DOE/DP/10560

KMSF-U2375

KMSF-U--2375

DE91 002771

Semi-Annual Technical Report

to the

Department of Energy

Period Covered
October 1989 - March 1990

MS Date: April 27, 1990

KMS Fusion, Inc.
700 KMS Place
Ann Arbor, MI 48108

Editor: Roy Johnson

Technical Editors: Ruth Luckhardt
Nancy Terry

Scientific Editors: Douglas Drake
James Gaines

DISCLAIMER

Table of Contents

FOREWORD 4

SECTION ONE. TARGET TECHNOLOGY 5

Introduction 5

1.1 Engineering Analysis 9
1.1.1 Automated Interferometry 9
1.1.2 Characterization of Layers on PS Shells 17
1.1.3 Residual Gas Analysis 25
1.2 Cryogenics and Tritium Technology 41
1.2.1 Beta-Heating Modeling Studies 41
1.2.2 Holographic Studies of DT Ice Layers 44
1.2.3 Experimental Design Considerations 58
1.3 Capsule Fabrication 62
1.3.1 Polymer Fuel Containers 62
1.3.2 Advanced Fuel Container Fabrication 94
1.4 Coating Technology 102
1.4.1 Films and Filters 102
1.4.2. Diagnostic Components 118
1.5 Microfabrication and Assembly 121
1.5.2 Target Deliveries to LANL 125
1.5.3 Target Deliveries to UR/LLE 127
1.6 References 128

SECTION TWO. LASER PLASMA INTERACTIONS 132

Introduction 132

2.1 X-ray Spectrograph Design and Development 134
2.1.1 High Energy X-ray Continuum Spectrograph for Aurora 134
2.1.2 High Energy X-ray Continuum Spectrograph for Nova 144
2.2 Los Alamos National Laboratory Probe Beam Design 151
2.3 Interpenetrating Plasma Experiment 154
2.4 Ionization Balance Experiments 163
2.5 A Likely Mechanism for Cold Jetting Radiation Cooling Instability 170
2.6 References 180

SECTION THREE. PRESENTATIONS AND PUBLICATIONS 182

3.1 Presentations 182
3.2 Publications 184

FOREWORD

This KMS Fusion Semi-Annual Technical Report covers the period October 1989 through March 1990. It contains a review of work performed by KMS Fusion, Inc. (KMSF), in support of the national program to achieve inertially confined fusion (ICF). A major section of the report is devoted to target technology, a field which is expected to play an increasingly important role in the overall KMSF fusion effort. Among the highlights of our efforts in this area covered in this report are:

- Improvements and new developments in target fabrication techniques, including a discussion of techniques for introducing gaussian bumps and bands on target surfaces.
- Development of a single automated system for the interferometric characterization of transparent shells.
- Residual gas analysis of the blowing gases contained in glass shells made from xerogels. These usually include CO_2, O_2 and N_2, and are objectionable because they dilute the fuel.
- Efforts to observe the ice layers formed in the β-layering process in cryogenic targets, and to simulate the formation of these layers.

In addition to our work on target technology, we conducted experiments with the Chroma laser and supported the ICF effort at other labs with theoretical and computational support as well as diagnostic development. Included in the work covered in this report are:

- Experiments on Chroma to study interpenetration of and ionization balance in laser generated plasmas.
- Diagnostic development, including an optical probe for the Aurora laser at Los Alamos National Laboratory, and a high energy x-ray continuum spectrograph for Aurora.
- Investigation of the radiation cooling instability as a possible mechanism for the generation of relatively cold, dense jets observed in ICF experiments.

SECTION ONE. TARGET TECHNOLOGY

James R. Gaines, Scientific Editor

Introduction

The Department of Materials Science (DMS) at KMS Fusion (KMSF) provides direct, program-wide support of experiments performed for the Department of Energy's inertial confinement fusion (ICF) program. Research and development work is pursued in target fabrication, coating technology, and target characterization so that targets supplied to the national laboratories can meet the ever-changing requirements of the ICF program. While some of the targets used for experiments can be fabricated by now-routine techniques, new and more challenging targets are being requested. Therefore the development of new approaches to target fabrication, a search for new materials, and the pursuit of new characterization techniques are all important activities for DMS. In this report, we summarize those activities for the six-month period, October 1989 through March 1990. We also describe our activity in delivering characterized targets to the national laboratories, an ever-increasing part of our overall effort.

Departmental Structure. Recognition that target deliveries had become a major activity of DMS precipitated a reorganization of the department effective January 1, 1990. As a result of this reorganization, a new group, Microfabrication and Assembly, was formed. This group was assigned the responsibility for making, characterizing, and delivering to the national laboratories those targets and target components that require little new development work. In this reporting period, deliveries were made to Lawrence Livermore National Laboratory (LLNL), Los Alamos National Laboratory (LANL), Sandia National Laboratory (SNL), and the University of Rochester's Laboratory for Laser Energetics (LLE). As a result of the reorganization, DMS now comprises five groups: (1) Engineering Analysis, (2) Cryogenic and Tritium Technology, (3) Capsule Fabrication, (4) Coating Technologies, and (5) Microfabrication and Assembly. The activities of all these groups are reviewed in this report.

Engineering Analysis. This group supports the activities of all other DMS groups through modeling and fundamental studies as well as characterization of developmental samples. In this reporting period, we began work in several areas that are central to the main target issues in the ICF program. One such area is the use of ray-trace modeling

and calculations that are based on the paraxial approximation in optics to design a new optical system capable of three different functions: (1) fast, accurate, and unattended characterization of batches of samples, (2) automated capsule selection, and (3) precise optical determination of capsule nonuniformity. The ideas that guide the design and construction of this system will be applicable to other precise characterizations required by the ICF program, such as the quantitative determination of the nonuniformity of the DT ice layer in a cryogenic fuel capsule.

Another activity of high practical importance is determining the amount of residual gas (i.e., gas evolved during capsule formation that remains in the capsule) in capsules that are subsequently filled with fuel gases by permeation techniques. Ideally, no gases would remain after the capsule is formed, so that only usable fuel would be present after permeation-filling with DT. Our work has centered on (1) determining the effective pressure of the residual gases in such capsules and (2) identifying the gases present as a function of storage time when DT, which can alter the chemistry as a result of its radioactivity, is also in the capsule.

One additional area of investigation that has both short- and long-term implications for the ICF program is the development of techniques for determining the properties (thickness, uniformity, surface finish, etc.) of poly(vinyl alcohol) (PVA) layers on plastic fuel capsules. Our previous work in this area has been extended to capsules that also have coatings deposited by glow discharge polymerization (GDP). We anticipate requests from the national laboratories for increasingly complex characterizations of coated and layered plastic fuel capsules. The details of the activities of the Engineering Analysis group appear in Section 1.1.

Cryogenic and Tritium Technology. Efficient laser implosion of a target requires that electromagnetic energy from several beams be combined at the location of the target. In the ideal case where the spatial distribution of energy is spherically symmetric, the target also must be spherically symmetric for maximum efficiency. Production of such a target has long been the goal of target fabrication in the ICF program.

The requirement for a high density target (to obtain high energy output) led to the suggestion that the fuel be either solid or liquid since solid and liquid densities are nearly one thousand times greater than gas densities. For hydrogen isotopes, this means that the sample must be held at low temperatures. Unfortunately the natural shape of both solid and liquid hydrogen samples formed at near-atmospheric pressure is not very symmetric. The discovery that β-heating of hydrogen samples containing tritium (such

as DT or T_2) could, in principle, produce uniform layers of DT ice inside spherical capsules was of major importance to the ICF program. The study of the effects of β-heating, both theoretically through modeling and experimentally in fuel capsules of the size currently of interest in the ICF program, has been the major focus of our work in Cryogenic Technology. The activities in both theory and experiment will be covered in Section 1.2.

The work on modeling β-heating includes development of a three-dimensional model of heat transport via free convection and conduction. The model is now being applied to β-layering in cryogenic DT ice targets cooled by an exchange gas with pressure high enough to provide significant convective cooling.

The main emphasis in the experimental program has been on demonstrating, via holography, that β-heating drives a *thin* layer of DT ice toward a highly symmetric shape. In previous work at KMSF, we took holograms of a capsule that contained gaseous fuel, then froze the fuel and took a series of holograms of the capsule containing frozen fuel. Comparison of the interferogram created by superimposing the gas hologram and the first of the solid holograms with interferograms created from the gas hologram and later solid holograms showed that the symmetry of the fuel layer increased with time. In fact, the interferograms approached the "bull's eye" pattern that would be expected for a perfectly symmetric distribution. Since the evidence for this increased symmetry came from only one view, it could be argued that the DT ice layer had only become cylindrically symmetric and that a second, orthogonal view would not be the same. This proved to be a difficult argument to counter because the apparatus used for the measurements had only one possible viewing axis, which meant that the sample itself had to be rotated! This work was finished during this reporting period and is described below. Based on these experiments, we concluded that the ice layer does approach the shape of a uniform spherical capsule but that it is not possible to quantify the layer's uniformity from this work. One very important conclusion can be drawn from the qualitative observation that these thin ice layers (so thin that only half the β-energy is deposited in them) become more uniform in time: If the innermost layer (8 μm) of ice becomes roughly uniform, then in a thick fuel layer, say 800 μm, the overall uniformity can be excellent, better than 1%.

In addition to the experimental work performed at KMSF, we have provided one person to support the program at LANL. This person is assisting LANL in taking and analyzing β-heating data obtained from direct imaging of the fuel layer. Preliminary

analysis of the LANL data has indicated that the β-heating does tend to produce a uniform DT ice layer. That work has been submitted (by LANL scientists in collaboration with the KMSF scientist) as a manuscript for the next *International Conference on Low Temperature Physics*.

Capsule Fabrication. The major development activities of this group have focused on plastic capsules, with special emphasis on improving their wall thickness uniformity. Our primary method of making these capsules, a drying column, has been augmented by another technique, microencapsulation. KMS Fusion previously made plastic capsules by microencapsulation, but characterization of those capsules revealed that voids (or vacuoles) existed in the capsule walls. This was unacceptable, so KMSF developed drying column technology for making plastic fuel containers.

Improvements in the microencapsulation process made at the Institute for Laser Engineering in Osaka, transferred to LLE (where additional refinements were made), and then transferred to KMSF have resulted in a re-examination of this process. As a result of these advances in the technology, KMSF can now make plastic capsules (by microencapsulation) of the size and uniformity of interest to the ICF program that are as good as those made in any other laboratory. The problem with the vacuoles has been reduced, but not entirely eliminated. It is safe to say that the number of large (0.5 μm or larger) vacuoles per capsule is now reduced to ten or fewer. The actual number that can be tolerated is unknown (and may be zero), but it is certain that progress has been made toward developing a usable plastic fuel container that will have high wall uniformity and a narrow range of outside diameters.

Another major activity involves the design of a new PVA coating system. This system will be of great immediate use in plastic capsule fabrication and should be able to provide coatings of the quality and thickness likely to be requested in the future. All of these activities are described in Section 1.1.3.

Coating Technologies. The major activity of the Coating Technologies Group has been the support of ion beam diagnostic work being done at SNL. This work has involved (1) producing and then precisely characterizing very thin gold foils that can be used to measure the distribution of ion beam intensity and (2) producing and then characterizing both free-standing metal foils and supported foils that can be used as x-ray filters.

The films made from very thin gold foils have proven to be of very high quality, with unprecedented uniformity, so that they have given very valuable information about the

ion beam's intensity distribution. The filter arrangements have consisted of single metal, single polymer, metal/metal, metal/polymer and even polymer/polymer films. This work is reported in Section 1.1.4.

Microfabrication and Assembly. This group, charged with making and characterizing those fuel capsules requested by the national laboratories that do not require extensive development, has been able to maintain a timely delivery schedule for all the laboratories to date. The actual deliveries covered in the period January 1, 1990, to March 31, 1990, are detailed in Section 1.1.5. Not included in this list are deliveries to SNL of films and filters that are made by our Coating Technologies Group.

1.1 Engineering Analysis

In the following section, activities of this group in three areas are detailed: (1) automated interferometry, (2) characterization of poly(vinyl alcohol) (PVA) or NaCl layers on polystyrene (PS) shells, and (3) residual gas analysis. Additional activities of this group are described in other sections of this report, most notably Section 1.1.3, Capsule Fabrication, which describes the use of modeling results to improve our fabrication and coating techniques.

1.1.1 Automated Interferometry

We are developing a single automated system for the interferometric characterization of transparent shells.[1] There are three specific goals for this system. The first goal is to provide an automated system capable of selecting shells with specified diameters, specified wall thicknesses, and wall uniformities determined at the 3% level from a large sample of shells. This process should make possible the unattended identification and location of good shells in a batch. The second goal is to provide a system capable of the unattended characterization of shells in a batch for statistical purposes. The third goal is to provide a system capable of accurately characterizing the wall nonuniformity of individual selected shells to the 1% nonuniformity level. This final goal does not require full automation, but it does require the same image-analysis techniques as the other goals.

An automated interferometry system consists of several components of both hardware and software. Hardware includes an interferometer, a motorized stage, stepper motors for selected interferometer adjustments, controlling electronics, a camera/image digitizer, display hardware, and a computer. Software tasks include stage and

interferometer control, image acquisition, image analysis, optical modeling/analysis, and overall coordination of the various elements.

A Jena Jenavert interference microscope has been purchased. This interferometer was chosen for its exceptional stability, which is essential for analysis techniques involving multiple fringe images. This is a shearing Mach-Zehnder interferometer, in which an split image shear generates two images, which are interfered against each other. When the shell from one image is interfered against the background in the second image, the familiar bull's eye pattern is seen. This instrument imposes some important limitations on our image acquisition in that, as now configured, its useful field of view (maximum shear) is 500 mm, with a resolution of 2.8 mm. We are looking into modifications to improve these figures, and we will be using image analysis techniques to reduce the consequences of the limited resolution.

Motorized stages meeting the required standards of accurate motion are commercially available as off-the-shelf components. Motorized control of compensator, and possibly filters and aperture diaphragms, will also be required.

The choice of image-acquisition hardware depends upon available light, dynamic-range requirements, and resolution requirements. Although the nominal resolution of the interferometer gives us only about 180 resolution lines across the usable field, we will need a finer grid of pixels to allow maximum use of the information available. We also must consider dynamic range, as the actual photometric intensity across a fringe pattern is critical for phase-shift analysis. Finally, the light levels of the fringe image must be assessed for the configuration of interest when delivery of the interferometer is completed. Based on our current understanding, a 1024 x 1024 eight-bit camera should be adequate.

Interface electronics will ultimately depend on the choice of camera. A VAX workstation, capable of meeting our anticipated computing needs, may be available in-house. It will need additional boards for the required interfacing.

Executive software design has begun. We have conceived strategies for shell location, focus, and centering. Control software is to be developed as mechanical design progresses. Image-acquisition software will depend on the camera decision.

Image-processing software has been tested on images acquired with a video camera attached to a Leitz interferometer. The phase-shift analysis software[2] has generated high-quality phase map data and fringe contours, as shown in Fig. 1-1.

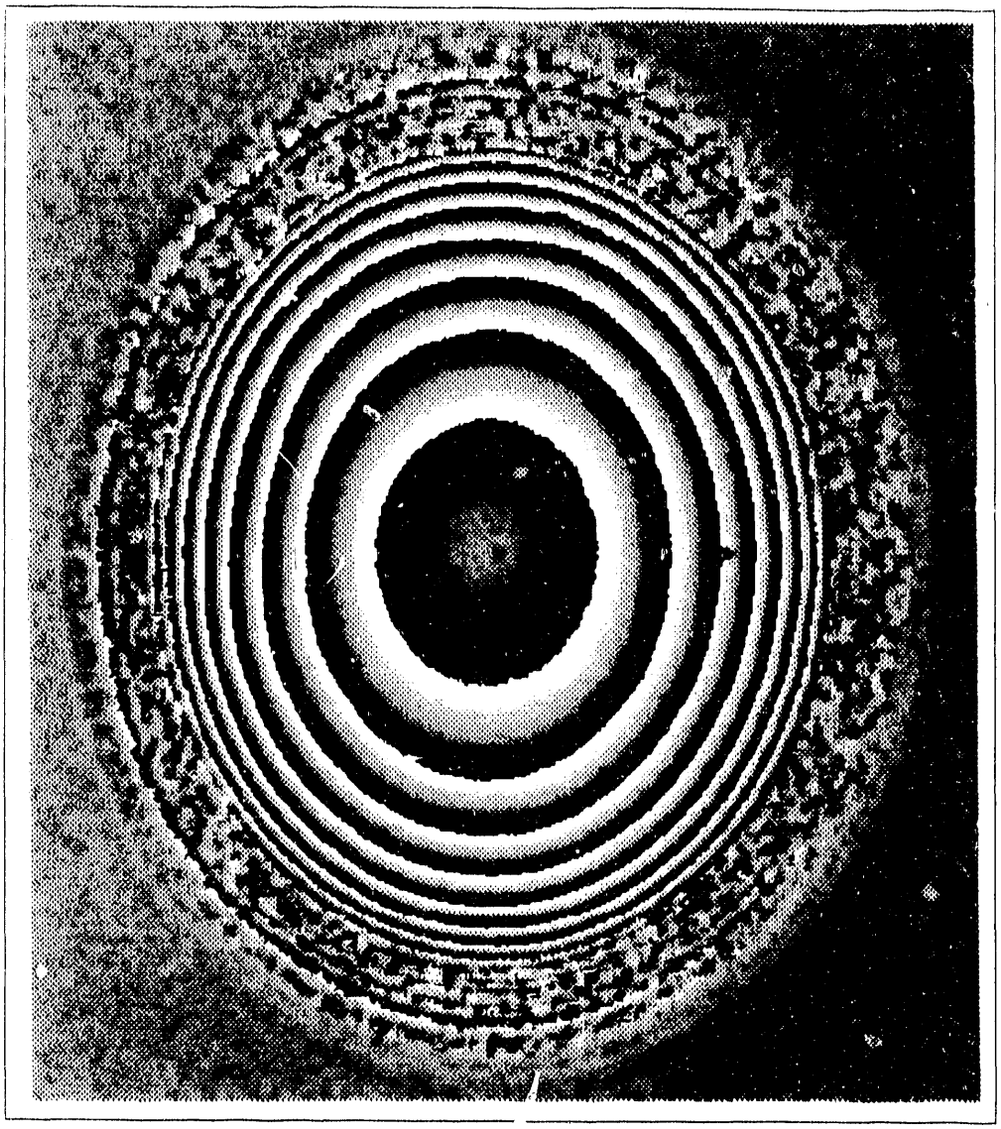

Fig.1-1a. This raw phase map of a glass shell was produced from three fringe images. Brightness indicates phase; sharp edges are phase jumps occurring at 360° intervals of phase. (Vertical stretch is an artifact of the imaging system.)

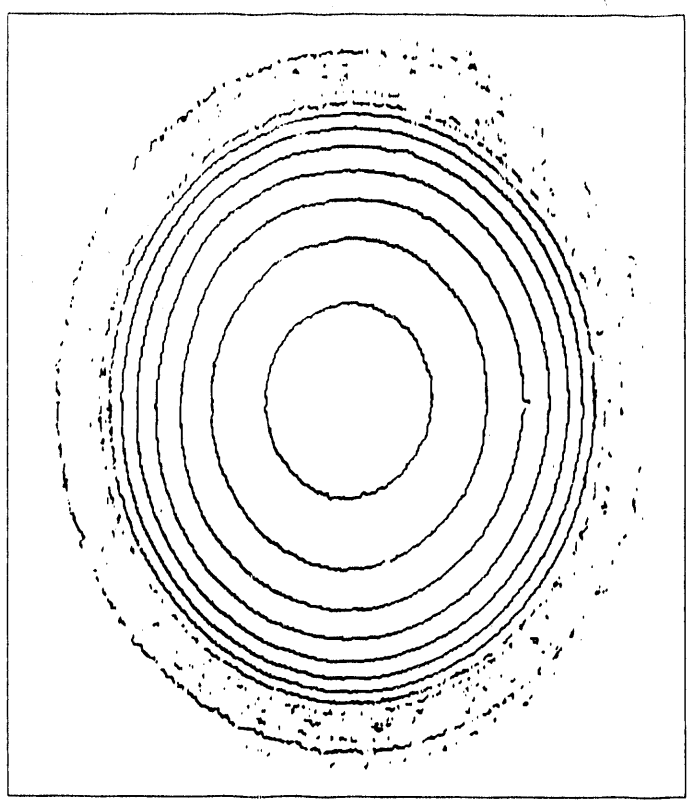

Fig.1-1b. Phase jumps from the image in Fig.1-1a. These can be used as fringe contours and interpreted as ordinary interference fringes. (Vertical stretch is an artifact of the imaging system.)

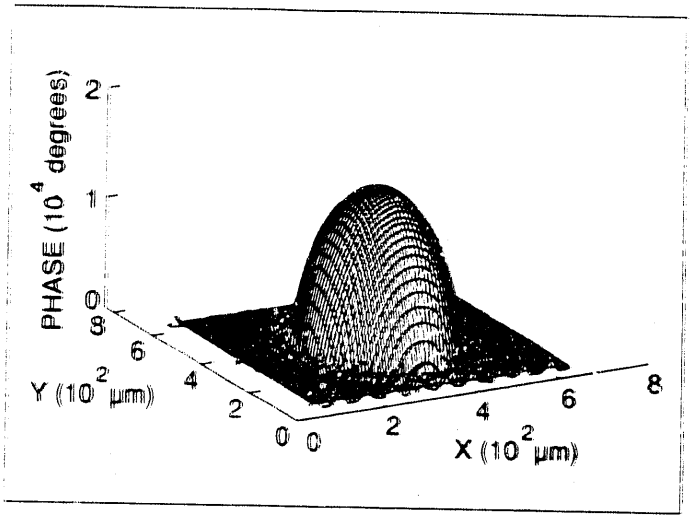

Fig.1-1c. Surface plot of phase function from image in Fig. 1-1a, processed to remove phase jumps. This function contains more information than simple fringe contours.

The ultimate characterization of shell geometry depends on modeling of shell optics to relate processed image data to shell properties. We are concentrating our efforts on interpreting fringe offset and ellipticity in terms of shell wall P_1 and P_2 defects. We have used two methods for this modeling: ray-trace and the paraxial method.[3] Both methods directly predict phase front or fringe properties produced by given shell geometries. Both methods require some sort of iterative approximation method to determine shell geometry from fringe patterns. Paraxial modeling is preferable for real-time use, as it is fast and yields concise fringe or phase data. However, paraxial results are strictly true only at the center of a phase or fringe image. To extend these results and make them usable over the entire useful area of a fringe image, ray-trace modeling is required. Ray-trace modeling is too slow for real-time use, so its value is limited to determining calibrations or corrections for paraxial modeling.

We are examining several schemes for the analysis of phase or fringe data. In each case, analysis begins with the acquisition of at least three stepped-phase fringe images, which are then processed into a raw phase map. This map is then sampled either in radial vertical slices, for phase profiles (see Fig. 1-2), or horizontal slices, for phase contours (roughly corresponding to fringes -- see Fig. 1-3).

If we slice vertically, the figures of interest in each slice are offset of the phase maximum and the second derivative of the phase at the image center. Phase maximum offset is caused by P_1 defect. Variations in second derivative are caused by P_2 defect, while the mean value of second derivative indicates wall thickness. Both values are best judged from the parameters of a curve-fit to the phase front data. We are looking into two approaches to this fit.

The first approach is to use a simple polynomial fit. Unfortunately, this method produces errors of several percent in second derivative. We are looking into quantifying this error over a wide range of parameters, so that we can use ray-trace-derived correction factors in practice. A preferable approach would be to curve-fit to an analytical function that more closely approximates the actual phase function. We are evaluating several functions for such a fit.

If we slice the phase map horizontally, to generate fringe-like contours, there are other options for analysis. We may select fringes at particular radii, or at particular phases. In either case, we can use correction factors determined with ray-trace modeling to relate the offsets and ellipticities of measured contours to the idealized zero-radius fringe used in the paraxial method.

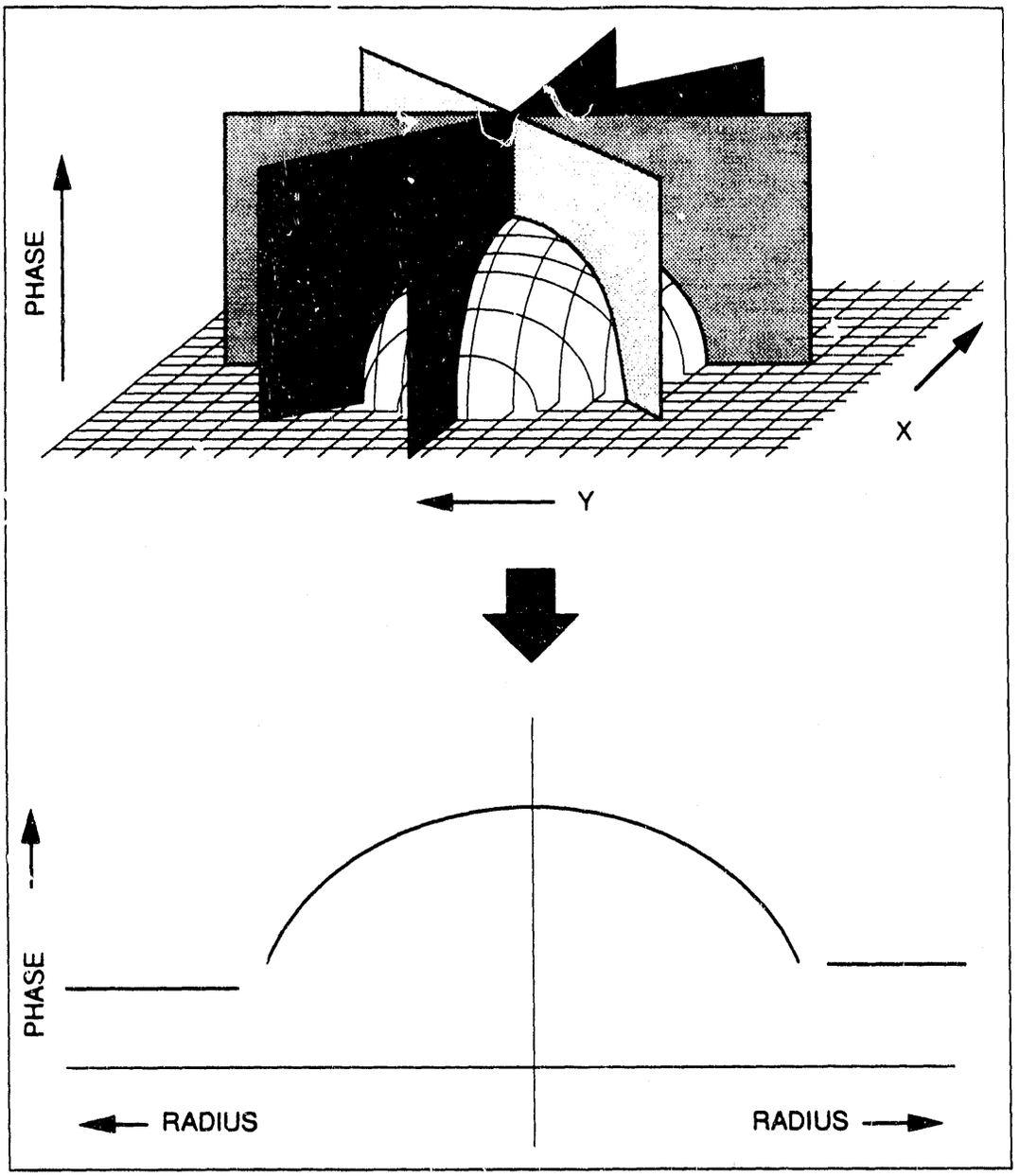

Fig.1-2. Radial vertical slices of the phase map generate phase-front functions. The curvature of the function at the center, averaged over many slices, gives thickness information. Variation and offset of slices is caused by nonuniformity

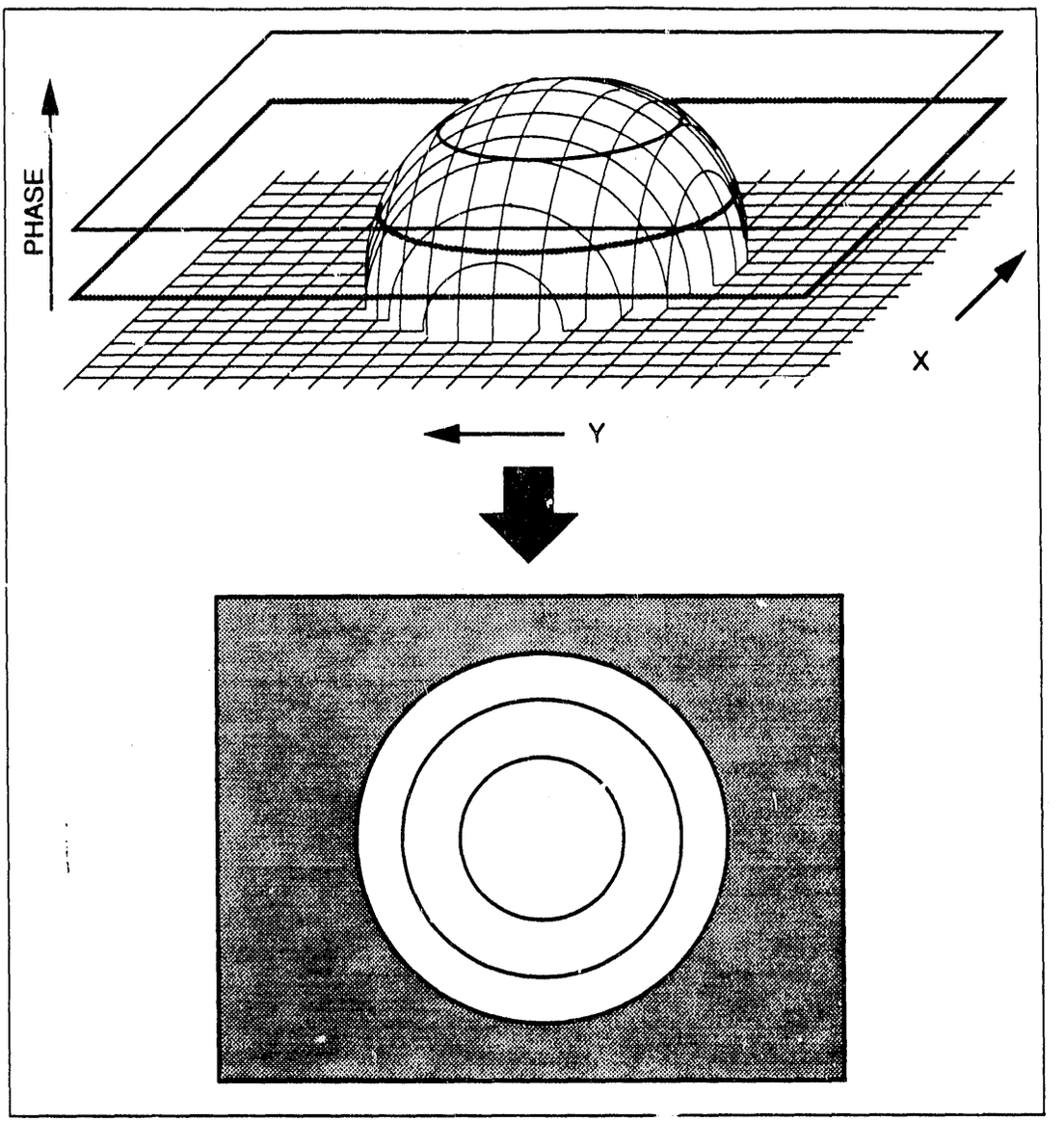

Fig.1-3. Horizontal slices of phase map generate contours corresponding to fringes. Deviation from circular concentric fringes is caused by nonuniformity. Radius and phase differences between contours together indicate thickness.

Whichever strategy is ultimately adopted, corrections or fit functions will be determined in advance by an array of ray-trace models covering a widely spaced array covering many shell parameters. The paraxial model will be used in real time to zero in on actual values of various P_1 and P_2 nonuniformities.

For additional information, please contact Peter Alway

1.1.2 Characterization of Layers on PS Shells

Polystyrene (PS) is a leading candidate material for inertial confinement fusion (ICF) fuel capsules because of its low effective atomic number and its expected ease of formation into high quality shells. However, one of the problems with PS is its high permeability to the hydrogen isotopes. An alternative capsule is a composite, a PS shell with a coating of poly(vinyl alcohol) (PVA), which serves as a permeation barrier. For such a PVA/PS composite capsule, a procedure to measure the wall thickness of the layers is needed.

In our 1989 Annual Technical Report[4] we described a procedure to determine the layer thickness of PVA/PS shells, based on optical measurement of a radiographic image of a PVA/PS shell. This procedure has been modified to enable us to measure the layer thicknesses of such PVA/PS shells that also have glow discharge polymerization (GDP)-deposited coatings.

We currently deliver NaCl-coated PS shells that have a thick GDP coating. We have a standard procedure for characterizing the uniformity of the NaCl layer, which was described inour 1989 Semi-Annual Technical Report.[5] This procedure involves radiographing witness shells after the NaCl coating but before the GDP coating, digitizing the radiographic images, and using image analysis to analyze the digitized images. Our desire is to expand this capability to allow characterization of the NaCl uniformity of each shell after the final GDP coating.

Poly(vinyl alcohol) Layers on PS Shells. The ability to detect an interface between two materials in intimate contact, such as PVA on PS, from a radiographic image is determined by the relative x-ray absorptivities of the two materials under the x-ray exposure conditions used. The x-ray exposure is selected to give the greatest absorption difference in the two materials. The x-ray path length through the materials is taken

into account when selecting an accelerating voltage. The voltage must be high enough to allow a sufficient x-ray flux to penetrate the shell and reach the x-ray plate without eliminating the x-ray absorption differences in the two materials. Once the proper voltage is determined, the exposure time can be varied to give the desired plate density.

A simple computer model, based upon chord length, was used to predict the intensity profile through the shell wall that would be expected from a radiographic image. This model determined the chord length through the GDP, PVA, and PS components of the wall, and multiplied the PVA chord length by 1.6, the ratio of PVA to PS absorption coefficients for the energy range of interest. The relative GDP/PS absorption was assumed to be 1. Figure 1-4 shows the intensity profile through a shell with a 3 μm thick wall, a 3 μm thick PVA coating, and a 40 μm thick GDP layer. The vertical lines a, b, c, and d are located at the computed inner wall of the PS, the PVA/PS interface, the GDP/PVA interface, and the outer edge of the GDP, respectively. The distinct peak at the PVA/PS interface (b) and sharp change in slope of the curve at point c from this intensity profile demonstrated that it should be possible to see both the PVA/PS and GDP/PVA interfaces from a radiographic image exposed under the right conditions. As a comparison, Fig. 1-5 shows a trace through the shell wall from an actual GDP/PVA/PS composite shell.

Poly(vinyl alcohol)-coated PS shells with and without 40 μm of GDP were used as samples for the radiography. The shells were supported on a 50 μm beryllium strip with a thin layer of grease to hold the shells in place. The beryllium strip was weighted down during the exposure to secure it. The x-ray unit used a sealed tube with a tungsten target as the x-ray source, with an x-ray spot size 400 μm in diameter. The anode-to-sample distance was approximately 40 in. Kodak high-resolution glass plates were used to record the radiographic images. An accelerating voltage of 5.5 kV was used with exposure times ranging from 30 to 120 min. The radiographic plates were developed for 5 min at 68°F using Kodak D-19 developer.

An exposure time of 60 min was best for PVA/PS shells without additional GDP coating. Using exposure times much less than this decreased the contrast of the interface, while exposure times much greater than this made the interface appear thinner and less distinct.

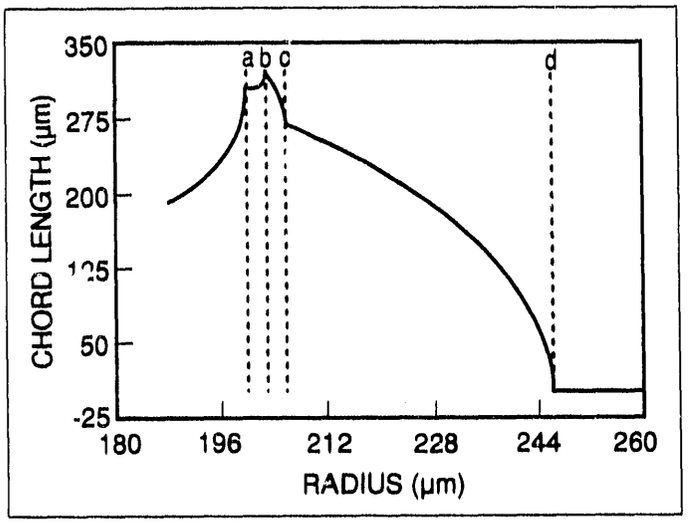

Fig.1-4. The predicted shape of an intensity trace through the wall of a radiographic image of a GDP-coated PVA/PS shell. The shell inner radius is 200 μm and the inner wall is located at peak a. The wall and PVA coating thicknesses are 3 μm each and the GDP thickness is 40 μm. The PVA/PS interface is at the dotted line b, which is also located at a peak. Dotted line c is at the GDP/PVA interface. A line at the PVA/PS interface should be visible on a radiographic image corresponding to peak b on this model, and the GDP/PVA interface should be visible where point c is located.

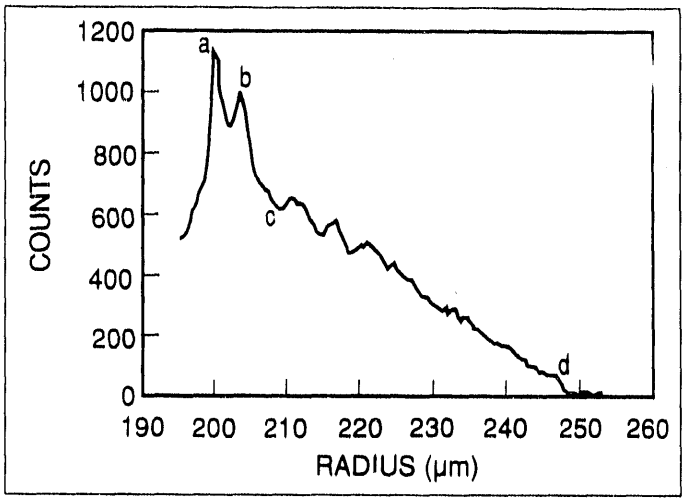

Fig.1-5. A radial trace through the wall from a digitized radiographic GDP/PVA/PS shell image. The inner wall of the shell is at peak a, the PVA/PS interface is at peak b, the GDP/PVA interface is at point c, and the outer edge of the GDP coating is at d.

For the shells with GDP coating, exposure times from 90 to 120 min were best. The PVA/PS interface was quite distinct within this exposure time range but was considerably less distinct for the 30 and 60 min exposures. The GDP/PVA interface was quite distinct for all four of the exposure times, although it was also somewhat better for the 90 and 120 min exposures. The outer GDP edge was very sharp at each of the exposure times.

A Nikon Optiphot microscope was used to examine the radiographic shell images at high magnification (400x). On the shells without GDP coating, the PVA/PS interface appeared as a fine, distinct line between the inner edge of the PS and the outer edge of the PVA coating. The PVA thickness can be measured at locations around the shell image to determine average thickness and uniformity. These measurements can be made directly on the microscope using a reticle or from a photograph of the shell image using Polaroid type 52 film.

On the shells with GDP coating, the PVA/PS interface appeared as a fine, distinct line between the inner edge of the PS and the PVA/GDP interface, although it was not as clear as on the shells without GDP coating. The GDP/PVA interface was not as sharp as the PVA/PS interface although it was still quite obvious, especially on the photographs, which tend to enhance the contrast between the layers. For this reason, is it better to measure the PS and PVA thicknesses from a photograph. It probably will be necessary to make the GDP thickness measurements directly on the microscope using a reticle -- it is virtually impossible to achieve correct exposure of both the inner and outer edges of the GDP simultaneously on Polaroid 52 film because the background outside the shell is so dark. Polaroid type 51 film, which is a high-contrast film, may be useful in accentuating the layer interfaces. However, it is highly sensitive to exposure conditions and much trial-and-error may be needed to obtain optimal exposure conditions.

Figure 1-6 is a photograph of a PVA/PS shell. The PVA/PS is quite distinct and it is obvious that the PVA coating is not uniform. Figure 1-7 is a photograph of a GDP/PVA/PS shell. The inner edge of the PS is the sharpest interface, but the PVA/PS and the GDP/PVA interfaces are also quite obvious. The outer edge is the GDP is not visible on the photograph, although it is visible on the radiographic plate.

Fig.1-6. This is an image of a PVA/PS composite shell where the PVA is several micrometers thick at the thickest point and decreases to an undetectable level. The brightest line is at the inner edge of the PS shell. The second line half the distance to the outer edge of the shell is at the PVA/PS interface.

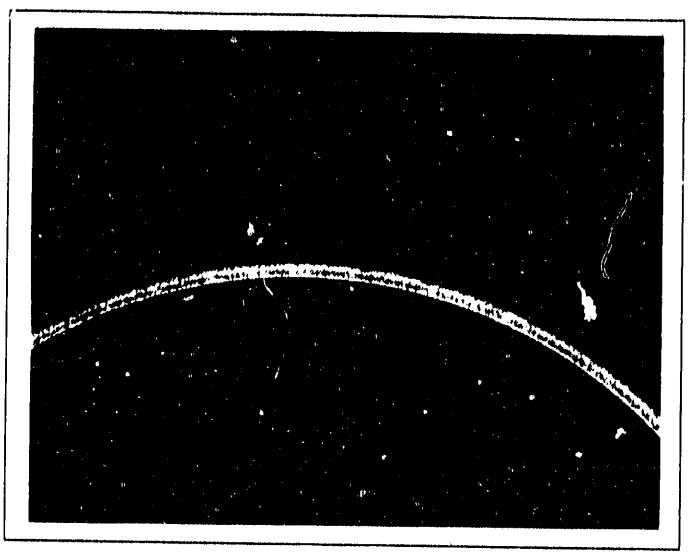

Fig.1-7. This is an image of a typical GDP/PVA/PS composite shell. The brightest line is at the inner edge of the PS shell. The next line is at the PVA/PS interface. The GDP/PVA interface is where the intensity drops off sharply. The outer edge of the GDP is not visible for the exposure conditions of the photograph because plate density in the background around the shell is too high.

Characterization of NaCl Uniformity on PS Shells. Two types of image analysis are used for our current procedure. The first uses several edge-detection schemes to locate various interfaces. The second type uses the pixel intensity variation along a particular edge contour (the inner wall of the shell). There are two contributing factors to the pixel intensity under this contour, the PS shell wall and the NaCl coating. The contribution due to the shell wall can be determined and removed, leaving the contribution due solely to the NaCl coating. The remaining intensity variation around the contour can then be related to NaCl coating uniformity. As previously stated, the final targets have an additional GDP coating added over the NaCl layer. Since witness shells are used for the NaCl uniformity analysis, only an average uniformity for the batch is obtained. The desire is to be able to determine the NaCl uniformity on each shell after GDP coating. The current effort is directed toward this goal.

The question is how best to remove the intensity contribution due to the GDP coating and PS wall. Since GDP absorbs oxygen, the contribution due to this unknown amount of oxygen must be taken into account. We have designed and are now testing a scheme for doing this.

Each GDP coating run of NaCl-coated PS shells will include samples of PS shells without NaCl. The shells without NaCl will be used in place of the uncoated PS shells in the radiographic characterization procedure. Since both types of shells will be from the same GDP coating run and exposed to the same conditions, they should both have the same GDP composition and the effects of the oxygen in the GDP can be mitigated. The rest of the analysis should be very similar to the previous analysis on shells without GDP coating.

Several questions will have to be answered as this procedure is investigated. One question is how the additional GDP coating will affect the performance of our current edge-detection programs and whether they will need any modification. Another question is the effect the GDP coating has on the sensitivity of the NaCl uniformity measurements. These concerns will have to be answered before we can characterize completed targets individually.

For additional information, please contact Steven Welch

1.1.3 Residual Gas Analysis

Glass shells made from xerogels contain residual blowing gases that usually include CO_2, O_2, N_2, and sometimes H_2O (Ref. 6). These residual blowing gases, at pressures up to 0.25 atm (room temperature), are especially objectionable in ICF targets with low fuel pressure because they dilute the fuel significantly.

Residual gases may, however, react with the fuel to form products of lower average atomic number. The hydrogenation of CO_2 and O_2 to CO (or hydrocarbons) and water are classical reactions, but require catalysis;[7,8] these reactions can also be activated by the β-flux of tritium decay.[9,10] While the reactions are thermodynamically favored at the pressures and temperatures employed in the permeation filling of shells, the rates of these reactions in ICF targets, and the extent of activation by the β flux from the decay of tritium, are not known quantitatively. In addition, reaction with the shell wall can remove some residual gas components. If matrix modifiers (e.g., alkali metals) diffuse to the inside wall, they can scavenge CO_2.

The objective of this work was to identify the residual gases in targets prepared for Lawrence Livermore National Laboratory (LLNL). These targets were glass shells with dimensions of 370 x 9 μm (o.d. x wall thickness) that were filled with 2 or 5 atm of fuel. We needed to determine the composition and amount of the residual gases as a function of DT or D_2 fill pressure (2 and 5 atm) as well as the cumulative effect of the β-flux on the gases in stored DT-filled shells.

In the past year, we measured the composition and amount of residual gases in glass targets that are typical of the usual ICF targets supplied to LLNL. This report extends our previous work[11] with results from DT-filled shells that were stored for almost two months. Deuterium was not investigated during this period.

Procedure. Glass shells were chosen from batches that were the sources for LLNL orders. These shell batches (T4R1218, T4R1220, and T4R1229) were all made from the same xerogel under similar furnace conditions. Each batch had approximately the same mean diameter (425 μm) and wall thickness (10 μm). Generally, shells from T4R1218 and T4R1220 were chosen from the 400 to 450 μm diameter range, although in four cases shells from the 300 to 350 μm range were also used in the analysis. All shells from T4R1229 were 350 to 390 μm in diameter.

Residual gases from these shells were analyzed under three conditions:

1. As made, to determine the initial residual gas composition (which depends on gel composition, furnace conditions, and shell size).

2. After filling with 5 atm D_2. Shells were filled according to our standard procedure at 360°C for two days. Shells containing D_2 were not evacuated before analysis.

3. After filling with 2, 5, or 10 atm DT. Shells were filled at 360°C for two days and stored for various periods of time (from 0 to 50 days). These shells were evacuated for three days before analysis to minimize the radiation hazard as the DT exited the gas chromatography (GC) apparatus and to allow measurement of total residual gas pressure by the gas entrapment in a viscous fluid (GEVF) technique.

Compositional analyses of these residual gases were performed by GC. Between 30 and 150 shells were broken in the inlet of the instrument per run. Most analyses were run in triplicate. The response of the GC was calibrated against a gas standard whose composition is traceable to a National Institute of Standards and Technology standard. For samples having a narrow shell diameter distribution, the GC results were reduced to an average residual gas pressure per shell by using the total volume of residual gas (obtained by adding the measured volumes of individual species) divided by the number of shells in the sample, the average shell volume (determined from the average shell diameter), and the ideal gas law. Results were adjusted to 298.2K. In many cases, total residual gas pressure was measured independently by our GEVF method, for comparison with the GC calculated pressure.

Results and Comments. Table 1-1 lists results from exposing the residual gases to 2 atm DT for various times. Data are listed separately for each shell batch examined. Values of gas composition are given as volume percent. In four cases, shells of mixed diameters were analyzed (i.e., the sample contained shells in the 300 to 350 μm and 400 to 450 μm diameter range); since the number of shells in each diameter range is unknown, GC-derived total pressure per shell was calculated assuming only measured

Table 1-1. Volume percent residual gas composition of glass shells filled with 2 atm DT and stored at room temperature for varying times. Pressures listed are total average pressure per shell.

Batch	Time (days)	O_2	N_2	CO_2	CO	CH_4	C_2H_n	Pressure, from GC (atm)	Pressure, from GEVF (atm)
T4R1218	0	19.6	7.8	72.6	-	-	-	0.19	0.21
T4R1218	1.9	0.40	9.8	65.2	24.6	-	-	0.15 [a]	-
T4R1218	13.8	0.37	9.98	73.9	14.1	1.4	-	0.15 [a]	-
T4R1218	36.9	0.52	9.78	73.25	10.5	5.1	1.65	0.12	0.079
T4R1220	0	20.7	8.07	71.2	-	-	-	0.17	0.19
T4R1220	1.9	0.50	9.27	73.8	16.4	-	-	0.11 [b]	0.115
T4R1220	13.8	0.40	9.71	76.6	12.0	1.34	-	0.11[b]	-
T4R1220	36.9	0.37	10.0	76.3	8.8	3.7	1.0	0.12	0.086
T4R1220	51.0	0.24	12.2	78.7	3.18	5.7	-	0.10	-[c]
T4R1229	0	21.95	9.65	68.4	-	-	-	0.16	0.17
T4R1229	2.0	0.34	11.2	66.15	21.8	-	-	0.126	0.10
T4R1229	44.1	0.83	14.0	66.7	9.9	7.0	2.3	0.081	0.071

a. Calculated pressure, based on observed loss of oxygen, because of mixed shell sizes in sample.
b. Calculated pressure, based on observed loss of oxygen, because of mixed shell sizes in sample.
c. DT was not evacuated for this analysis.

O_2 loss from the as-made shell. One sample, T4R1220, stored with 2 atm DT for 51 days, was not emptied before analysis. Its analysis seems to fit in with the other samples, which were emptied first. This suggests that the heating required to remove DT does not substantially change the composition of the residual gases after appreciable exposure time. This may be due to rapid removal of the bulk of DT in the first few hours of heating.

Table 1-2 lists similar data for 5 and 10 atm DT exposures for various times, as well as D_2 data. Figure 1-8 shows the change in total residual gas pressure with duration of exposure to 2 atm DT for each shell batch, based on GC-derived total pressures. Error bars display $\pm 1\sigma$ calculated from all sources of error for the GC (see Error Considerations, below). Figure 1-9 shows similar data obtained from the GEVF test on the same batches of shells. Here, error bars display $\pm 1\sigma$ based on the 20 to 30 measurements from which each GEVF average pressure reading is derived. The GEVF data show unambiguous loss in residual gas pressure after the initial fill period (2 days). Thereafter, both graphs show equal, continuing pressure losses. Figure 1-10 presents loss of residual gas pressure in 5 and 10 atm DT fills as a function of time. At higher fuel gas pressures, residual gas loss occurs more rapidly and to a greater extent than in the lower pressure fills.

Discussion. Oxygen quickly (i.e., within the DT fill time of 2 days) drops to a steady-state value of 1 to 3% of its original value and remains constant thereafter. It is converted to water during the DT fill step and permeates out of the inner void of the shells.

Nitrogen is only slightly affected by DT and remains near its original amount in 2 atm fills. After two months' storage at room temperature, losses observed in N_2 levels are approximately 10%. Probable reactions for nitrogen include formation of ammonia (NH_3) or low molecular weight amines (e.g., CH_3NH_2), neither of which can be seen by the GC as currently configured. However, neither of these compounds has been observed in the mass spectroscopy work done on these filled shells at KMSF.[12]

During the fill step, about 25% of the CO_2 is converted to CO by the DT as it permeates into the shell at 360°C. Thereafter the room-temperature reduction of CO_2 proceeds more slowly, forming step-wise reduction products according to the sequence,

$$CO_2 \rightarrow CO \rightarrow CH_4 \rightarrow C_2H_n .$$

Table 1-2. Volume percent residual gas composition of glass shells filled with 5 atm D_2, 5 atm DT, or 10 atm DT, and stored at room temperature for varying times. Pressures listed are total average pressures per shell. Shells were emptied of fuel gas before analysis.

Batch	Gas Fill (atm)	Time (days)	O_2	N_2	CO_2	CO	CH_4	C_2H_n	Pressure, from GC (atm)	Pressure, from GEVF (atm)
T4R1220	DT (5)	0	20.7	8.07	71.2	-	-	-	0.17	0.19
T4R1220	DT (5)	1.9	0.34	8.6	44.8	45.3	0.98	-	0.17	
T4R1220	DT (5)	34.9	0.37	11.65	50.2	14.45	23.3	-	0.12	0.082
T4R1229	DT (5)	0	21.95	9.65	68.4	-	-	-	0.16	0.17
T4R1229	DT (5)	1.9	0.44	10.45	33.05	55.45	0.7	-	0.12	-
T4R1229	DT (10)	0	21.95	9.65	68.4	-	-	-	0.16	0.17
T4R1229	DT (10)	6.8	1.1	18.0	31.5	20.8	20.0	8.6	0.073	0.062
T4R1229[a]	D_2 (5)	0	21.95	9.65	68.4	-	-	-	0.16	0.17
T4R1229[a]	D_2 (5)	2.0	0.67	10.5	54.0	34.8	-	-	0.117	-[b]

a. Data from last report.
b. D_2 not evacuated for this analysis.

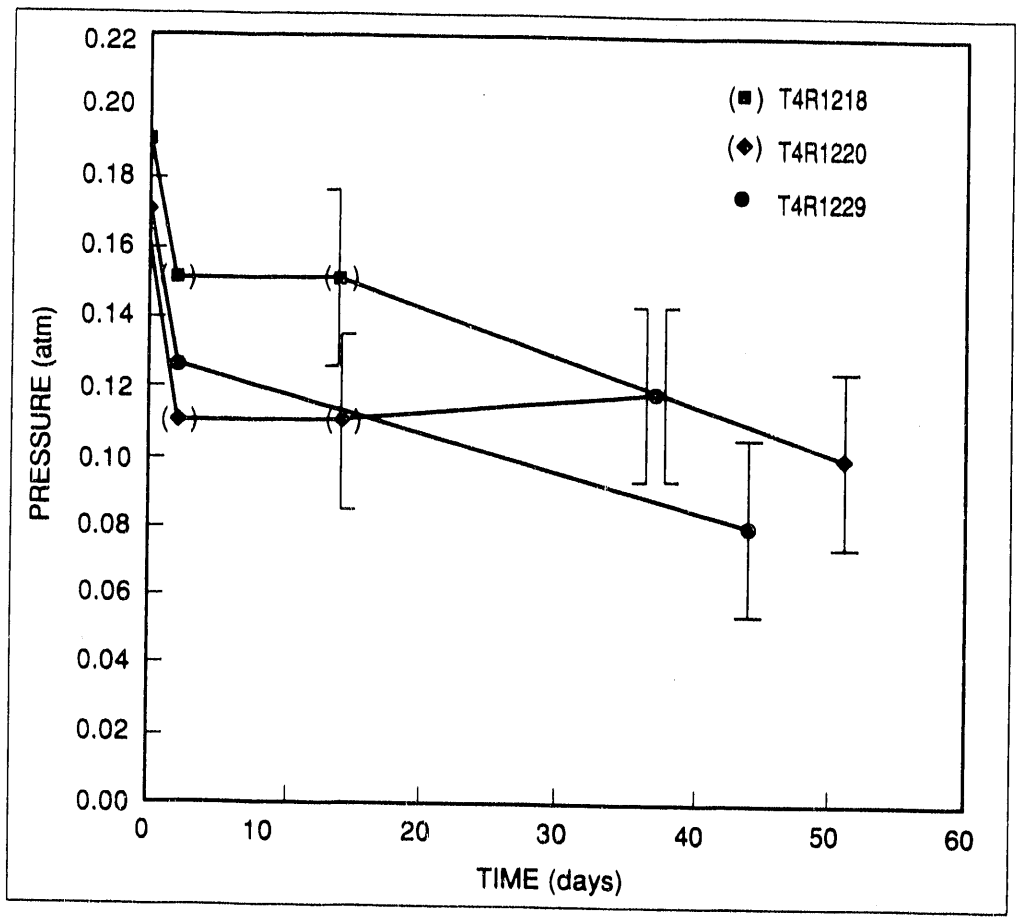

Fig. 1-8. Variation of total residual gas pressure in glass shells with exposure time to 2 atm DT fuel gas. Error bars show ±1σ (~18.7%). Parenthetical points are calculated values based on measured loss of oxygen (shell sample had mixed diameters).

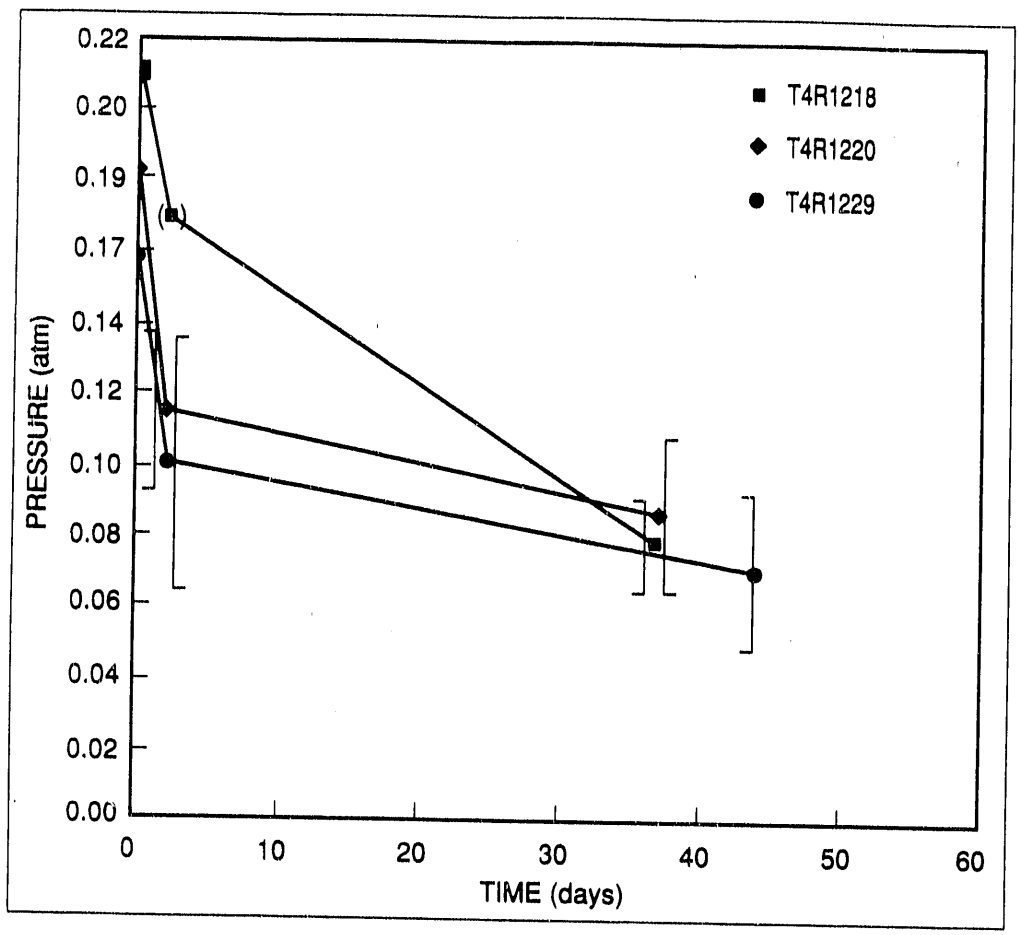

Fig. 1-9. Variation of total residual gas pressure in glass shells with exposure time to 2 atm DT fuel gas, as measured by the GEVF method. Error bars show ±1σ. The parenthetical point was calculated from measured loss of oxygen.

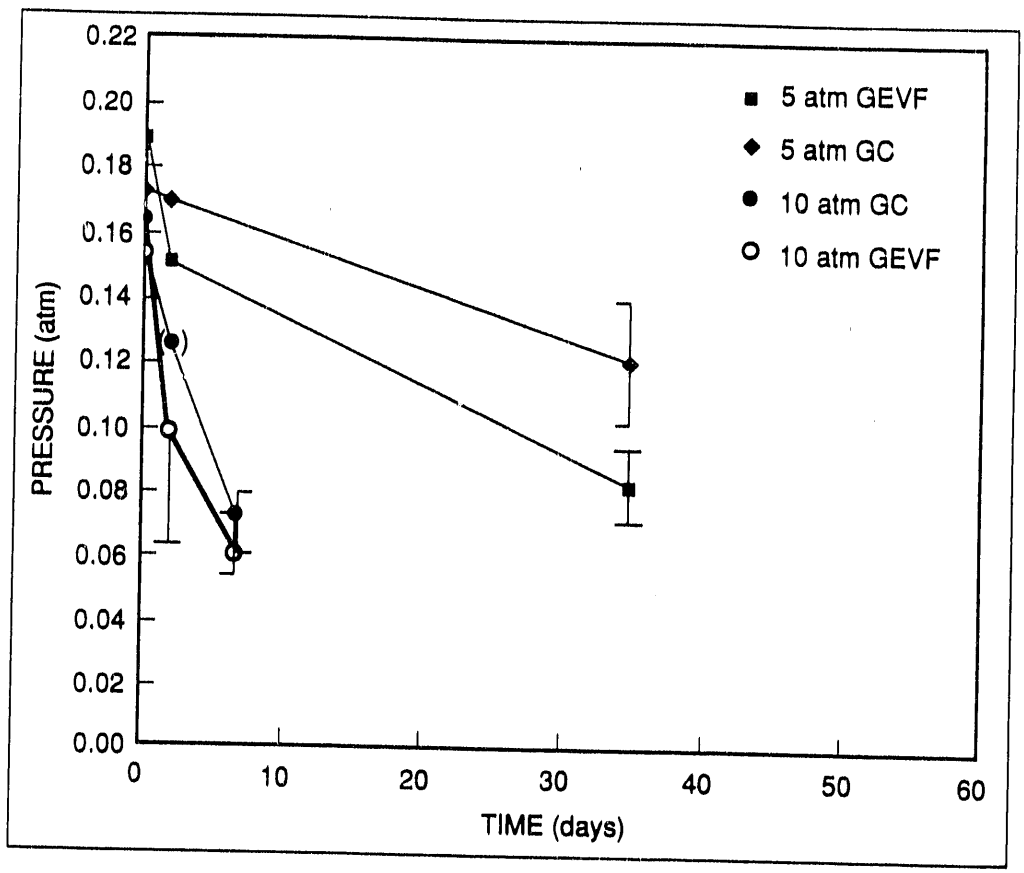

Fig. 1-10. Variation of total residual gas pressure in T4R1220 glass shells with exposure to 5 atm DT, and in T4R1229 glass shells with exposure to 10 atm DT, as measured by both GC and GEVF methods. Error bars show $\pm 1\sigma$. Parenthetical values at 1.9 days for the 10 atm data are calculated, based on loss of oxygen.

Carbon monoxide concentration peaks during the fill process, then slowly declines at room temperature as methane, and possibly CO_2 (by disproportionation), is formed. Higher homologues of methane (acetylene, ethylene, ethane) form slowly in shells containing 2 atm DT, constituting about 1% of the total gas in the shells after 37 days; higher pressures of DT increase the formation rates of these species.

This information is summarized in Table 1-3, which tabulates partial pressures of constituent species based on percent composition and GC-derived total pressures for 2 atm fills. Data are organized according to shell batch. In the far right column is listed the sum of the partial pressures of all carbon species for each exposure. For the first two or three weeks of exposure time, the sum of the partial pressures of all carbon species is reasonably constant. After this time we see a decrease in total carbon content, but the precision of the 2 atm data makes the exact amount of decrease uncertain.

These trends are shown more clearly in graphs of normalized composition for the residual gases. Data from all three shell batches have been combined and presented as an average percent of the original total amount of each gas species, plotted against duration of exposure to 2 atm DT. Figure 1-11 contains data on the gases O_2, N_2, and CO_2, as well as a plot of total residual gas pressure for reference. Figure 1-12 shows the carbon gases (CO_2, CO, and CH_4), again with total residual gas pressure for reference, and with a plot of total gaseous carbon species. Figure 1-11 shows a trend of N_2 mass loss with time over the entire period. The graph for total carbon species in Fig. 1-12 shows carbon mass loss beginning after about 2 to 3 weeks. The precision of the data makes the magnitude of this loss trend uncertain, but the total pressure curve is consistent with this trend.

Experiments done at higher DT fill pressures have confirmed the trends seen in the 2 atm DT-filled shells. In fills of 5 and 10 atm DT, total pressure of residual gas is down 30 to 50% from the original, as-made pressure, and the loss of residual gases beyond that due to oxygen is more obvious. The major fraction of this loss is from carbon species, which decline to about 50% of their original values in a few days in both 5 and 10 atm DT exposures. Nitrogen falls to about 70% of its original value in these same exposures. This is presented graphically in Fig. 1-13 (data on 5 atm DT fills) and Fig. 1-14 (data on 10 atm fills). Loss of carbon in the gas phase may result from several different mechanisms, operating singly or in concert. Some possible reactions are listed below.

Table 1-3. Partial pressures of glass shell residual gases, calculated from GC-derived total pressure values and volume percent compositions. Shells were exposed to 2 atm DT for various lengths of time. Far right column is the sum of the partial pressures of all carbon species.

Batch	Time (days)	O_2	N_2	CO_2	CO	CH_4	C_2H_n	$\Sigma(C_pX_q)$
T4R1220	As-made	0.0358	0.0140	0.1232	-	-	-	0.1232
T4R1220	1.9	0.0006	0.0102	0.0812	0.0180	-	-	0.0992
T4R1220	13.8	0.0004	0.0107	0.0843	0.0132	0.0015	-	0.0990
T4R1220	36.9	0.0004	0.0117	0.0899	0.0103	0.0049	(tr.)	0.1051
T4R1220	51	0.0002	0.0122	0.0787	0.0032	0.0057	-	0.0876
T4R1229	As-made	0.0347	0.0152	0.1081	-	-	-	0.1081
T4R1229	2.0	0.0011	0.0141	0.0833	0.0275	-	-	0.1108
T4R1229	44.1	0.0007	0.0113	0.0540	0.0080	0.0075	0.0019	0.0695

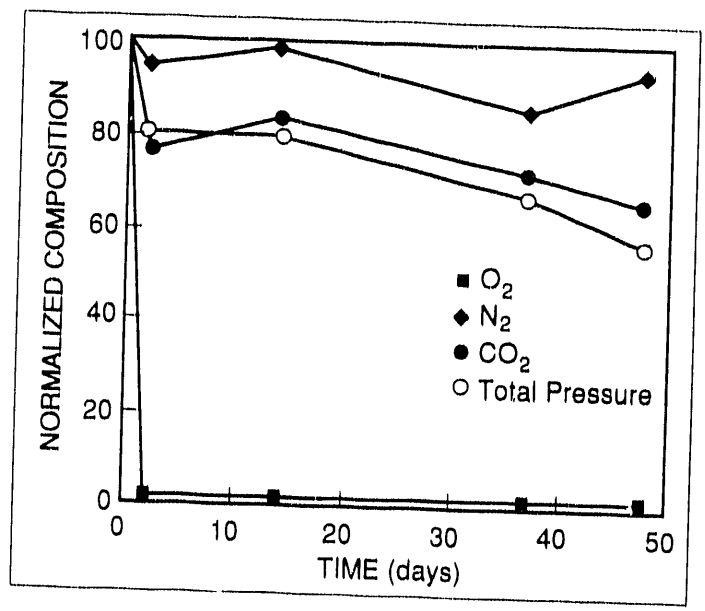

Fig. 1-11. Each component of the residual gas, O_2, N_2, and CO_2, is normalized to its original composition in as-made glass shells. The graph shows variation of this normalized composition with exposure time to 2 atm DT fuel gas. Normalized total residual gas pressure is also shown.

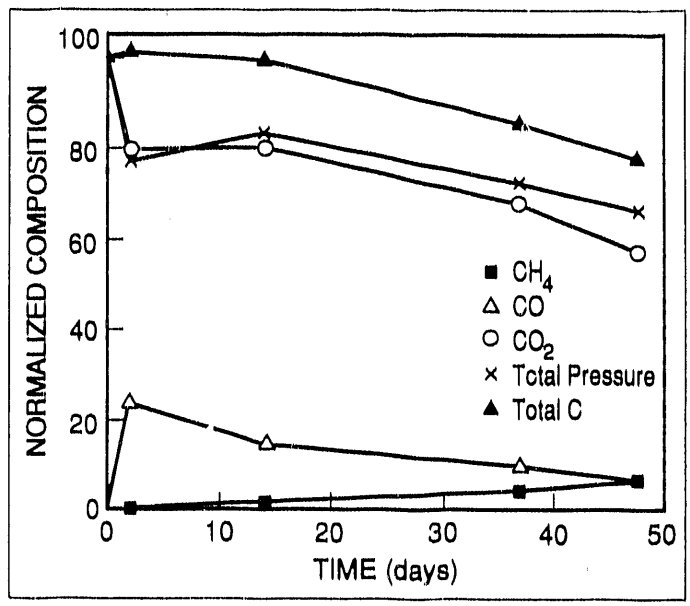

Fig.1-12. These carbon gases are normalized to the original composition of CO_2 in as-made glass shells, since the CO and CH_4 originate in the CO_2. The graph shows variation of this normalized composition with exposure time to 2 atm DT fuel gas. Normalized total residual gas pressure is also shown, along with a trace for total gaseous carbon species.

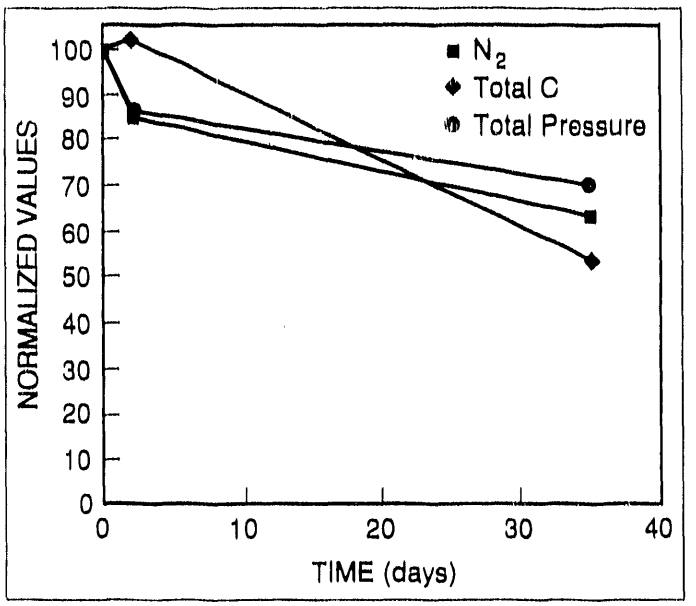

Fig. 1-13. Normalized data on residual nitrogen and total carbon gases in 5 atm DT-filled glass shells. Normalized total residual gas pressure is also shown.

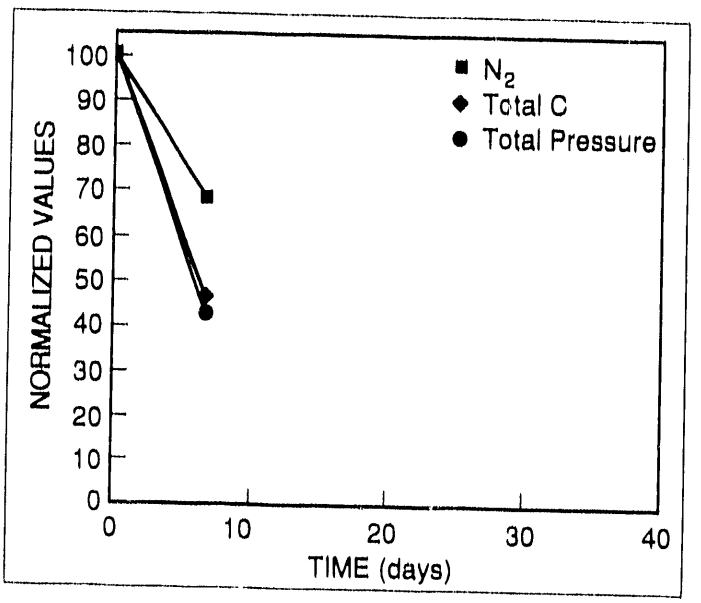

Fig. 1-14. Normalized data for nitrogen and total carbon residual gases in 10 atm DT-filled glass shells. Normalized total residual gas pressure is also included.

1. Combination of CO_2 with base compounds on the inner wall:

$$O_2 + 2H_2 \rightarrow 2H_2O$$
$$Si\text{-}O\text{-}M + H_2O \rightarrow SiOH + MOH$$
$$MOH + CO_2 \rightarrow MHCO_3,$$

where M = Na, K, Rb.

2. Disproportionation of carbon monoxide:

$$2CO \rightarrow CO_2 + C$$

3. Polymer formation. Both CH (Ref. 9) and CHO (Ref. 10) polymers have been reported to form under conditions found in filled shells.

All of these reactions deposit carbon on the inner surface of the shell in the form of bicarbonate, elemental carbon, or polymer. We have looked for this deposited carbon in shells exposed to DT for longer periods of time with our scanning electron microscope, but were unable to detect it. The quantity of carbon would be very small, probably distributed uniformly over the inner surface of the shells, and would be difficult to detect.

To summarize, quantitative analysis at longer storage times confirms that reduction reactions between residual gases and low-pressure DT fuel proceed slowly at room temperature. In 2 atm DT fills, oxygen is almost eliminated during the fill step and about 25% of the CO_2 is converted to the CO. Thereafter loss mechanisms are slow; after two months' storage, total pressure falls another 20%, mostly from loss of carbon, with some slight contribution from nitrogen. Experiments at 5 and 10 atm DT fills show faster reaction times for residual gases with DT and offer a promise of more complete reduction of residual gas contamination in the fuel. We will be examining shells stored for longer times with 2, 5, and 10 atm DT to expand our understanding of these gas reactions.

Error Considerations.

Gas Chromatography. One-point calibration was used for the GC, the reference gas being an analyzed mixture of O_2, N_2, CH_4, CO, and CO at 1,000 ppm each, from Scott Specialty Gases, Troy, Michigan. A one-time check, with a calibrating gas mixture of the same components at the 5% concentration level, gave similar response factors, indicating a linear calibration curve through the origin. In every analysis, calibration points were taken before, between, and after the shell gas analyses. Repeatability of response from the GC to the calibrating gas gave relative standard deviations of 1 to 3% for all calibration points on any given day. For over a year, GC response factors were constant to within ± 3% for CO_2, ± 5% for N_2, and within the range of 3 to 5% for the remaining gases. The calculated relative standard deviation for the volume percent composition data is 5.3% (Ref. 10). The error connected with GC-derived total residual gas pressure per shell derives principally from two factors.

1. Shells for analysis from T4R1218 and T4R1220 were chosen by eye to be in the 400 to 450 μm diameter range. However, sometimes most of the shells in a given sample were near the upper limit of this range, and other times most were at the lower limit. Thus, assuming an average o.d. in the sample of 425 μm for calculation of average pressure per shell will sometimes be in error.

2. The number of shells per analysis may be incorrect. This error derives from the difficulty of keeping track of over 100 shells during a protracted operation, and from the fact that some shells break, unseen, as they are loaded into the sample needle. (The possibility of shells not breaking in the GC is eliminated, since shards are examined when the needle is cleaned after a run. At most, one unbroken shell may occasionally be found, and it is subtracted from the total number of shells for that analysis.)

Pooling the standard deviations for all runs on DT-exposed shells yields a sigma value of 0.0135 atm, which gives a 90% confidence level of ±0.024 atm for the mean values.

GEVF Method. This total pressure test method requires two measurements with an optical microscope on shells immersed in glycerine: a reading of the shell i.d. before breaking it, and a measurement of the bubble diameter after breaking the shell to release the internal gas. Bubble measurement is straightforward since refractive index

effects cause the bubble to be clearly outlined. Measurement of shell i.d. is the largest source of error. While the index of the glass wall is closely matched by the index of glycerine, the necessity of viewing the i.d. obliquely through the glass wall material, which has its own optical aberrations, makes this the more difficult measurement due to blurring of the image. Errors in bubble measurements are <0.4%, while errors for shell i.d. are ≈1%.

We have investigated the solubility of fuel gases and residual gases in glycerine. Hydrogen and its isotopic combinations are insoluble, as are O_2, N_2, CO, and CH_4. Carbon dioxide is slightly soluble in glycerine, but over the duration of the measurement (20 s), minimal amounts dissolve, so this potential error in GEVF total residual gas pressure measurements is reasonably ignored.

For additional information, please contact Matthias Ebner

1.2 Cryogenics and Tritium Technology

During the reporting period, KMS Fusion (KMSF) continued its work in the simulation of the β-heating process and extended its previous experimental work in the optical characterization of frozen fuel layers. In addition to these activities, KMSF provided assistance with the experimental program at Los Alamos National Laboratory (LANL) to observe the effects of β-heating on DT ice layers near their thermodynamic triple point.

1.2.1 Beta-Heating Modeling Studies

Simulating β-layering in Cryogenic Targets Cooled by Convection and Conduction. We have developed a three-dimensional model of heat transport via free convection and conduction. The equations governing free convections are[13] listed below.

1. Momentum equation:

$$\rho\vec{V}_t + \rho(\vec{V}\cdot\nabla)\vec{V} = -\nabla P + \nabla\cdot\tau(\vec{V}) + \rho\vec{g},$$

where ρ is density, $\vec{V}$ is the velocity vector, P is pressure, τ is the viscosity stress tensor, and $\vec{g}$ is gravity.

2. Heat equation:

$$T_t + \bar{V} \bullet \nabla T = \chi\{\mathrm{div}[k(T)\nabla T] + q\},$$

where T is temperature, $\bar{V}\bullet\nabla T$ is the convective term, $\chi = 1/(\rho C_p)$, $\mathrm{div}[k(T)\nabla T]$ is the usual term for conductive heat transport, q is the heat source (= β-decay), C_p is the specific heat at a constant pressure, and k(T) is a nonlinear conductivity coefficient.

3. Continuity equation:

$$\rho_t + \mathrm{div}(\rho \bar{V}) = 0,$$

where $\rho_t = 0$ in an elastic approximation.

In these equations, exponentially accurate spectral methods are used. The variables $\bar{V}$, T, and ρ are expanded in orthogonal systems of Chebyshev polynomials in radius and spherical harmonics in angular variables. For example,

$$T(r,\varphi,\xi,t) = \sum_{n=0}^{Nr} \sum_{l=0}^{N\varphi} \sum_{m=-1}^{l} a_{lmn}(t)\, C_n(r)\, Ym_{l(\varphi,\xi)}$$

where $C_n(r)$ is the nth Chebyshev polynomial and $Ym_{l(\varphi,\xi)}$ is the spherical harmonics of order m and degree l. Time differencing is similar to the method in Ref. 14.

Nonlinear terms in the above system are calculated in physical space, then transformed to spectral space using a spherical harmonic transform package, Spherepack.[15]

Our computer code implementing these mathematical methods includes subroutines for the heat, momentum, and continuity equations, as well as transform, initial value output, coefficient, and time-marching routines.

We are currently applying this model to β-layering in cryogenic DT ice targets cooled by an exchange gas with pressure high enough to provide significant convective cooling (see Fig. 1-15).

In compressible fluid flow, the evolution of the flow patterns can depend in complex ways on the initial velocity and temperature profiles. We are experimenting with

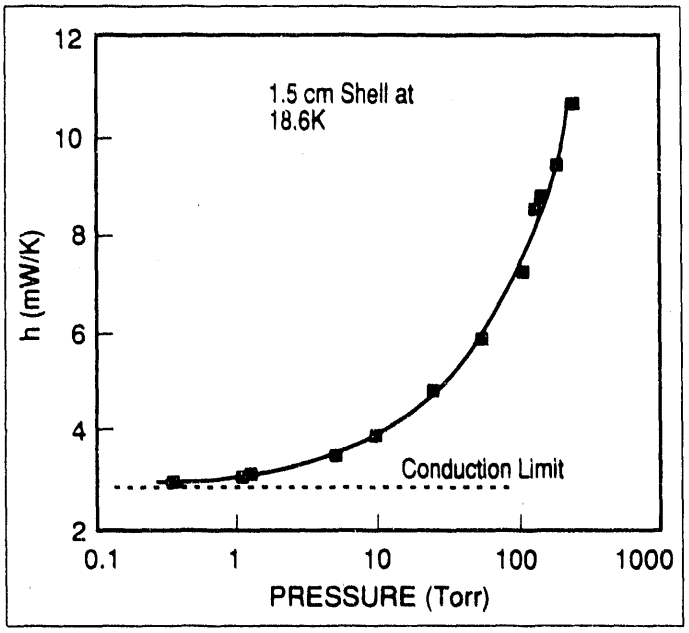

Fig. 1-15. Convection dominates as a heat-transport mechanism at pressures greater than about 1 Torr. Here, power is approximately equal to $h\Delta T$. The data are from Evan Maypoles, Lawrence Livermore National Laboratory.

carefully chosen initial conditions (Fig. 1-16) to study the stability and uniqueness of the flow evolution.

To illustrate complex flows and make comparisons to other free convection results in the literature, KMSF has developed three-dimensional color graphics software (see Fig. 1-17). Features include shading, variable-flow ribbon size, and variable perspectives.

An application we are just beginning to develop is including DT ice layer movement in the evolution from initial to equilibrium state (Fig. 1-18). This requires us to address issues like mass transport in the interior vapor region and the possibility of multiple equilibrium states for both flow and ice-layer shape.

For additional information, please contact Stephen Wineberg

1.2.2 Holographic Studies of DT Ice Layers

We have continued to develop sandwich holography as our primary optical diagnostic to determine the geometry of fuel distributions resulting from the β-layering process. In the KMSF 1989 Annual Technical Report[16] we reported that the fringe patterns in our holographic interferograms become symmetric as the solid DT is redistributed due to β-decay heat. The symmetry of those patterns is consistent with that expected from a uniform solid layer. Our recent work has been directed toward obtaining further evidence that a uniform solid DT layer forms during our β-layering experiments.

The interferograms shown in the 1989 Annual Technical Report were all obtained along a single viewing axis. A single-axis view is not conclusive evidence for a uniform solid layer. Symmetry can be present in a single axial view of a target while a second (orthogonal) view demonstrates a high degree of nonuniformity.[17] Succinctly stated, a single radially symmetric interferogram implies, at most, cylindrical symmetry.

To address this issue, we have performed experiments on β-layered DT distributions employing two widely separated viewing axes. Since our present apparatus has a single viewing axis, we rotate the capsule once the solid layer has become symmetric to obtain the second view. Two holograms, one with the fuel in gas phase and a second with the fuel in solid phase, are needed to evaluate the DT distribution. We obtain the needed

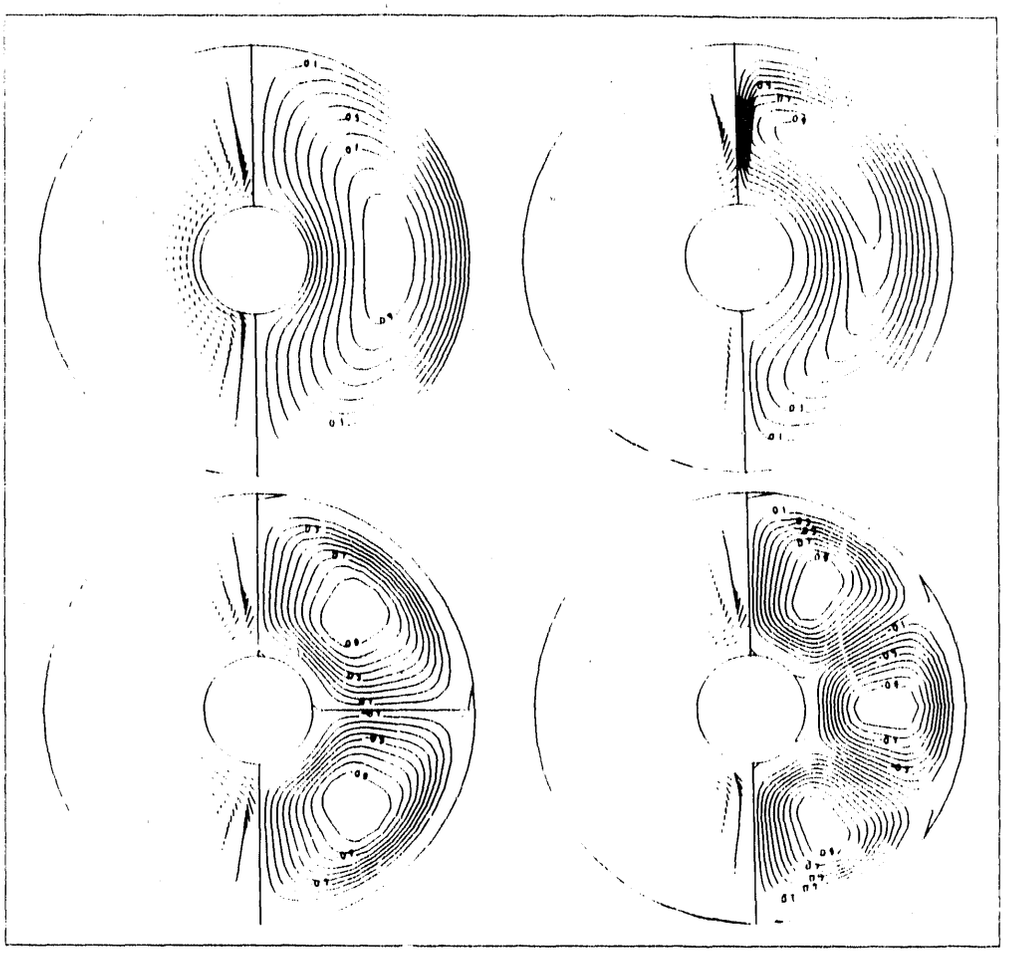

Fig. 1-16. We are studying the evolution of flow and temperature distributions from a variety of axisymmetric initial conditions.

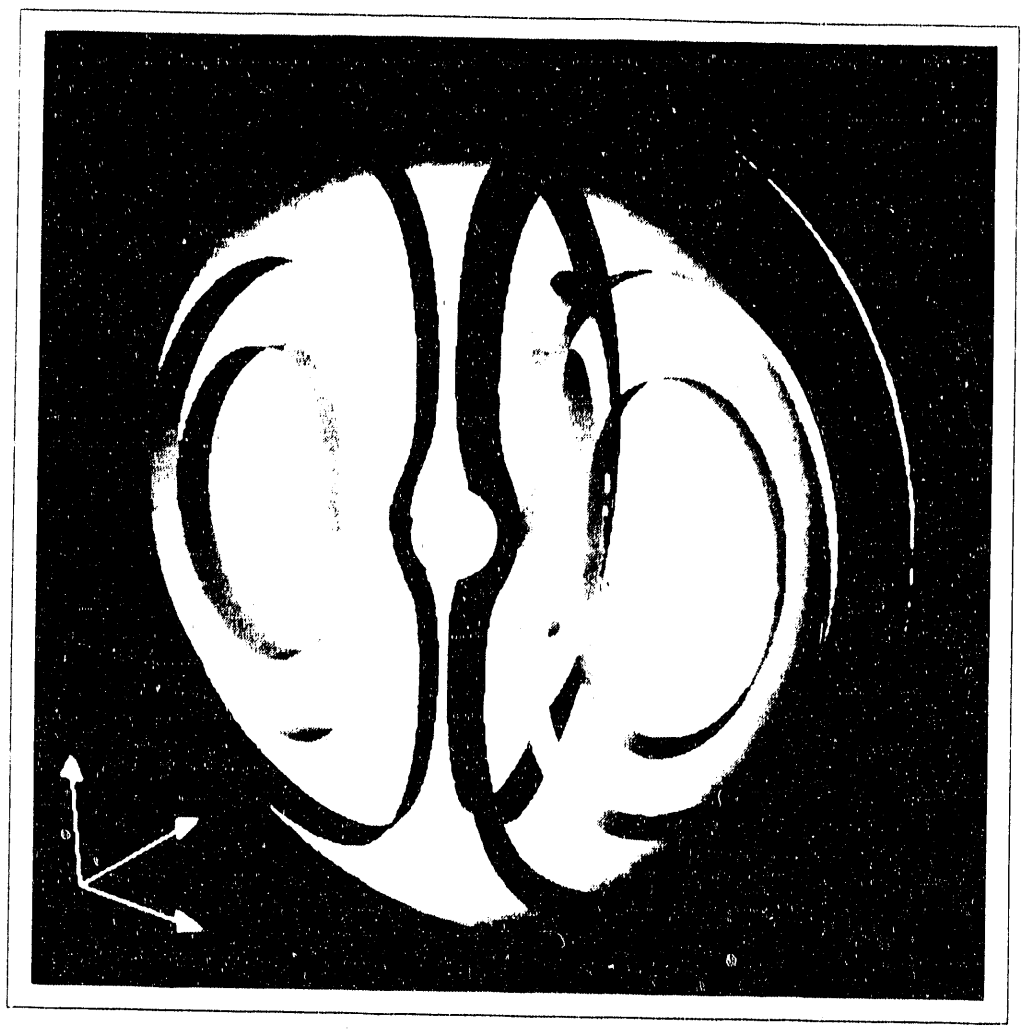

Fig. 1-17. Representation of a three-dimensional color illustration of free convective flow patterns.

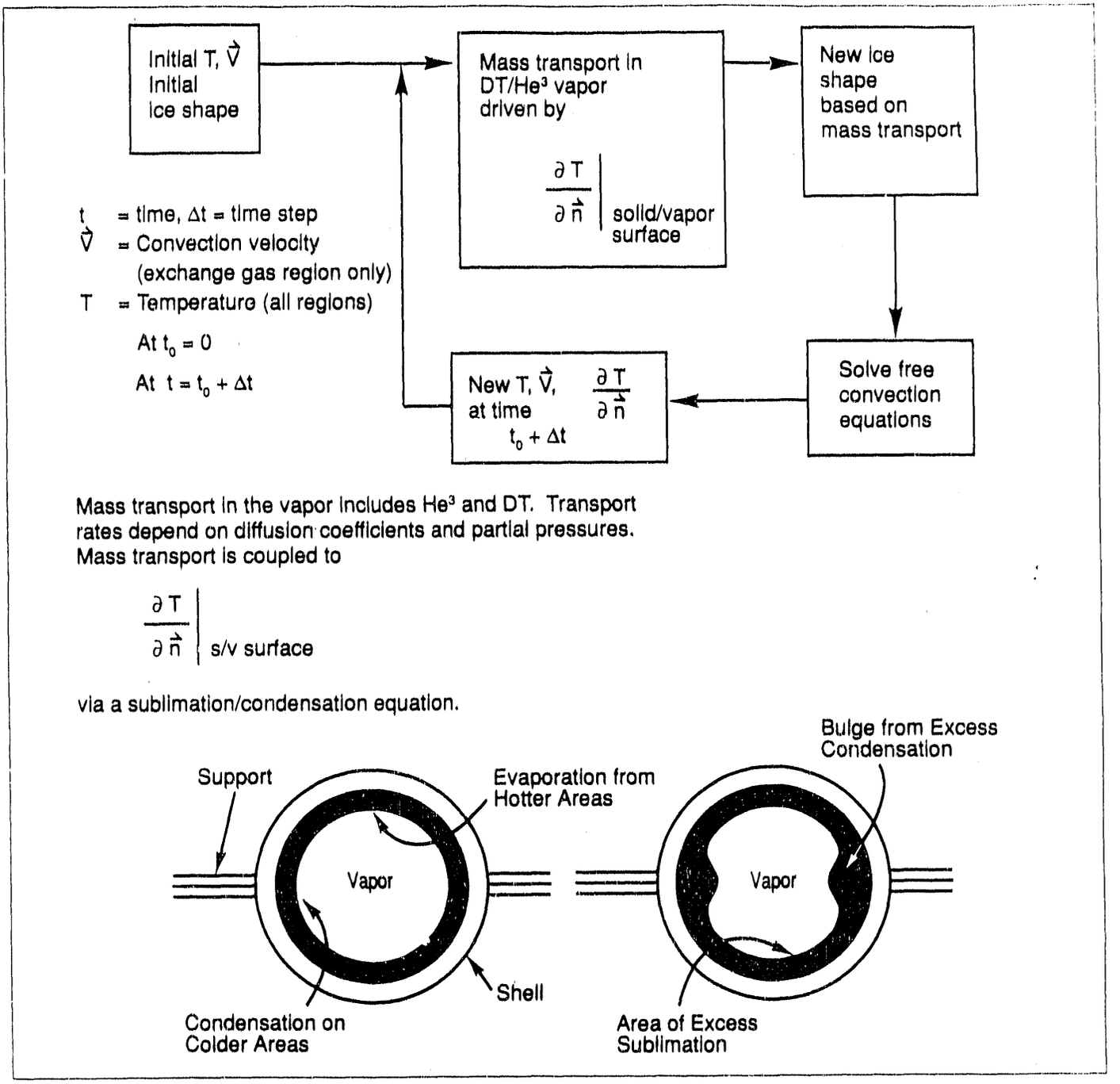

Fig. 1-18. Time-dependent simulation of β-layering with a convection/conduction model.

holograms in the following manner:

1. Obtain the first gas phase hologram.

2. Admit helium exchange gas[18] and allow the DT to become symmetric (additional holograms are made during this process).

3. Make a hologram of the symmetrical solid distribution.

4. Rotate the capsule approximately 75° and make another hologram of the solid distribution.

5. Evacuate the helium exchange gas and allow the DT to return to gas phase due to ß-decay heat (additional holograms are made during this process).

6. Obtain a gas-phase hologram for the rotated view.

We have performed experiments starting with both the normal view and the rotated view. The capsule mounting configuration (Fig. 1-19) prevents us from recording two orthogonal views, since one viewing axis is chosen to be normal to the mounting frame to allow the least obstructed view.

At the end of the experiment we have a gas-phase and a solid-phase hologram for both views. We combine the reconstructed wavefronts from the gas phase and the solid phase to form an interferogram, which gives information on the uniformity of the solid layer.[19] Gas-phase/solid-phase hologram pairs from both views can be used to form holographic interferograms using the micropositioner we have built specifically for this purpose.[16] The results of one of these experiments are shown in Fig. 1-20. Both the normal and the rotated views show the concentric circular interference fringes, which indicate a fuel distribution that is symmetrical about the viewing axis. Although the rotated view shows more refractive features, which make the fringe pattern difficult to distinguish, these fringes can be identified easily when the interferogram is phase-shifted by moving one hologram slightly with respect to the other during reconstruction. The presence of two symmetric circular interference patterns about two widely separated axes removes the ambiguity inherent in single-axis viewing and supports our position that the DT solid is distributed in a uniform solid layer.

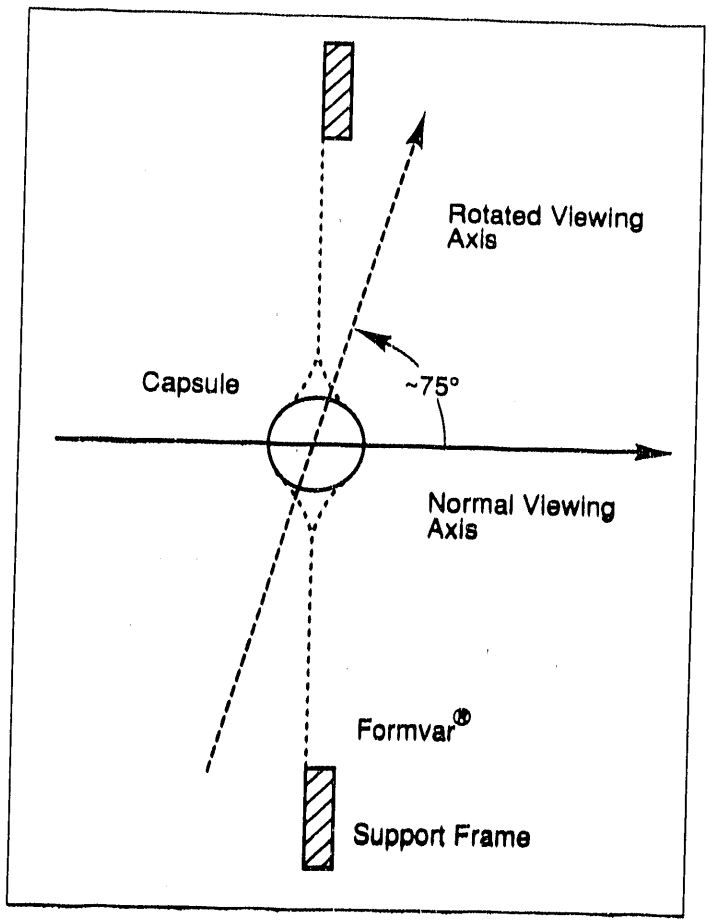

Fig. 1-19. Diagram of the capsule mounting configuration, showing the normal and rotated viewing axes.

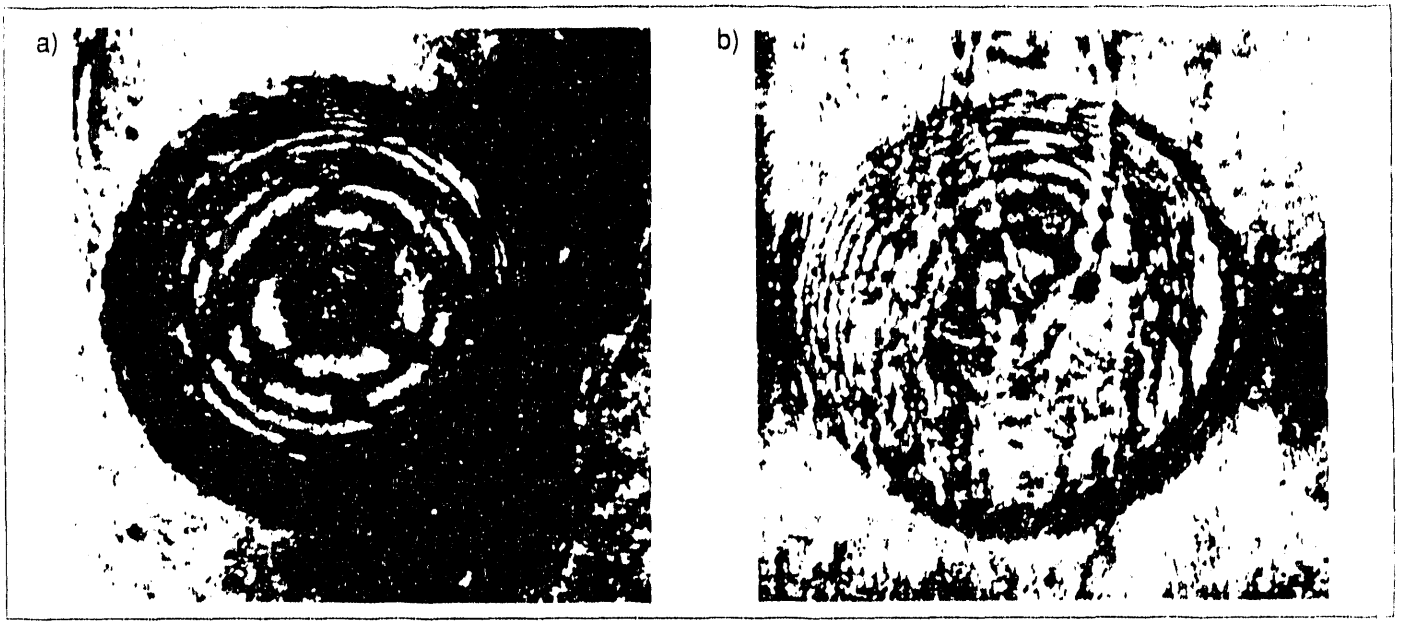

Fig. 1-20. Concentric circular fringe patterns are seen along both the normal (a) and rotated (b) viewing directions. The shell in these interferograms has an o.d. of 880 μm and a wall 7.5 μm thick. It is filled with 80 atm DT.

In addition to the dual-axis views, we have studied liquid-phase/solid-phase interferograms. These compare the solid distribution to that of a liquid layer. When the fuel is in the solid state or a liquid layer just above the triple point, there is little mass remaining in the vapor. Therefore, reconstruction of a liquid-phase with a solid-phase hologram will give an interferogram that indicates the differences between the liquid and solid distributions. The case of interest is the interferogram of a slumped liquid layer and a solid distribution. A slumped liquid layer is symmetric about the gravitational axis (the vertical axis in Fig.1-21). A uniform solid layer is spherically symmetric. If the solid is distributed as a uniformly thick layer, the liquid-phase/solid-phase interferogram should then be symmetric about the gravitational axis. The interferogram that results when the wavefront from a slumped liquid layer (Fig. 1-21a) interferes with that from the solid distribution (Fig. 1-21b) shows linear fringes traversing the capsule perpendicular to the gravitational axis (Fig. 1-21c). The left-to-right symmetry of these fringes implies that the solid distribution is symmetric left-to-right about the vertical axis. Also, the interferogram clearly shows a localized nonuniformity in the solid layer (upper left of the capsule in Fig. 1-21c). This feature corresponds to a feature in the gas/solid interferogram (Fig. 1-21b) that does not show discernible fringes. The fringes are visible in the solid/liquid interferogram because the wavefronts from the solid and the liquid in that area of the capsule are sufficiently similar to give a fringe spacing above the 10 μm resolution limit of our optical system. The presence of this feature 23 hours after the onset of solidification implies that, although ß-layering is giving a symmetrical solid distribution (as evidenced by the concentric circular interference patterns), localized nonuniformities persist.

The light used to make the holograms is coherent. Thus, an obstacle in the beam causes noise due to diffraction.[20] This fact can be used to determine that a given layer contains solid DT. We have noted that the concentric fringe patterns obtained from solid layers thicker than about 10 μm develop considerable noise as time progresses.[21] Comparison of the fringe patterns within a shell containing aged DT solid (Fig. 1-22a) with the fringe patterns obtained from the same shell containing liquid DT (Fig. 1-22b), as well as with the background interference patterns of the interferograms themselves (for example, the background fringes in Fig. 1-22b), shows that the patterns within the capsule containing solid are definitely noisier. The noise is present in all areas of the capsule. The only causative agent for this noise is solid

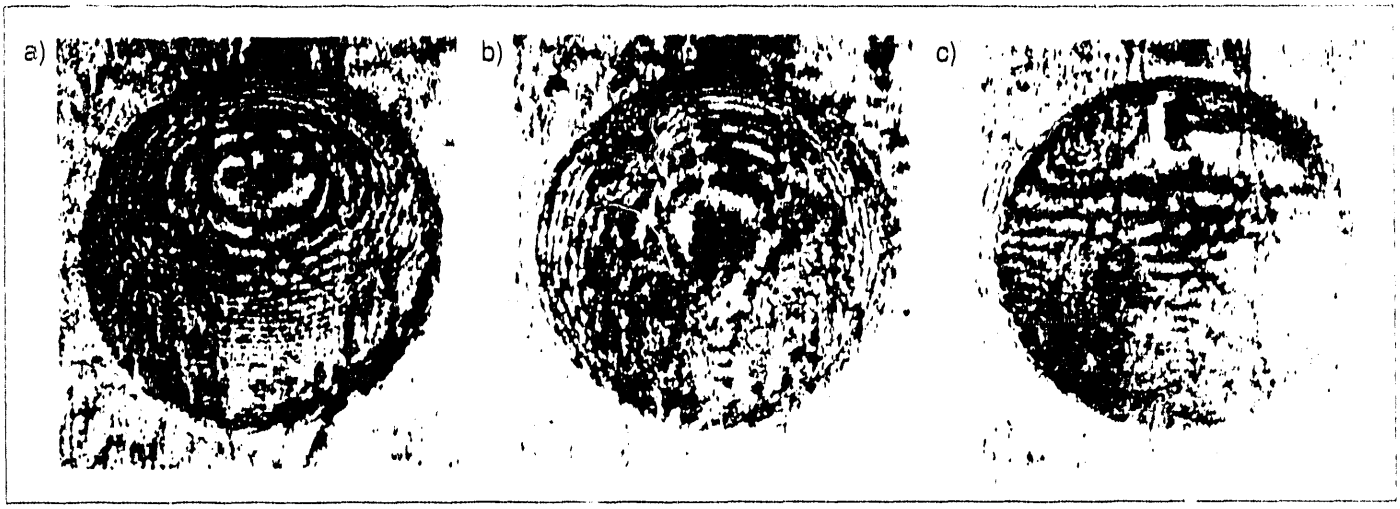

Fig. 1-21. When the wavefront from a liquid layer (a) interferes with that from a solid layer (b), linear fringes are formed (c). Left-to-right symmetry of the fringes implies left-to-right symmetry of the fuel distribution. (Interferograms in [a] and [b] are formed by interfering with the reconstructed wavefront from gas phase.) The shell in these interferograms has an o.d. of 880 μm and a 7.5 μm thick wall. It is filled with 80 atm DT.

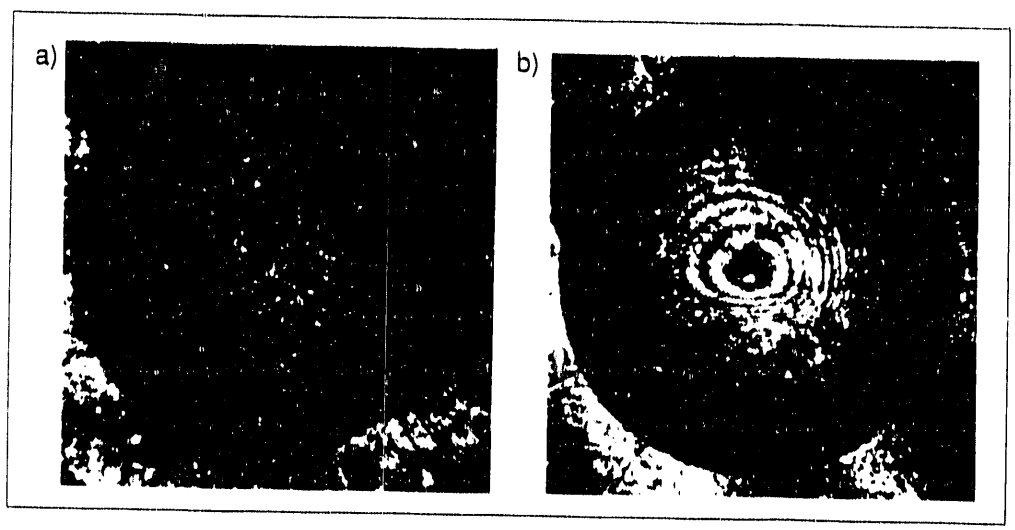

Fig. 1-22. Noise develops throughout a capsule containing solid DT (a). The interferogram on the right (b) is of a liquid layer formed earlier in the same experiment. The shell in these interferograms has an o.d. of 3750 μm and a 176 μm thick wall. It is filled with 75 atm DT.

on the capsule wall. The presence of increased noise confined to the region within the shell containing an aged solid layer indicates that fuel is distributed on the capsule wall.

The presence of solid in a symmetric layer on the capsule wall is indicated by the presence of specific recognizable features in shadowgrams of the solid layer that map to areas of concentric fringes on the interferogram. The arrows in Fig. 1-23a point to bright features that were not seen before the DT solidified. These features indicate that DT ice is present. The subsequent observation, upon interference with a gas-phase hologram, of smooth, unbroken arcs of concentric circular fringes through the same areas indicates that fuel is distributed symmetrically in that region. The arrows in Fig.1-23b point to the regions corresponding to the features indicated in Fig. 1-23a. Concentric circular fringes indicating a symmetric fuel distribution are seen in each case.

To summarize, we now have four separate observations that indicate either that the solid distribution is symmetric, or that it is distributed in a layer on the capsule wall, or both:

1. Concentric circular fringes seen in two widely separated views are consistent with a spherically symmetric solid distribution.

2. Solid-phase/slumped-liquid-phase hologram pairs indicate left-to-right symmetry of the solid distribution.

3. "Optical noise" or haze developing in the aged solid distribution indicates the presence of a solid layer on the capsule wall.

4. Correlation of specific features in shadowgrams, which indicate the presence of solid, with areas of concentric fringes in interferograms, which indicate a uniform distribution, shows that there is a symmetric solid layer in these areas.

These observations make a good argument for the presence of uniform solid DT layers in these capsules.

Fig. 1-23. Recognizable refractive features (a) map to areas of concentric circular fringes in the interferogram (b). The shell in these photographs has an o.d. of 915 μm and a 11 μm thick wall. It is filled with 75 atm DT.

As has been noted above, refractive features are present when the DT is in the solid phase. These features obscure the interference fringes in parts of the capsule. Once the solid distribution has formed, most of these refractive features are stable in time. Furthermore, these features are not reproducible from one experiment to the next, as would be the case if they were uniquely associated structures on the inner wall of the capsule.[22] There is, however, evidence that some of the refractive features are associated with the Formvar® mounting film. The rotated view allows better observation of the regions where the Formvar® first contacts the capsule. More refractive features are consistently seen in the rotated view than in the normal view, in which much of the information from the regions where the Formvar® first contacts the capsule is lost.[23] This observation suggests that the mounting film may be having an effect.

To test this hypothesis further, we conducted two experiments with a capsule mounted between two Formvar® films with holes, so that the capsule contacted the film only near its base. In both experiments a U-shaped refractive feature was seen to form where the mounting film contacted the capsule. Figure 1-24a shows the capsule within the mounting film. Since the capsule in Fig. 1-24a contains only a small amount of liquid, the region where the film contacts the capsule and the details of the film are clearly visible. Figure 1-24b shows the same capsule with the DT in the solid phase. While some refractive features are scattered throughout the capsule, a large feature obscures the entire area where the 300 nm thick Formvar® film contacts the capsule. Since this happened in two separate experiments, it seems that the mounting film is affecting the distribution of refractive features. We are currently pursuing alternative mounting configurations to minimize the effect of the mounting fixture.

One possible explanation for the refractive features is based on earlier observations of gaseous contaminants (i.e., CO_2, O_2, and N_2) within similar capsules.[24] These contaminants solidify at higher temperatures than DT and could be transported as small crystallites within the DT liquid. As the DT crystallizes, these contaminants can be excluded. Concentrations of many fine contaminant crystallites along DT grain boundaries could account for the nonrepeatable refractive features we observe. As part of our effort to eliminate refractive features, contaminants will be minimized in future work.

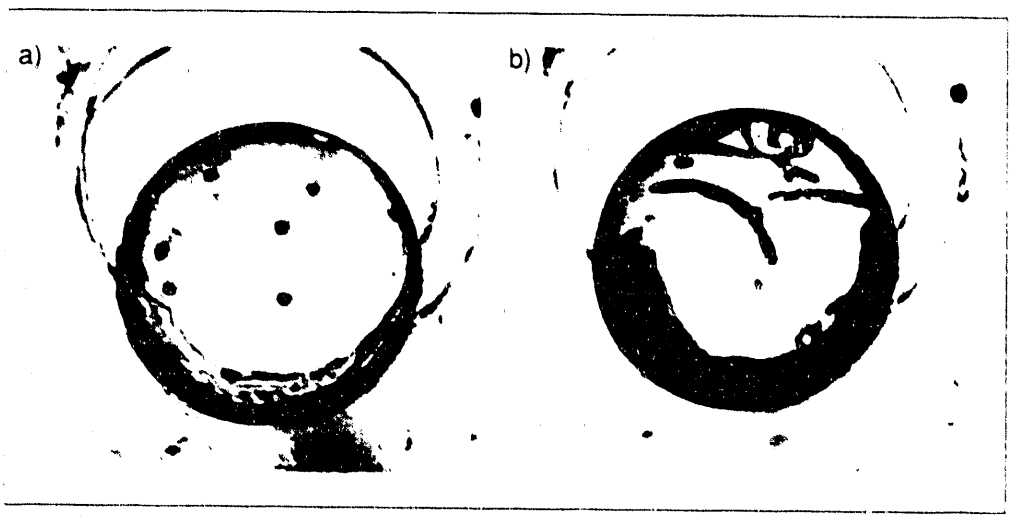

Fig. 1-24. A U-shaped refractive feature forms where the mounting film contacts the capsule: thin liquid layer, showing detail of the mounting film (a), solid distribution (b). Incoherent light was used for these photographs. The shell in these photographs has an o.d. of 880 μm and a 7.5 μm thick wall. It is filled with 80 atm DT. The mounting film is 300 nm thick.

While we feel that this is the explanation for the refractive features we observe, and that the underlying fuel distribution is uniform, other interpretations of our results are possible. Chief among these is that most of the solid is localized in the regions of the refractive features that obscure the interference fringes. In this case the underlying concentric circular pattern we observe is due to the (necessarily) uniform gas distribution interfering with regions within the capsule where little or no solid is present.

To improve our experimental capabilities, we are currently building a dual-axis holographic diagnostic station with a cryogenic refrigerator. This system will allow us to control the capsule temperature and obtain better optical data. For example, if the fuel were distributed in lumps or crystals, closely spaced fringe patterns indicating rapidly increasing solid thickness would be present in these areas. We plan to employ diffraction-limited f/2 documentation optics, which will give 1 to 2 μm resolution. Compared to the current system, which gives about 10 μm resolution, the new system will give us better information about the fuel distribution, especially in areas where the interference fringes are closely spaced.

For additional information, please contact Janet Ankney

1.2.3 Experimental Design Considerations

The national ICF program continues to focus on the β-layering process for forming uniform solid layers of DT inside spherical capsules. During the reporting period we embarked on an ambitious program to maintain and enhance our experimental capabilities for studying DT layers.

The apparatus we use to study the β-layering effect inside glass shells is configured as a classical cryogenic insert suitable for immersion into a liquid helium bath.[25] The liquid helium provides an exceptional isothermal environment. Unfortunately, the saturation temperature of liquid helium at atmospheric pressure is 4.2K, whereas the β-layering process proceeds most rapidly at temperatures only slightly below the triple point of DT (19.8K). Therefore, in practice, we attempt to maintain the temperature of the capsule only slightly below the triple point by balancing the internal heat generation of the fuel layer against the cooling effect of a low pressure helium exchange gas in the experimental chamber. Lack of precise temperature control has become an increasing concern as our experimental program has progressed. Variations in temperature after a

DT layer becomes solid can thermally induce stress cracks. This could help explain the degradation in quality of the interferometric holograms we have been obtaining after the DT fuel becomes solid.

Along with the desire to improve the quality of our holograms, we would like to increase the speed of our primary imaging optic and provide simultaneous views. Increasing the speed of the optics would improve the resolution of our holographic system. Obtaining two simultaneous views of the capsule along orthogonal axes would add valuable information to aid in interpreting the condition of the fuel layer. Unfortunately, it is not possible to easily retrofit the current apparatus to improve the optical system.

Concurrently, we are performing x-ray phase probe studies[26] that could lead to the development of an interesting new diagnostic for understanding the β-layering process. In brief, we have found that it is possible to monitor the thermodynamic phase of the DT fuel inside glass shells remotely by examining the soft x-ray signal emanating from them. We were able to perform a proof-of-principle experiment on our current ß-layering apparatus, but found the retrofit impractical for routine use because of the low signal-to-noise ratio and the operational hardships in attempting to use the insert in a manner for which it was not originally designed.

Our desire for better temperature control and improved optical imaging along orthogonal axes, along with our desire to explore further the x-ray signal emanating from a shell, has motivated us to begin the design of a new β-layering apparatus. The fundamental new feature of the design is the use of a mechanical refrigeration system for the production of the cryogenic environment, rather than the boiling helium bath in our previous design. To this end we have chosen a Cryomech model GB37 cryogenic refrigerator, which can provide 60W of refrigeration at 70K on its first stage and 25W at 20K on its second stage. In our new design we are incorporating a temperature control system to accurately maintain the experimental chamber at the desired temperature. We are also attempting to allow for an f/2 primary imaging optic along two orthogonal axes. Finally, we are attempting to maintain, if not improve, the signal-to-noise ratio of our low-energy x-ray detection scheme by using a commercially prepared low-energy scintillator/photomultiplier tube detector (Bicron 2XM.040/2BLP).

The most pressing design concern at present is the mechanical vibration created by the physical cycling of the refrigerator's internal components. During the reporting period, we attempted to quantify both the magnitude and frequency of the vibrations. The mechanical vibrations present a serious challenge to the holographic diagnostic for two reasons. First, the capsule will not be in the same physical space every time a hologram is taken (making the background phase gradient fiducial of paramount importance), and second, unless the shutter speeds are fast relative to the motion, the holograms will be blurred. We have performed a simple experiment to measure the magnitude of the vibration problem. With the refrigerator mounted in the experimental chamber, we used a crudely collimated white light source to backlight a cylindrical calibration rod, mounted where the target normally would be, projecting from the refrigerator's second stage (the shell-mounting platform). A simple microscope, compatible with the chamber's flanges, was used to form a sharp optical image (shadow) of the lower edge of the calibration rod on a white screen. We placed a photodiode in the vicinity of the shadow's edge, and observed the change in the signal as the motion of the rod moved the shadow across the sensitive surface of the photodiode detector. The electrical signal produced by the photodiode was displayed on an oscilloscope for analysis. The oscilloscope trace revealed that the motion of the second stage of the refrigerator fall into two distinct domains: a gross translational motion of approximately 30 μm total deflection at intervals of roughly 1 Hz, and a second, higher-order motion superimposed on the gross deflections. We noted that the superimposed vibrations almost completely disappear at certain recurring intervals. Therefore, our next objective will be to search for a repeatable timing fiducial for triggering the exposures so that they occur during periods of relative inactivity and nearly identical position.

We have decided upon the conceptual strategy that will be used for the fabrication of the next-generation β-layering apparatus. A capsule, sandwiched between two thin films of Formvar®, resides inside the innermost of three cylindrical containers. The container is made from oxygen-free, high-conductivity (OFHC) copper. Four sapphire windows allow for the optical observation of the capsule along two orthogonal axes, while a 0.020 in. thick beryllium window at the bottom permits the low energy x-rays to pass through to our room-temperature detector. A machined OFHC copper web mechanically reinforces the thin beryllium. Although optically baffled to prevent perturbations in

the isothermal environment, the atmosphere in this (first) container is common with the immediate outer (second) container. A thin-walled fiberglass/epoxy tube on the flange of the second container supports the innermost container.

The second container is nearly identical to the first except for two important differences. First, it is intended to be leak-tight. Indium foil will be used for cryogenically sealing the container. Second, this enclosure is to be thermally attached to the second stage of the cryogenic refrigerator. A thermometer and heater will be placed on this container to provide a means of measuring and controlling the temperature of the enclosed volume.

The third cylindrical container is attached to the first stage of the cryogenic refrigerator, and functions as a 70K radiation shield. It is intended to provide a thermal radiation barrier between the 300K room-temperature environment and the 20K experimental environment. The outermost cylindrical container is the vacuum chamber. It does not require a thin beryllium window for the low energy x-rays since our detector can be used in a vacuum environment.

In our approach we perceive three areas of engineering risk: (1) use of large diameter (up to 2.0 in.) sapphire windows optically cemented to a thick copper substrate with a known differential thermal contraction coefficient, (2) use of thin beryllium windows epoxied to a copper substrate, which also has a known differential thermal contraction coefficient, and (3) reliance upon a thin washer of indium foil to provide a leak-tight and reliable seal as the apparatus is cycled between room temperature and cryogenic temperatures. To minimize our engineering risk, we are in the process of constructing a simple test piece to examine the three major areas of concern. At the same time we are proceeding with the more detailed and meticulous design of the actual experimental apparatus, being prepared to make changes as the subsequent testing may mandate.

For additional information, please contact Michael Mruzek

1.3 Capsule Fabrication

Two aspects of the work of the Capsule Fabrication Group are reported here. These are (1) the continuing work to improve polymer fuel containers and (2) the fabrication of glass fuel containers of large volume. The work on plastic fuel containers is dictated by both near- and long-term interest in low-density capsules, while the work on large glass containers is needed to fulfill an immediate need in the inertial confinement fusion (ICF) program.

1.3.1 Polymer Fuel Containers

Introduction

Our primary objective for this year is to improve shell wall uniformity. We are closely scrutinizing all aspects of the drying column process for capsule formation to identify the conditions that influence uniformity. We have also initiated a modeling effort to support our experimental work with drying columns. We are simultaneously evaluating microencapsulation as an alternative capsule-fabrication technique. This process can produce capsules in useful size and wall thickness ranges, and with good wall uniformity. However, small voids (vacuoles) in the walls are a persistent problem. We have identified a mechanism for vacuole formation, and have made significant progress toward reducing the number of vacuoles produced with this process.

The polymer solution droplets that are formed into polystyrene (PS) capsules in the drying column are produced by a stripping gas droplet generator (SGDG). Before we could begin systematic experiments to identify the drying column process parameters that affect the wall uniformity of PS capsules, we had to stabilize the SGDG so that we could produce repeatable runs. The effects of process parameters on wall uniformity cannot be determined without precise control of the droplets that constitute the input for the process.

Demand also exists for composite PS/poly(vinyl alcohol) (PVA) capsules (that is, PS capsules with PVA coatings) which combine the desirable qualities of both polymers. Experiments with the composite capsule-fabrication process, combined with results from modeling studies, have defined practical limits for our present equipment in terms of the largest composite capsule that can be fabricated. Near-term target requirements are likely to exceed the capabilities of our present system. Also, our options for

improving coating uniformity are limited with the present equipment. We are therefore designing a new system that will meet both the near-term and anticipated future needs.

The fabrication processes for PS and PVA/PS shells involve several physical processes and many experimental parameters that can be varied widely. To develop an understanding of these processes and to guide experimentation, a theoretical model is under development at KMSF to model the drying column formation of PS shells and the fabrication of composite shells. The objective is to improve shell and coating uniformity. Modeling will help achieve this objective by narrowing the range of experimental conditions tested, suggesting new approaches, and helping interpret experimental results. Models of the mechanisms that cause or might prevent nonuniformity are to be added in future work.

Droplet Generators and Drying Columns

Fabrication (polystyrene). The dimensions of the shells required to support the ICF program are 230, 360, 445, and 510 μm in o.d. with walls 2 to 4 μm thick. We have made all of these sizes previously, but our runs were not repeatable. The lack of repeatability was attributed primarily to insufficient precision in the control of process parameters.

Solution injection rate is an important parameter because it, along with the flow rate of the stripping gas, determines the size of the droplets that are injected into the drying column. A new syringe pump was installed to improve control of the injection rate. The pump utilizes a PID controlled zero-cog DC motor. The system is capable of using 50, 100, 500, and 1000 μl gas-tight syringes. The injection speed is variable from 0.15 to 88.19 μl/s, selectable in 0.01 μl/s increments. Depending on the syringe used, steady-state volumetric flow is approximated from 9×10^{-5} to 2×10^{-3} μl/s. The new syringe pump has made injection rate selection accurate and repeatable.

To break the injected PS stream into drops, a stripping gas is required. We use nitrogen for the stripping gas. Methylene chloride is incorporated into the stripping gas to keep the polymer from drying on the injection needle. The methylene chloride adds mass to the stripping gas, thus affecting the drop size. As the nitrogen is passed over the methylene chloride, the methylene chloride cools. As it cools, less methylene chloride is added to the stripping gas. The stripping gas becomes less dense and the drops increase in size. To control this problem the methylene chloride was placed in a three-necked flask (see Fig. 1-25).

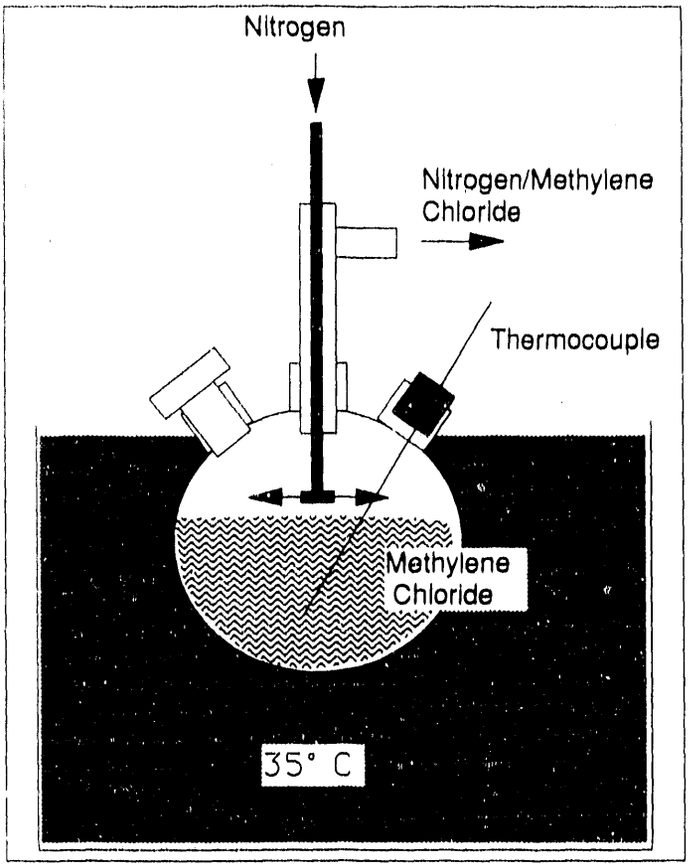

Fig. 1-25. Schematic illustration of the arrangement for dissolving methylene chloride in the SGDG stripping gas for PS capsule fabrication: The nitrogen is passed in and out of one neck. The second neck is used for a thermocouple to record the methylene chloride temperature. The third neck is a fill port. The flask is immersed in a water bath up to the necks. The water bath is set at 35°C. Before a run, the stripping gas is started. When the temperature of the methylene chloride stabilizes (usually 5°C below water bath temperature) the run is started. The flow rate of the N_2/methylene chloride is recorded.

A third parameter we adjusted was the drying column temperature profile. In the past, we have used a "ramping" profile. We would gradually increase the temperature, then decrease it. There are some advantages to this approach; however, the actual temperature within each zone must be controlled precisely. Our system currently uses thermocouples mounted between the heaters and the outside wall of the drying column. If a cool zone is located above a warm zone, the heat rises and affects the cooler zone. With the thermocouples located outside the tube, the actual temperature in the zone is unknown. Small shifts from run to run added to the overall instability. Until we can control the temperature in the zones, we have opted for a "block" profile, where the entire tube is heated to one temperature. This has eliminated temperature shifts.

The control gained over the injection rate and stripping gas flow rate, along with the stable temperature zones, has allowed us to derive a fairly linear relationship between polymer concentration and shell o.d. We kept the following parameters constant: injection rate (6.00 µl/s), nitrogen flow rate (1.32 l/min), methylene chloride/nitrogen flow rate (1.82 l/min), and temperature (220°C). The graph in Fig.1-26 shows the relationship between polymer concentration and shell o.d.

It is our belief that these data represent only a small part of the entire picture. These parameters allow us to produce the desired ICF targets reliably and repeatably. However, as the concentration of the polymer changes, viscosity changes, thus the drop size also changes. This accounts for part of the o.d. shift. Even though a variety of shell sizes are possible with these parameters held constant, the optimum solution concentration is around 2.7%.

Control of injection rate, stripping gas flow rate, nitrogen/methylene chloride ratio, drying column temperatures, and polymer concentrations have allowed us to make all the current ICF targets with a uniformity that is state-of-the-art for droplet tower technology.

Improvement of Wall Uniformity. The first step toward improving wall uniformity is to understand the shell-forming process within the SGDG system. We have begun statistical modeling of the system (see Simulation and Modeling, below). Informal experiments have begun to define the boundaries of the SGDG system.

One of the first discoveries was that we were not operating the SGDG as intended. In an ideal droplet generator, a fluid is passed through a needle. As the fluid exits the needle, a drop is formed. A stripping gas passing over the sides of the needle pulls individual drops from the needle. If the injection speed and stripping gas flow rate are

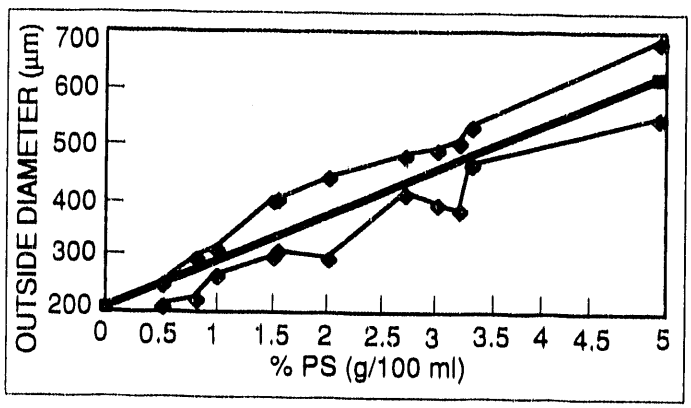

Fig. 1-26. Plot of PS capsule diameter as a function of solution concentration. The heavy straight line is a linear regression of average batch o. d. The data points are ± 2σ for the o. d. statistics of each batch, and form a 2σ "envelope" around the least squares line.

held constant, the drops formed should be uniform in size. With the parameters mentioned above, a variety of drop sizes were being formed. Between 80 and 90% of the drops were the same size, but quite a few were not because the injection rate was too high in relation to the stripping gas. Instead of pulling off individual drops, a stream was being produced that was being broken up into drops. To remedy this situation we slowed the injection rate to 1.00 µl/s.

Control is the key to this process. Over the next six months our goal is to increase control over all the parameters of the system, to define the shell-blowing process theoretically and experimentally, and to use this knowledge to improve wall uniformity. As part of that effort, we will evaluate ways to control bubble nucleation, the effects of aerodynamic drag, and the effects of various molecular weights and blends.

Coating (PVA). Polystyrene and PVA are the two components of the composite shells. Each complements the other to produce a fuel capsule whose total attributes exceed the sum of the individual component attributes.

The substrate is a PS shell. These shells are quickly and reliably produced in a variety of desired sizes. Polystyrene, being a poor containment barrier for any gas, is quickly and easily evacuated, then backfilled with a desired composition and mass of gas. The PVA, being a relatively good containment barrier, produces a "seal" surrounding the PS shell, essentially entrapping the desired gas. The net result is a strong, low-Z, shielded fuel capsule that exhibits good barrier properties.

The concept for fabricating PS/PVA composite fuel capsules has not changed much since the basic technology transfer to KMSF from Lawrence Livermore National Laboratory (LLNL) in 1988. However, since that time, there has been considerable refinement in the coating process, which has led to tremendous improvements in reliability and yield, and reduction in batch process time. These refinements are beginning to accelerate the experimental progress as well. Many refinements were based on theoretical process models used to simulate various aspects of the coating process. Other refinements were based on results from statistically designed experiments. The experimental and theoretical work through the first half of this reporting period resulted in a basic conclusion: If progress is to continue, especially in the area of coating quality and uniformity, a next-generation coating system must be engineered and constructed. Much of the work in the second half of this reporting period was directly related to the development of such a system.

For PVA coating research and production purposes, we have replaced our 15 cm diamter drying column with a drying column having a 0.6 m x 0.6 m square cross section. The average yield of coated shells with defect-free surfaces, as evaluated by optical inspection (defined as "good" coated shells), from the 15 cm diameter drying column system was approximately 2.5%. The average yield of good shells from the unmodified 0.6 m x 0.6 m drying column was approximately 17%. During the later part of 1989, the 0.6 m x 0.6 m drying column system was modified to improve control and reduce debris contamination of the coated shell surface. The modifications included, but were not limited to, installing an insulated, water-cooled top covering, a water-cooled collection surface, and PID temperature control. The result was a slight decrease in the average yield of good shells recovered to about 12%, with a range from 8% to 25%. This reduction in yield was more than offset by a reduction in set-up time and an improvement in coating quality. These improvements were a direct result of improved control and reduction of debris contamination, respectively.

Reduction in the yield of good shells is a result of an increase in natural downdraft (convection). In fact, initial results from the modified system were poor. The cooled covering increased the density of the air about the center of the drying column, thus significantly increasing natural downdraft. This resulted in a low yield of good product because the coatings were insufficiently dried. To compensate, the drying column temperature was increased to between 210 and 215°C. However, an obvious trade-off exists between changing temperature and the magnitude of the downdraft velocity. As the temperature was increased, so was the downdraft, and the result was a heat-damaged PS substrate. When we stopped cooling the covering, the result was an immediate improvement in the yield of good shells.

A statistical optimization approach was applied to improve the yield of good shells recovered. The statistical format was a near-saturated 2^3 factorial; the optimization approach is referred to as a "walk" or "self-directed optimization." This approach is an iterative method that uses the results of eight trials as boundary conditions to determine the next trial or set of trials. The control parameters considered were dry shear gas flow rate, solution injection rate, relative humidity of shear gas, capillary position relative to the nozzle exit, and two temperature zones. The results of the initial eight trials indicated that capillary position and the two temperature zones are the dominant control parameters within the original domain of the six varied. The control region of

optimum yield of good 435 to 455 μm coated shells is as follows:

Shear Gas Flow Rate (argon)	24 to 26 l/m on 605 ga.
Solution Injection rate	14 to 20 μl/s
Shear Gas Humidity (80°F)	54 to 62%
Capillary Position	(-)0.5 mm (inside nozzle)
Top Heater Zone	179 to 186°C
Bottom Heater Zone	181 to 189°C

Figure 1-27 illustrates the effectiveness of the optimization process employed. The best operating point was repeated, resulting in the average yield stated previously.

The spectrum of results from the modified drying column system is very similar to the results prior to modification. In the vicinity of optimum yield of good shells recovered, approximately one-third of the product was not dry before colliding with the collection dishes, one-third was heat-damaged, and one-third was good. The resulting spectrum of product is illustrated in Fig. 1-28. Since the humidity of the shear gas is now under some control, there is virtually no clumping together of coated shells. Before humidity control, clumping was the dominant problem. Clumping appears to be caused by high shear gas humidity.

The variation in the characteristics of recovered product is a result of the drying column being too short. The temperature required to dry the PVA coating on a 435 to 455 μm shell is much higher than the glass transition temperature of the PS. The PS substrate is protected while the PVA is still in solution about the shell. Heat of vaporization of the solvent (water) keeps the substrate temperature below its glass transition temperature. However, when the PVA phases out of solution, the substrate temperature increases rapidly (see Simulation and Modeling, below, for details). If the temperature of the substrate is kept high enough long enough, heat-damaged product occurs. On the other hand, if some shells fall through a slightly cooler region they will not be completely dry before they reach the bottom of the drying column. The good shells are those that fall through a region that dries them sufficiently without heat

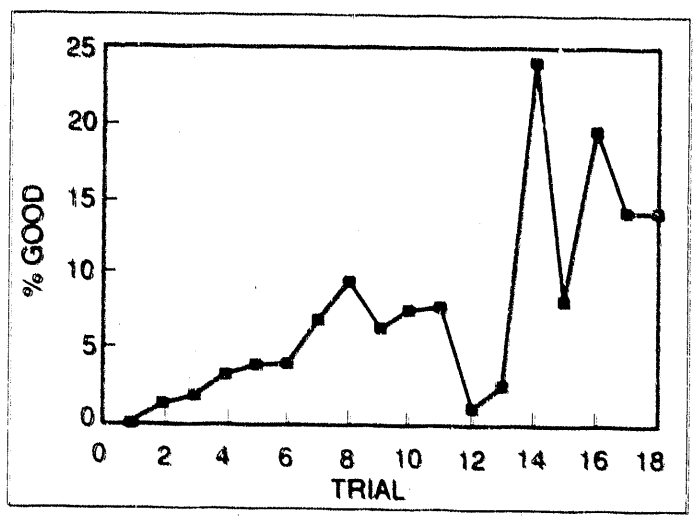

Fig. 1-27. Progression of the optimization process. The percentage of good shells recovered is plotted as a function of progressing trials.

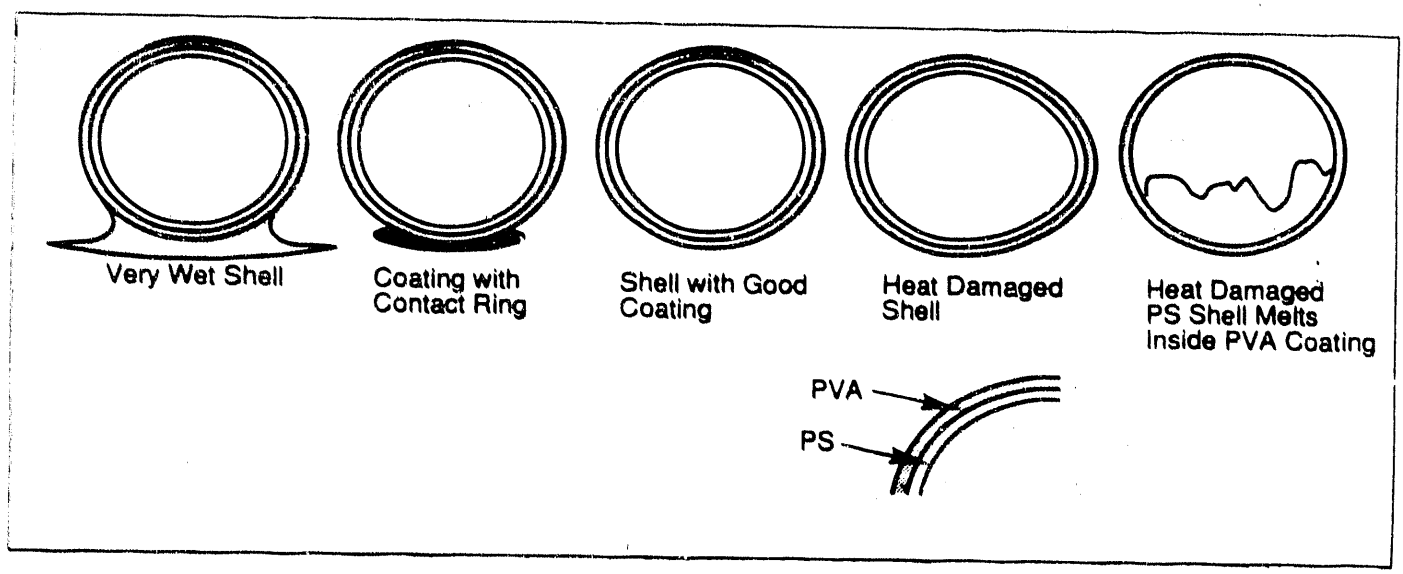

Fig. 1-28. The spectrum of product recovered after a run.

damage of the substrate. Unfortunately, drying shells at relatively high temperatures is a very unstable process. Figure 1-29 illustrates drying instability.

The conclusion from experimental results, which are supported by theory, is that the 435 to 455 μm diameter x 3 μm thick shells are about the size limit for the drying column. However, for any set drying column length, theory suggests that reducing the outside diameter sufficiently should improve the yield of good shells. Theory predicts that the temperature at which the coatings should dry would be lower, thus the stability of the process should improve. Improved stability implies that the ratio of heat-damaged shells to either wet or good recovered shells should drop. Raising the temperature slightly to decrease the ratio of wet shells to good shells without producing heat-damaged shells should also be possible. Assuming that the total number of shells recovered has not changed, there should be a tremendous improvement in the yield of good shells recovered.

The hypothesis that the yield of good shells would improve by decreasing the size of the shell and lowering the drying column temperature was tested by producing PVA coated shells for the Laboratory for Laser Energetics (LLE) at the University of Rochester. The hypothesis was directly supported by coating 220 to 245 μm shells in the drying ccolumn. Once the injection parameters were determined, the yield of good shells approached 50%! The observed yields reflect a recovery of 60 to 120 shells with a good coating produced from the injection of one capillary tube full of solution and shells. These shells were dried between 100 and 115°C, as predicted by theory. Figure 1-30 illustrates the difference between drying 445 μm shells and 230 μm shells. Additional information is presented in Simulation and Modeling, below.

Unlike surface finish, the uniformity of the PVA coating is not now a controllable attribute. The nonuniformity of the coating ranges from 50 to 100%. Nonuniformity of the PVA coating, at the present, is not of much concern to Lawrence Livermore National Laboratory (LLNL) since the bulk uniformity of the final trilaminate target is essentially unaffected. The Laboratory for Laser Energetics, on the other hand, has some concerns about the PVA coating uniformity. It was decided that constructing a new PVA coating system, engineered to meet current and anticipated future research and production requirements, would be in the best interest of the ICF program. The current coating system is not versatile enough to be an adequate research tool.

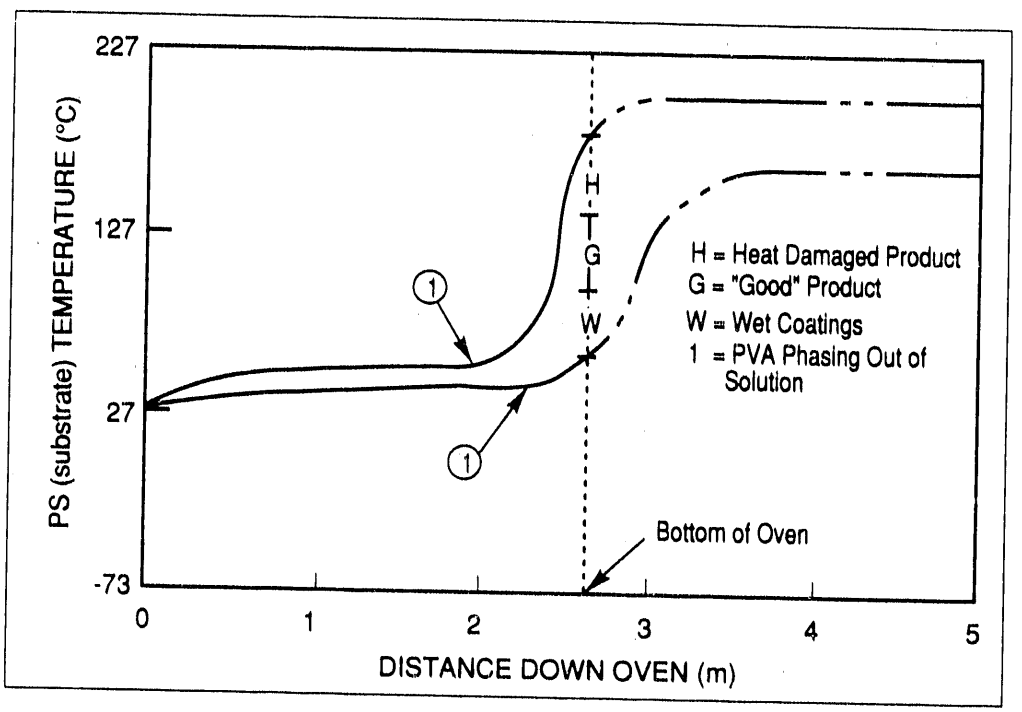

Fig. 1-29. Variation of substrate temperature with drying distance.

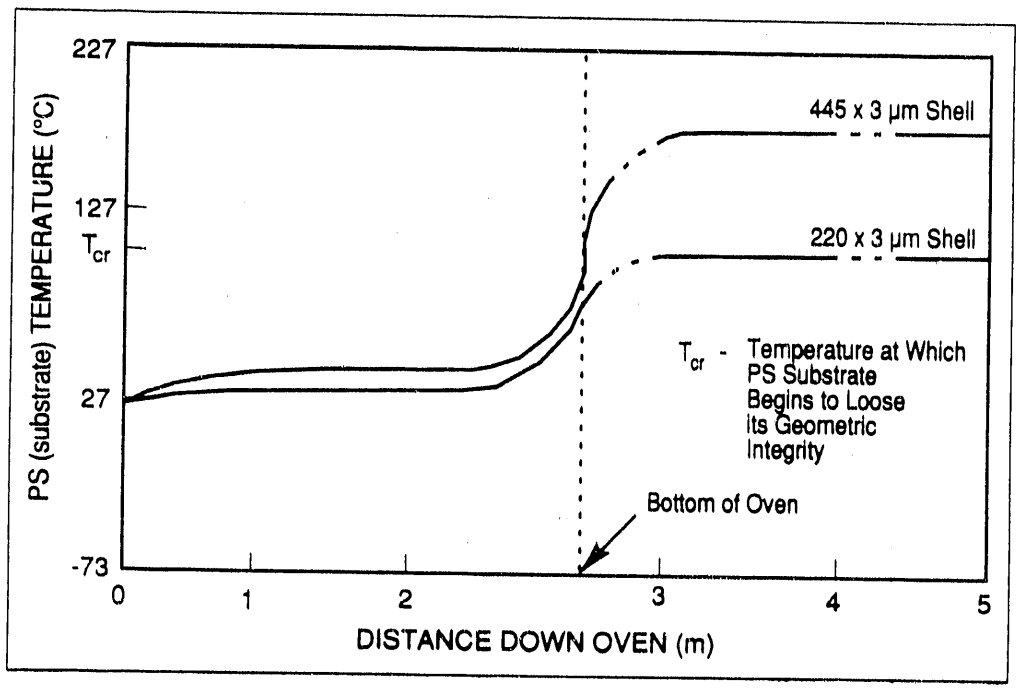

Fig. 1-30. Substrate temperature is plotted as a function of drying distance for shells of two different diameters.

Theory suggests that uniformity will be affected by altering the pressure and composition of the heated gas in a drying column (for additional information see Simulation and Modeling, below). The current system is incapable of supporting the type of experiments that will be required to study coating uniformity. The current system is limited to additive and surface treatment studies, which are currently underway.

For the new PVA coating system to meet our requirements, it must be able to dry the liquid PVA layer surrounding a PS shell at temperatures that will not not damage the PS substrate. This implies that the drying temperature must not exceed the glass transition temperature of the substrate. It also implies that the drying column necessary to accomplish this must be taller than the existing system. The new system must be suitable for research as well. This implies that the control parameters of the system must be adjustable over broad ranges and have good resolution. It also implies that the environment within the drying column should be controllable in composition, pressure, and temperature. The system must also allow for easy acquisition of data - preferably automatic or semi-automatic acquisition. Therefore, these and many other topics are being considered to ensure a successful design.

Specifically, the system under development is being designed to coat 700 μm x 10 μm PS shells with 4 μm of PVA. The PVA is from a 10%, 25,000 average m.w. PVA solution that is 98.5% hydrolized. The process conditions are similar (except for residence time) to those currently being used to apply 3 μm PVA coatings to 445 μm x 3 μm PS shells. In addition, the system is being designed to coat shells of the size of current interest to LLNL at temperatures of less than 100°C in 1.0 atm of air. The system will be expandable to increase the upper limit of diameters and/or wall thicknesses of shells that could be coated. The system is also being designed to accurately control the temperature over a 30 to 200°C range and the pressure over a 1 to 1500 Torr range, and to provide control of the gas composition. Sizing the system was accomplished through computer simulation of the process (see also Simulation and Modeling, below).

A system as versatile as the one being developed will be much more sophisticated and complex in design than the present system. The first phase of this project includes, but is not limited to, completing the design and construction of a coating system that meets the requirements delineated above. It is anticipated that the first phase of this project will be completed in June 1990, at which time experimental work can begin on the new system.

The specification for this system addresses every aspect of the coating process. To develop the specification, the coating process was broken down into subsystems, which were categorized by isolated, integrated, or related subsystems or subprocesses. There are twelve basic subsystems or subprocesses; six are being addressed in the first phase of the project. Approximately 95% of the control system and 75% of the mechanical system is specified, and all critical engineering calculations are complete. The project currently is on schedule and the June completion date has not changed. Figure 1-31 is a simplified schematic of the new PVA coating system.

For additional information, please contact Lorne Adams

Microencapsulation. The water in oil in water (W/O/W) microencapsulation process involves three distinct phases: (1) an internal water phase, (2) an oil phase, and (3) an external water phase. The internal water phase is suspended in the oil phase, which is in turn suspended in the external water phase. The internal phase consists of distilled water with no additives. The oil phase consists of PS dissolved in an appropriate solvent system (the preferred solvent system contains 50% benzene and 50% 1,2 dichloroethane by volume). The external water phase contains 5% PVA.

The internal water phase is dispersed in the oil phase as discrete droplets. The polymer solution is dispersed in the external water phase as individual drops, each of which contains one of the water droplets. Surface tension and interfacial tension tend to make the polymer drops spherical and to make the internal water droplets spherical and concentric with the oil phase.

The solvents in the oil phase dissolve in the external water phase, diffuse to the surface of the water, and evaporate. The solidified shells thus produced are separated from the external water/PVA phase by a water rinse, which removes PVA from the shell surface. The shells are then placed in alcohol to start the removal of the internal water phase and also to reduce residual solvents. The shells are then placed in a vacuum oven, which removes the remaining internal water phase from inside the shells and residual solvents from the shell walls.

Vacuoles (bubbles in the shell walls) can originate from several sources, including entrainment of air, entrainment of internal-phase water, entrainment of external-phase water, and water dissolved in the oil phase. Dispersion techniques are used to

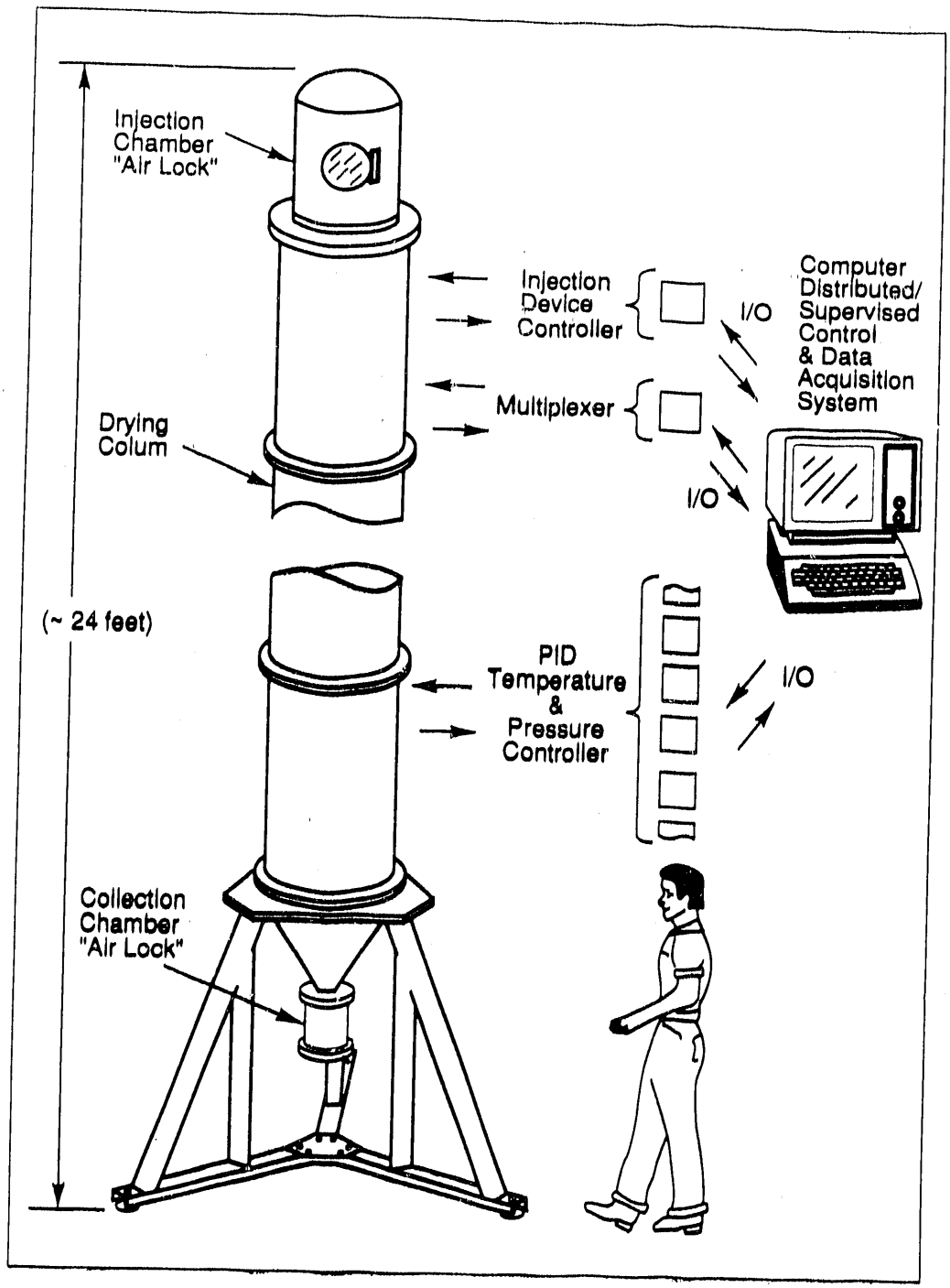

Fig. 1-31. Basic configuration of the new PVA coating system.

minimize (if not eliminate) entrainment of both air and water in the oil phase during the dispersion of the internal phase and the dispersion of the oil phase.

The most likely source of vacuole formation during microencapsulation is water dissolved in the oil phase. Water is soluble at a level of about 0.1% at 25°C and > 5% at 70°C (benzene azeotrope contains 9% water at 69°C and 1,2 DCE azeotrope contains 8% water at 72°C). Water droplets can be formed in a 1/1 benzene/1,2 DCE solution by placing the solution in a vial with water, raising the temperature to 70°C, then cooling the vial to room temperature. Heating saturates the solvent with water. Cooling forces the water out of solution into droplets that are large enough to scatter light but small enough to form a very stable dispersion.

The dispersion method that has been used by the Institute for Laser Engineering at Osaka University and LLE is to place the internal water phase and the polymer solution into a vial and shake it for 10 s. The ILE process calls for 5 g water and 10 g polymer solution in a 200 ml vial,[27] while LLE's process calls for 4 g of water and 8 g of polymer solution in a 15 ml vial.[28] We made shells using both a 200 ml and a 15 ml vial. The shells made using a 15 ml vial contained far fewer vacuoles than did those made with the 200 ml vial.

The polymer solution is dispersed into the external water phase using a four-bladed, propeller-type stirrer. Initally, 400 rpm is used to disperse the polymer solution into droplets, then 200 rpm is used to keep the droplets in suspension.

The internal water phase, the polymer phase, and the external water phase are filtered to remove nonvolatile particulate contaminants. We filter the internal water phase to 0.1 μm, the polymer phase to 0.1 μm, and the external water phase to 0.22 μm.

Filtration of the internal water phase removes particulate material that would otherwise remain inside the finished shell. This particulate material could also be incorporated into the shell wall. This filtration to 0.1 μm is accomplished using a syringe-mounted filter.

Filtration of the polymer solution removes particulates that could contaminate the shell wall. This contamination is undesirable for two reasons: (1) the contaminant itself is undesirable in the shell wall and (2) the contaminant can act as a nucleation site for the formation of a vacuole in the shell wall. The polymer solution is filtered to 0.1 μm using a syringe filter.

Filtration of the external water phase/PVA solution removes particulates that can contaminate the exterior surface of the shells. The water/PVA solution is passed through

a 0.22 µm filter using a vacuum system to force the solution through. The vacuum degasses the solution in addition to removing the particulates.

The polymers used in the microencapsulation process are selected on the basis of the physical and chemical property requirements of the shells. The solvents are selected on the basis of their compatibility with each other and with the polymers used to make the shells.

The ideal internal-phase material would be insoluble in the polymer solution and capable of diffusing through the shell wall after the shell has solidified. Water meets these requirements reasonably well, even though it is slightly soluble in the polymer solution. The density of the internal phase should be close enough to the density of the polymer solution to neutralize gravity so that surface tension and interfacial tension can center the internal phase in the polymer solution drop.

The ideal polymer-phase solvent must be a good solvent for the polymer. It should also be slightly soluble in the external-phase solvent so that it will dissolve in the external phase for transport out of the shell wall. It is desirable for syneresis to occur betweeen the solvents and water such that the water leaves the shell along with the solvents. Syneresis would prevent the formation of vacuoles because phase separation wouldn't occur. The density of the polymer solution must be close enough to the density of the external phase to neutralize gravity and allow the surface tension of the polymer solution to force the drop to be spherical. The surface tension of the polymer-phase solution should be lower than the surface tension of the internal phase. A 50% by volume blend of benzene and 1,2 dichloroethane meets these requirements well. This blend of solvents forms shells having the best sphericity and wall uniformity.

The external phase should be insoluble in the polymer-phase solution and have a surface tension lower than the polymer solution. A 5% PVA in water solution has properties close to the ideal external phase. The problem is that water is slightly soluble in the polymer solution, and this solubility is what leads to the formation of vacuoles.

Process temperatures at different stages of the microencapsulation process are important because they affect the solubility of the various components in each other.

The internal phase is dispersed in the polymer phase at room temperature. The polymer solution is dispersed in the external phase at 65°C. The temperature is raised to 85°C to remove the solvents from the polymer phase. It is important that the temperature be constant or increasing until the shell walls have solidified. The dissolved water will separate because of solubility changes with temperature if the temperature is lowered before the shells have solidified.

Shells have been produced using PS with m.w. of 22k, 50k, 90k, 165k, 200k, 400k, 900k, and 1,500k. The following trends were observed with increasing m.w.:

1. Total yield tends to decrease.
2. Shell diameter tends to decrease.
3. Wall thickness increases.
4. Resistance to fracture increases.

The maximum yield of shells for a given set of conditions consistently occurs with 90k m.w. polymer. The microencapsulation process is currently used to produce "Class A" PS shells ranging from about 200 to 1000 μm in diameter with uniform walls ranging from about 3 to 12 μm.

Solvents and additives that can affect solubility will be investigated on the basis of their compatibility with all of the components in the system. Components will be selected on the basis of their ability to cause syneresis to prevent vacuole formation.

We will investigate two different dispersion methods. The method currently being investigated is to suspend the internal water phase in the oil phase by shaking the two phases together in a vial and then dispersing that mixture into the external water phase with a stirrer. We will continue to evaluate this method. The second method is to use a hollow droplet generator to introduce uniform-size droplets with uniform walls.

Care must be taken to minimize turbulence at the interfaces as the phases are being dispersed in each other. The design will incorporate smooth flow channels to reduce turbulence. The Reynolds number will be kept low to operate in laminar flow conditions.

We currently control the temperature during the solvent removal, rinsing, washing, and drying steps of the process. Temperature is controlled independently for each step. Temperature varies from step to step as well as during the transfer between steps. We will investigate the use of an isothermal process, maintaining a constant temperature during the entire process. The shells will be totally contained in the process equipment,

at a constant temperature, from the point where the different phases come in contact with each other until the water is totally removed from the shells.

Size control will be determined by investigating the effect of mixing and stirring intensity in the hand-mixing method, and by orifice sizes, injection rates, and orifice vibration in the hollow droplet generator method.

Wall thickness control will be evaluated by investigating the effect of polymer concentration in the oil phase in both methods and by orifice size, injection rate, and orifice vibration in the hollow droplet generator method.

We will investigate two methods to form a PVA layer on the PS shell: (1) use of a four-phase emulsion (water in oil in water in oil) and (2) dispersion of water-filled PS shells in a PVA solution, followed by dispersion of that solution in oil and removal of water from the PVA and from inside the shell to leave a uniform PVA-coated shell.

The results of recent microencapsulation experiments are summarized in Table 1-4.

Simulation and Modeling The PS shell formation process consists of several steps: injection, drying, nucleation, and blowing (see Fig. 1-32). The PVA coating process shares the first two of these steps, so a single model can be constructed to apply to either case. This report first considers drying in the context of PVA coating, then considers blowing of PS shells, keeping in mind that the PS must dry before blowing according to the same mechanism as the PVA.

Experimentally, the most effort so far has been concentrated on the injection, i.e., controlling the rate and drop monodispersity through injection system design. This has been sufficiently successful that the injection is giving predictable, consistent drop streams. Consequently, the injection step is probably not important in modeling the process - the drop stream may be taken as given at the top of the tower. The efforts in modeling described below concentrate on what is occurring after the injection. The largest effort so far has been given to the drying step.

Numerical Model of Drying. The model to be developed here gives the depletion of mass of solvent from the PVA solution as the shell falls down the tower. The outside

Table 1-4. Diameters and wall thicknesses of PS capsules from recent microencapsulation experiments, where polymer m.w. and solution concentration were varied.

Run #	Mean Dia (μm)	Mean Wall (μm)	Min. Dia. (μm)	Min. Wall (μm)	Max. Dia. (μm)	Max. Wall (μm)	M. W (10^3)	Conc. (%)
ME010290-1	564	6.5	310	2.3	738	9.5	250	5
ME010390-1	500	5.4	247	1.1	729	10.4	250	5
ME010490-1	512	5.8	268	1.3	818	14.2	250	5
ME010590-1	647	5.8	470	3.6	1024	8.9	250	5
ME011190-1	387	5.7	177	3.3	602	10.0	200	5
ME011290-1	399	3.8	188	1.9	676	6.0	50	5
ME011590-1	440	5.4	202	2.8	728	8.7	170	5
ME011790-1	513	5.8	209	3.4	900	7.9	900	2.5
ME012390-1	430	5.4	206	3.2	838	6.6	900	3
ME012490-1	550	7.4	189	3.7	901	10.0	170	5
ME020690-1	619	9.1	358	3.9	948	11.1	170	5
ME021090-1	490	8.5	212	5.5	746	12.1	200	5
ME021590-1	442	5.6	114	2.9	787	12.3	250	3.6
ME021690-1	581	6.2	100	3.8	823	10.0	250	3.6
ME022090-1	559	5.6	123	2.7	802	9.7	250	3.6
ME022290-1	391	5.0	205	3.0	578	7.2	250	3.6
ME022790-1	559	6.5	191	4.9	769	9.5	250	3.6
ME022890-1	405	5.4	160	3.4	650	7.7	250	3.6
ME030190-1	452	5.3	216	3.9	706	9.5	250	3.0
ME030190-2	391	5.4	231	3.6	587	8.9	250	3.0
ME030690-1	340	8.1	234	3.3	454	12.6	900	2.5
ME030790-1	630	8.5	284	4.4	908	11.8	170	5
ME030890-1	509	4.9	220	3.3	940	7.7	90	4.5
AVERAGE	492	6.1	222	3.3	767	9.7		

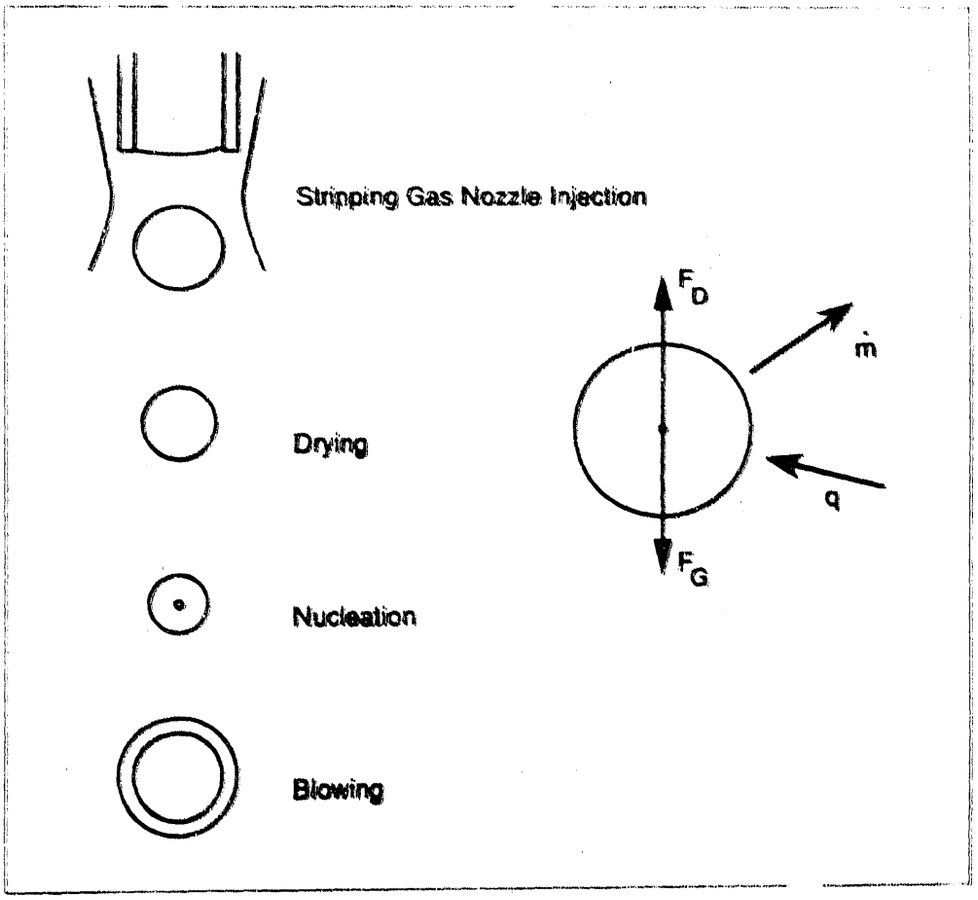

Fig. 1-32. Schematic representation of the PS shell-forming process. A stripping gas pulls droplets of PS solution from a capillary tube. The droplets fall through a vertical tube furnace, where the drying, nucleation, and blowing steps take place. The forces acting on the drop are aerodynamic drag F_D and gravity F_G. Thermal energy q drives solvent evaporation $\dot{m}$.

diameter d of the coating is

$$d = \left[\frac{6m}{\pi\rho} + d_H^3\right]^{1/3},$$

$$\frac{1}{\rho} = \sum_i \frac{\bar{\omega}_i}{\rho_i},$$

where m is the remaining mass of solution and ρ is its density, which is estimated by assuming that the solution constituents are additive in volume.

At the end of the run, the only mass remaining is the PVA (subscript P) that was present initially ($\bar{\omega}_i$ denotes mass fraction, so far assumed to be homogeneous throughout the coating, and m_f is final mass),

$$m_f = \bar{\omega}_P^o m_o .$$

The drying process is a balance of heat, mass, and momentum transport processes. Heat transfer θ to the drop drives evaporation of the solvents present, so that there is a mass transfer $\dot{m}$ from the drop. Simultaneously, the atmosphere exerts a fluid drag force F_D on the droplet. These effects for the transport outside the drop may be modeled on an average or macroscopic basis using readily available correlations in chemical engineering. Previous work at KMSF[29] began in this direction for drying of PVA shells from a hollow droplet generator.

The evolution of the droplet (its position, velocity, mass, composition, size, and temperature) may be modeled using a system of ordinary differential equations for these bulk properties of the droplet. Following are the equations derived from descriptions of the three types of transport:

$$\dot{z} = v_z,$$

$$\dot{v}_z = -\frac{\pi Re C_D \mu_A d(v_z - v_z^\infty)}{8(m+m_H+m_G)} - \frac{\pi\rho_A g d^3}{6(m+m_H+m_G)} - \frac{\dot{m}_{out} v_z}{m+m_H+m_G} + g,$$

$$\dot{T} = \frac{-\pi Nu k_A d(T-T_\infty) + \sum_i \dot{m}_i \lambda_i}{(m+m_H+m_G)\,c}$$

and

$$\dot{m}_i^{out} = -\pi \frac{M_i}{M_A} Nu_{Ai}\,\theta_i\,\rho_A\,D_{Ai}\,d\,\frac{x_i^{out} - x_i^{\infty}}{1 - x_i^{out}}$$

Notice the similar form of the terms for transport to or from the environment, ∞. Primary variables in the above equations are downward velocity v_z, position down the tower z, temperature T, and masses of coating m, PS shell m_H, and interior gas bubble m_G. Properties of the atmosphere A are evaluated at the film temperature and tower pressure: density ρ_A, viscosity μ_A, molecular weight M_A, thermal conductivity k_A, and diffusivity of i in A, D_{Ai}. These may variously be estimated from the ideal gas law, from Lennard-Jones kinetic theory,[30] or from tabulated data. Subscript i refers to the species present in the drying solution. The specific heats of vaporization λ_i of the volatile species are needed, as well as the specific heat capacity of the mixture c. Analogous dimensionless numbers appear in the three transport equations: ReC_D, the Reynolds number multiplied by the drag coefficient; Nu, the Nusselt number for heat transfer to a sphere; and $Nu_{Ai}\theta_i$, the mass transfer Nusselt number multiplied by a correction factor[31] for high transfer rates. The drag coefficient is correlated as a function of Reynolds number by Clift et al.,[32] and the two Nusselt numbers are commonly calculated by the Ranz-Marshall equation as functions of Reynolds number and Schmidt or Prandtl number.[33] The mole fraction of each volatile species at the shell surface x_i^{OUT} is calculated from vapor/liquid equilibrium (VLE) data. Simple VLE activity coefficient models are the Wilson equation[34] for dilute solutions and Flory-Huggins theory for concentrated polymer solutions.[35] The conditions far away from the drop are influenced by the shear gas jet at the top of the tower. They may be estimated from theory for the velocity of a turbulent gas jet[36] and from experimental conditions in the tower. As a final note, two similar equations (except for gravity g) can be

constructed for horizontal displacement x and horizontal velocity v_x if the droplet starts out at some angle from vertical.

It has been suggested that fluid drag and gravitational effects contribute to shell or coating nonuniformity. For PS blowing, the system is far too small for internal buoyancy to have any relevance, and the shell viscosity is so high in comparison with the atmosphere that it is unlikely that drag is causing the nonuniformity after the blowing step. Most likely, the nonuniformity is caused by off-center nucleation or by asymmetric fluid properties due to asymmetric drying. For PVA coating, fluid drag must be the culprit, pushing fluid around to the back of the shell as it falls. The bottom of the droplet will dry several times faster than the top under typical conditions. Asymmetries around the droplet or shell in the momentum and mass transfer increase with Reynolds number,[32]

$$Re = \frac{\rho_A [v_z - v_z^\infty] d}{\mu_A}.$$

The next section explores some efforts to reduce the Reynolds number as part of the design and planning for the new PVA coating tower.

Results for PVA Drying. As a guide for the design of the new PVA coating tower, the computer model was run for a variety of expected or possible conditions. Shells currently produced for LLNL are typically 450 x 3 μm PS, coated with 2.5 μm PVA. Ideally they would be coated with PVA at a temperature only moderately above the PS glass transition temperature of about 80°C. Figure 1-33 shows the effect of pressure on production of shells this size at 100°C.

As expected, drying takes longer at lower pressures because of a moderately higher shell velocity. This is not due to a lowering of the viscosity, which is essentially independent of pressure for gases at low pressure. Nor is it due to a lowering of the total drag force, which exactly balances gravity and is therefore the same except to the extent that it takes longer to accelerate to terminal velocity. Rather, it is because of the reduced density of the nitrogen atmosphere. In fact, as illustrated, the density decrease with vacuum overwhelms the velocity increase to reduce the Reynolds number and provides some hope that vacuum conditions will improve uniformity. If drag force is important in nonuniformity, then reduced pressure will have no influence on

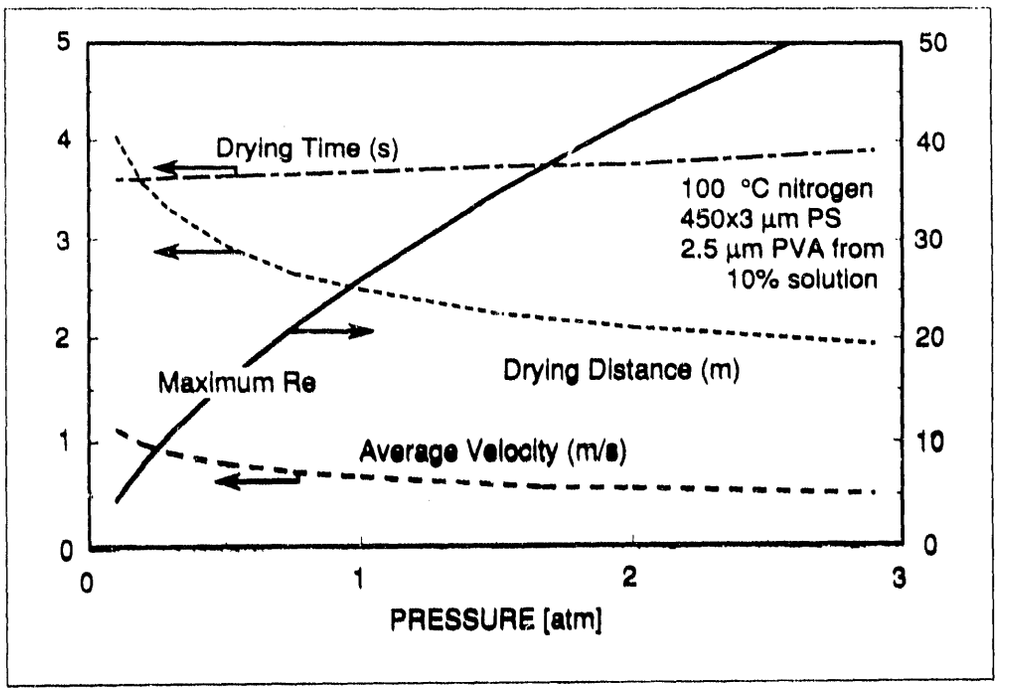

Fig. 1-33. Results from simulated production of 450 µm PVA/PS composite capsules. The time and distance required to dry the PVA layer, capsule velocity, and maximum Reynolds number are plotted as functions of nitrogen pressure inside the drying column.

uniformity, but the reduced Reynolds number at reduced pressure will mean more uniform mass transfer and presumably more uniform drying.

Similar calculations can be done as a function of temperature for a particular pressure, as depicted in Fig. 1-34. The first conclusion is that doubling the drying distance from the currently available 2.5 m or so will allow much lower temperatures. Since current temperatures are around 180 to190°C, it is also seen that the modeling underpredicts drying distance, so that some design factor is needed from the calculations in their current form. Interestingly, the shell velocity is roughly insensitive to temperature, so Reynolds number decreases slightly with temperature since density is again decreasing.

To provide some size guidelines for the new PVA tower, runs were done to determine the temperature needed to dry shells of representative size in the proposed 16 ft column with a 25% safety factor in length (i.e., the model-predicted distance equals 12 ft). Table 1-5 considers the operating range in atmospheric air, high pressure air, and the intriguing (though expensive) option of helium.

Table 1-5. Temperatures needed to dry representative or extreme size shells in 12 ft under various atmospheres. Also: maximum Reynolds number seen and maximum distance from center line for a 25° initial trajectory.

Ambience	Pressure (atm)	PS o.d. (μm)	PS Wall (μm)	PVA Coat (μm)	T needed to dry in 12 ft. (°C)	Max Re	Max x
Air	1	200	3	3	32	50	6.5
Air	1	500	3	3	97	91	12.4
Air	1	700	3	3	134	112	15.1
Air	1	500	10	4	146	83	16.5
Air	1	700	10	4	187	102	20.3
Air	2	700	3	3	112	237	11.3
Air	2	500	10	4	122	177	12.4
Air	2	700	10	4	162	216	15.2
Helium	1	700	3	3	92	16	29.5
Helium	1	500	10	4	96	12	31.3
Helium	1	700	10	4	133	15	39.6

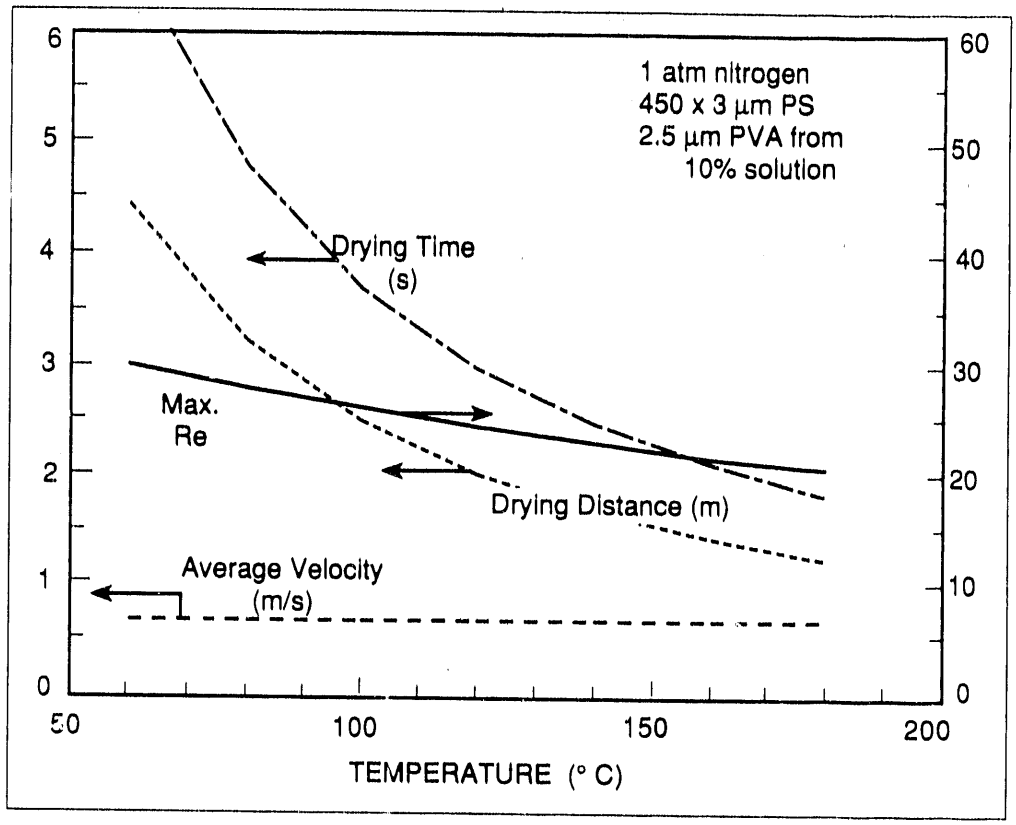

Fig. 1-34. Results from simulated production of 450 μm PVA/PS composite capsules. The time and distance required to dry the PVA layer, capsule velocity, and maximum Reynolds number are plotted as functions of temperature inside the drying column.

From this table, we can conclude that current-size shells can be coated easily in the planned new tower. Coating larger, microencapsulation shells should also be feasible (if barely), if temperatures as high as currently used (180°C) can be tolerated. The table also shows that shells injected at the observed maximum angle of about 25° from vertical will not strike the wall in a 2 ft diameter (30 cm radius) furnace, with the possible exception of runs in a lower-density helium atmosphere. Not shown are results for a higher-density argon atmosphere, which makes things worse all around compared to air or nitrogen.

In general, the column size required is almost directly proportional to shell size for a given wall thickness. Because of curvature (the initial solution thickness is about ten times the final coating thickness), drying distance is more than proportional to the PVA thickness to be dried. In looking at the possibilities for vacuum, a question arises concerning the largest shell that can be dried for a given pressure at a moderate temperature. Table 1-6 answers this question for air at 110°C.

Table 1-6. Largest shells that can be dried at 110°C and various air pressures. PS Wall = 3 μm; PVA = 3 μm.

P (atm)	Maximum PS o.d. Dried in 12 ft (μm)
0.1	385
0.5	490
1.0	570
1.5	632
2.0	685

The drying model predicts drying times shorter than those observed in current experiments with the spray box. Several experimental factors may contribute to this discrepancy: (1) the shear gas jet apparently induces or exacerbates sizable convection currents, resulting in an uneven temperature field, (2) still lacking on the modeling side is adequate treatment of the mass transfer going on inside the coating; the coating is treated as a homogeneous liquid at all points in time, and (3) skinning over of the polymer on the surface would resist diffusion of the solvent to the surface and would lower the vapor pressure at the surface. Modeling of this problem via finite difference

solution of the diffusion equations involved is well underway and should lead to longer predicted drying times or distances and better understanding of the process.

Blowing: Numerical Model. For PS shell formation, in addition to the drying processes already described, there is the added step of inflating the droplet of solution into a hollow sphere. This step can be modeled as an addition to the set of ordinary differential equations to be numerically integrated. Past work at KMSF considered the fluid mechanics of a falling hollow droplet,[37] and Amundson et al.[38] considered the final inflation and refinement of a polymer shell. In this work we sought a simple model valid from the beginning of the blowing stage.

The size of a droplet or blowing shell can be calculated from its mass in a manner similar to that used for the PVA coating if the inner gas bubble diameter d_G is known,

$$d = \left[\frac{6\ m}{\pi\ \rho} + d_G{}^3\right]^{1/3} .$$

This formula also applies for a droplet if $d_G = 0$. The wall thickness of the shell, $w = (d-d_G)/2$, can be calculated also. Calculations can easily be done that relate the final PS shell dimensions to the initial droplet size or vice versa. Again, the simple volume-additive mixing rule applies for density. The unknown gas bubble diameter remains to be determined from the fluid mechanics of the bubble inflation.

Once blowing begins, the heat transfer to the shell drives evaporation of solvent and blowing agent both to the outside and to the inside gas bubble G. Since blowing occurs quite rapidly, we neglect the outer evaporation at this point to simplify things,

$$\bar{\omega}_i\ \pi\ Nu\ k_A\ d\ (T-T_\infty) \approx \dot{m}_i^{in}\ \lambda_i ,$$

$$\dot{m}_i^{G} = -\dot{m}_i^{in} .$$

The model considers the inflation to begin with nucleation at the center of the droplet and to proceed spherically symmetrically. The spherically symmetric velocity profile that satisfies continuity and the boundary conditions on the inner and outer surfaces of the

shell is

$$u_r = \frac{d_G^2 \dot{d}_G}{8 r^2},$$

$$u_\theta = u_\phi = 0,$$

where u is relative to the center of mass of the shell. This is a biaxial extensional flow with extension rate $\dot{e}(r)$,

$$\frac{\partial u_r}{\partial r} = -\frac{d_G^2 \dot{d}_G}{4 r^3} = \dot{\varepsilon}.$$

The next step is to put this velocity profile into a constitutive model for the stress. Since the elongational viscosity of PS and other polymers is roughly independent of extension rate, the particular constitutive model used does not matter, only the value of the elongational viscosity $\bar{\eta}$ which is three times the value of the zero shear rate shear viscosity η. Following are equations for the stress in the bubble,

$$\tau_{\phi\phi} = \tau_{\theta\theta} = \frac{2\eta u_r}{r} = -\frac{1}{3}\bar{\eta}\frac{\partial u_r}{\partial r} = \frac{\bar{\eta} d_G^2 \dot{d}_G}{12 r^3}$$

and

$$\tau_{rr} = 2\eta\frac{\partial u_r}{\partial r} = \frac{2}{3}\bar{\eta}\frac{\partial u_r}{\partial r} = -\frac{\bar{\eta} d_G^2 \dot{d}_G}{6 r^3}.$$

The elongational viscosity is dependent on PS concentration, PS molecular weight, and temperature. These dependencies may be described by, for example, the Martin equation and the WLF equation.[39]

When the above equations for stress are substituted into the Cauchy equation of fluid motion (with the assumption of creeping flow), and the equation is integrated from the inner to outer surface with surface tension boundary conditions on each, the result is a

differential equation for d_G as a function of the pressures in the bubble P_G and in the tower P_A,

$$\dot{d}_G = \frac{P_A - P_G + 4\gamma\left[\frac{1}{d} + \frac{1}{d_G}\right]}{\frac{4\bar{\eta}\, d_G^2}{9}\left[\frac{1}{d^3} - \frac{1}{d_G^3}\right]}$$

This equation comes into play after nucleation occurs. In reality, nucleation will occur when the interior solvent vapor pressure exceeds the containing force of surface tension, depending on the presence of impurities or nucleating agents. The numerical model currently uses a very simple description: Nucleation occurs at some specified degree of dryness to match the final shell dimensions observed.

Results for PS Blowing. Figure 1-35 presents results of a run for the typical production of 450 μm PS capsules. Shown are the evolution of shell temperature, mass and composition, and velocity down the tower. General results are that the droplet stays quite cool (room temperature) during the drying. It initially accelerates and then decelerates as it shrinks. The blowing step occurs very rapidly according to the model. This agrees with the observation that partially inflated shells are rarely observed experimentally. Once it has blown and dried, the shell acts like a parachute: it slows down considerably and heats up to the air temperature. Model results are fairly insensitive to initial conditions. As for PVA coating, PS drying and blowing times predicted so far have been less than are apparently occurring in experiments. Again, current work in modeling the internal diffusion of the polymer and solvents will add more detail to the picture.

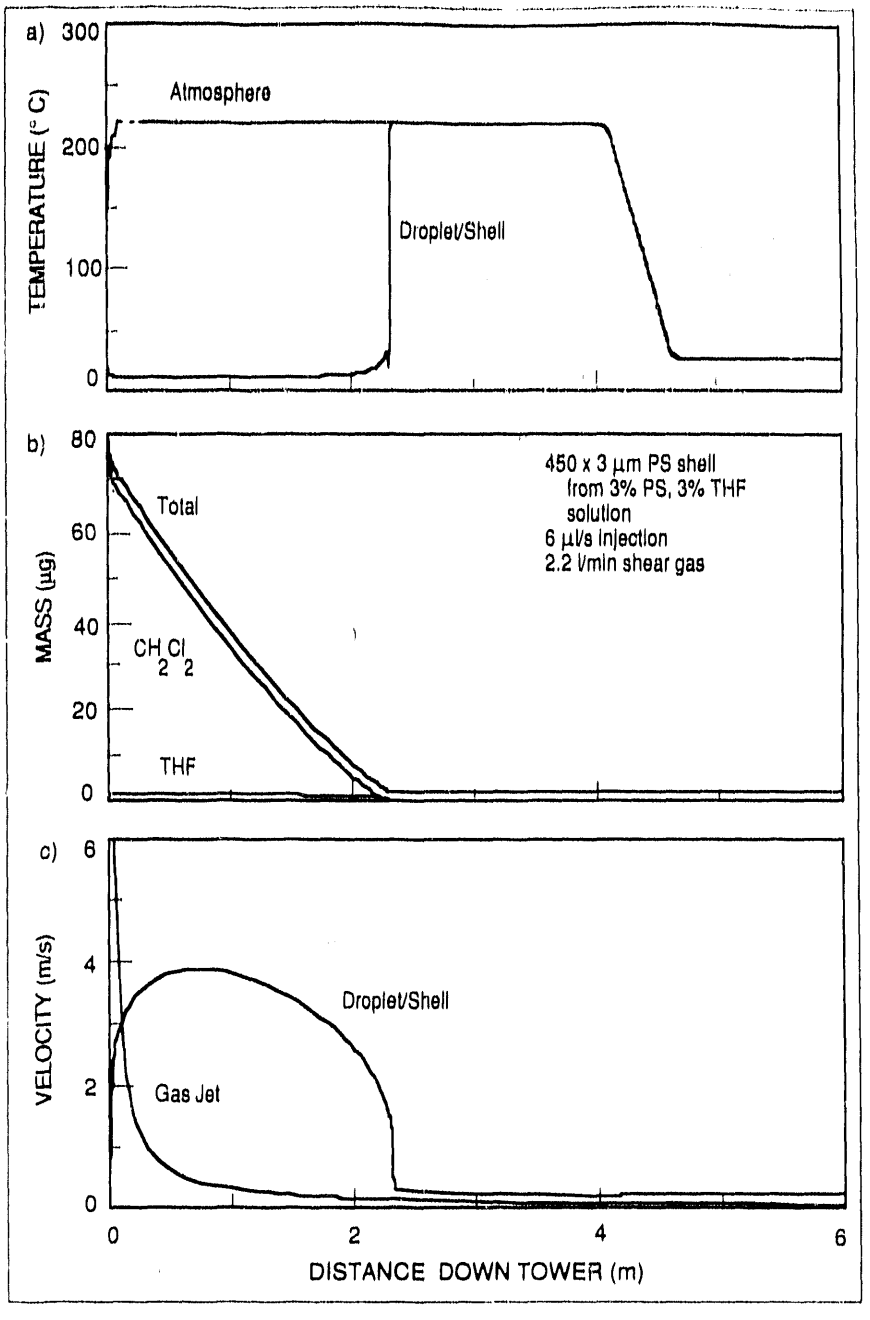

Fig.1-35. Results from simulated run for production of 450 µm PS capsules. Figure 1-35a shows the evolution of shell temperature as the shell proceeds down the column, Fig. 1-35b shows the change in mass and composition, and Fig. 1-35c shows velocity as a function of position down the column.

For additional information, please contact Thomas P. O'Holleran

1.3.2 Advanced Fuel Container Fabrication

Introduction

For the past several years, we have been developing techniques to fabricate high-aspect-ratio fuel capsules with diameters ranging from 2 to 10 mm to meet the needs of advanced fusion drivers. Specifically, such capsules are needed as direct drive targets for the Particle Beam Fusion Accelerator (PBFA) II at Sandia National Laboratory, Albuquerque (SNLA), for use in β-heating studies, and for the Laboratory Microfusion Facility. The large capsule sizes required for these experiments preclude the use of conventional drop-tower technology. At these sizes, aerodynamic drag can seriously distort the shape of molten capsules. The gas could conceiveably be removed from the drop tower, but then the length of the drop tower required increases dramatically. Not only does the capsule accelerate continuously in an evacuated drop tower, but heat transfer is also inhibited. These two factors, combined with the relatively large mass of capsules in the 2 to 10 mm range, combine to make the size of the drop tower needed to process such capsules unrealistically large.

We have found it possible to produce a spherical shell by grinding material away from a highly spherical cavity that has been fused into a glass preform. The cavity is first formed by grinding hemispherical cavities in the flat surfaces of commercially procured glass disks, and then fusing the disks together in a furnace with a rotating process tube. As the glass melts, surface tension provides the spherical shape, while the rotation time averages the gravity vector to zero. Fused voids are characterized using an optical comparator.

Once the void is formed, it is rough-cut from the glass preform with a diamond saw into a nearly spherical shape. The rough form is then machined in a three-point lapper to form the outer surface of the capsule. The three-point lapping technique cuts the wall away uniformly until a desired wall thickness is reached. By changing the grinding compound, we are able to reduce the wall to the desired dimension and diminish the surface roughness until a final polish is achieved using 0.3 μm cerium oxide.

Finished capsules are characterized using our optical comparator. Fast Fourier Transforms are used to describe the shapes of the inner and outer surfaces (and hence the wall thickness uniformity) mathematically. The following sections describe experimental and theoretical developments in this process in the last six months.

Machining and Artificial Microgravity Processing. We have extensive experience in using Pyrex® borosilicate glass to make large fuel capsules. Pyrex® glass is easy to work at temperatures that are achieved readily in our rotisserie furnaces. Using borosilicate glass, we have performed screening tests to evaluate a number of parameters that influence size, sphericity, disk interface, roughness, etc. We realized that there were inherent problems using borosilicate glass, primarily devitrification, weathering of the inside surfaces, and residual water inside the cavity. Fused silica is not readily devitrified and, since it is a single-component material, is not subject to weathering. It is chemically inert, and has high optical clarity. It does, however, require very high temperatures to reach the viscosity necessary to spherate via surface tension. We found that we were pushing our rotisserie furnaces to exhaustion long before we achieved the required sphericity. A few acceptable fused-silica capsules had been made, but these were probably formed only because we had perfect alignment of the spherical hemi-cavity preforms: The glass only had to melt; no appreciable glass transport was required. Borosilicate glass has certain disadvantages, which may be overcome by specific handling techniques. We have experience from a screening experiment with borosilicate glass, in which we examined the effect of 12 independent variables on interior surface roughness, interface visibility, and/or bubbles and sphericity.

The concept of using helium as the void-forming gas (it provides pressure to counter the shrinking effect of surface tension in the melt) has at least two implications: (1) oxygen and water vapor in the void are displaced, eliminating (reducing) the chance for weathering and nucleation points in the capsule, and (2) the helium can be removed readily by out-permeation at temperatures below the annealing point of the glass. Using a helium fill, the gas can be removed without tubes, plugs, or other protuberances in the walls.

The helium-containing voids do not collapse when we provide a helium atmosphere external to the glass. This prevents the helium from escaping and allows the concentration of helium dissolved in the glass to equilibrate and maintain the void size. If necessary, we can reduce the void size by processing the glass in any other gas, since the permeabilities for all other gases are much lower than for helium. That is, the helium comes out of the void much faster than it can be replaced by other gases.

In a comparison test,[40] two 6-mm voids were tacked in air and two in helium. All four voids were then spherated together in a helium atmosphere. The voids that contained air increased significantly in size (1.5 to 2x diameter) upon helium uptake, while the voids that contained helium remained about the same (one increased, one decreased) in size. In crucibles, we observe an increase in void size unless a gas leak occurs from the crucible.

The gas-tight crucible method involves packing the glass disks into a snug-fitting stainless steel crucible made from a piece of tubing. A small fill tube is TIG welded into an end cap, and the cap is welded to the crucible tubing. A slurry of boron nitride is painted on the inside of the crucible to form a mold release. This is dried and burnished to remove loose particulate matter before the disks are loaded. Once loaded, the other end cap is welded on to complete the crucible. The fill tube is connected to a vacuum/helium manifold and the crucible is baked and pumped and back-filled to purge all the air and water vapor. Once the baking is completed, a measured pressure of helium is inserted and the fill tube is crimped to seal the crucible. The crucible is processed to the fusing temperature in a rotisserie furnace, but since the helium is sealed in, it is not necessary to circulate the gas around the outside of the crucible. The crucible is subsequently opened by sawing with a diamond cutting tool. If the mold release were not present, the glass would stick to the crucible and stress cracks would damage the boule of voids.

Voids formed in a helium atmosphere are more spherical than those formed in air. We had not expected this phenomenon, which occurs for both the helium-tacked and the crucible-formed cavities. An evaluation of air and helium processing gases under similar processing conditions[41] for seven air- and nine helium-processed voids indicates an improvement from 5.63% wall nonuniformity (worst of three orthogonal views) for air to 2.08% for helium.

At our processing temperature, the helium distribution should be uniform in the glass matrix after about four hours, if the inside and outside pressures are equal. In this condition, or if there is a greater concentration of helium near the inside, the mobility of the glass is apparently increased, facilitating the formation of a more uniform spherical shape. According to Bansal and Doremus,[42] water and other impurities in silicate glasses lower the viscosity, thereby allowing surface tension to pull the glass to uniform sphericity in a shorter time.

The four main problems we have had with borosilicate glass shells are bubbles, water inside the void, granules in the glass, and weathering. Some of these are not noticeable until the void is machined into a shell. We think we have found the reasons leading to some of these problems. Devitrification has not proved to be a problem, and poor sphericity is reduced using helium.

We have encountered bubbles in three different places within the glass boule, and all of these are adjacent to surfaces: outside surface of cylinder, at disk interfaces, and at the inside surface of the void. Bubbles do not appear to be dispersed through the matrix of the glass, and this causes us to suspect surface contamination.

Liquid has been visible inside finished shells. We suspect that it is water and have been making a greater effort to reduce it by baking the preform at 500°C under vacuum for a day before sealing the pinch-off tube. Water can also be introduced as a product of oxidation of fuels, but the helium-formed voids should eliminate this source. That we have seen liquid in shells that have just been polished indicates that the liquid material is present when the void is formed. A device has been made for breaking voids in cubes of glass inside the reaction vessel of a Karl Fischer apparatus. A water analysis of new voids will tell us if we are actually driving the water out of the voids by treating the preforms.

Granules inside the void are a recently discovered feature. They appear as bubbles near the void surface in shadowgraphs, but a closer look shows them to be solid material. Examination with energy dispersive x-ray spectroscopy (EDXS) has not revealed the nature of the material, but has ruled out boron nitride, which is used as a mold release.

Weathering is due to the redistribution of soluble alkaline materials within the shell. This occurs when liquid or high humidity occurs within the shell, and appears to have diminished when we baked the preforms prior to tacking and fusing. This is noticed on random shells, including two made by the pinch-off technique used earlier. Crystals were noticed in these shells, one before and one after a DT fill. In earlier research, water was observed only after a DT fill but was not looked for previously. In the shells made recently, we have noticed water soon after the shell was polished.

We are still using nine modes of fast Fourier transforms (FFT) of three orthogonal views to produce three-dimensional mapping data of voids and shells. The computer programs have been updated to calculate the three-dimensional results with a minimum of operator input, thereby reducing the possibility of human error in data transfer. In the final analysis of a shell, for example, the operator must present three orthogonal

planes of the shell to the optical comparator (light source). The programs will read 50 data points for inner and outer contours in each of the three views and produce sphericity and uniformity data on the inner and outer contours and wall thickness.

One of our three three-point lapping machines has been converted from spring loading, as used in rough-lapping thicker-walled shells, to differential-pressure pneumatic loading. This provides a more delicate tension, as used on thinner shells in the final contouring stages and for polishing.

Simulation and Modeling.

Dimensional Analysis. In order to qualitatively estimate what is important in processing Macroshell™ spheres made of different materials, we performed an order-of-magnitude dimensional analysis for the void refinement process. We summarize here a number of results from that analysis, which considered fused silica at 1750°C, Pyrex® at 1200°C, and the possibility of processing lithium Macroshell™ spheres at 200°C.

The silica and Pyrex® are very different systems because of a three order-of-magnitude difference in viscosity. In glass, inertia is negligible, so the process is one of surface tension γ overcoming viscosity η, and a characteristic processing time for a void diameter d is

$$t \propto \frac{\gamma d}{\eta}.$$

Thus a three order-of-magnitude viscosity difference translates into a three order-of-magnitude difference needed in processing times for similar transient results. Where a Pyrex® void needs an hour for refinement, a silica void would take days. In both cases, even a very slow rotation rate is enough to overwhelm gravitational processes. Silica could be processed more easily at higher temperatures, but the furnaces are already taxed at 1750°C.

We also looked at temperature and cooling effects on the void. Deformation based on thermal contraction alone during cooling is very small in comparison with void size and cannot account for observed nonuniformities. On the other hand, the bubble must necessarily change significantly in pressure or size between room temperature and processing temperature. If the void size changes and fluid is moving because of changing gas pressure, then during cool-down nonuniformity could result from a temperature gradient and a consequent viscosity gradient across the crucible. This conclusion

regarding the importance of the cool-down step is similar to the conclusion of Wang and Day[43] concerning their rising-bubble experiments.

Molten lithium would be a completely different type of process. The high density and low viscosity of the liquid metal mean that refinement should be accomplished in a fraction of a second, but rotation speeds would have to be very high to keep the void centered.

Centrifugal Effects. Two questions are addressed here: (1) How far off axis will a void travel in a spinning fluid, and (2) what shape will the void have due to the spinning?

For high rotation rates, the void will deform into a prolate shape (eventually into a cylinder) because of the centrifugal force. If fluid dissipation (i.e., drag) may be neglected, then the shape may be found by energy arguments. Since the system is not closed (work is available in any amount through the rotating wall), the system will seek a point of minimum potential energy. Three types of potential energy are present: gravitational, centrifugal, and surface energy beyond the minimum shape of a sphere. By assuming the void is a prolate spheroid, the potential energy may be quantified and numerically minimized over spheroid eccentricity (nonsphericity) and off-axis distance, the two quantities of interest. The gravitational potential energy of the fluid decreases with bubble distance above the axis of rotation. The surface energy is just the product of void surface area with surface tension. The rotational potential energy for the void on axis is just the rotational energy of the missing fluid in the void. However, if the bubble travels off-axis, the rotational potential energy will depend on the flow pattern around the bubble. Two extremes are possible: we can assume that the fluid moves just as it would if the void were not there, or we can assume that a stagnant region forms with roughly the shape and size of the bubble projected around the axis. In the first case, one recovers an off-axis maximum distance of g/ω^2. Unrealistically high rates are needed to make this quantity negligible. In the second case, we find a critical rotation rate above which the bubble has no tendency to travel off-axis at all. Figure 1-36 summarizes these results for the case of a 6 mm o.d. lithium void. The figure shows both distance travelled off axis (as a fraction of void diameter) and the expected nonsphericity of the void based on the prolate spheroid shape. According to the calculations, a rotation rate of 500 to 1000 rpm would give the best balance between these two negative effects.

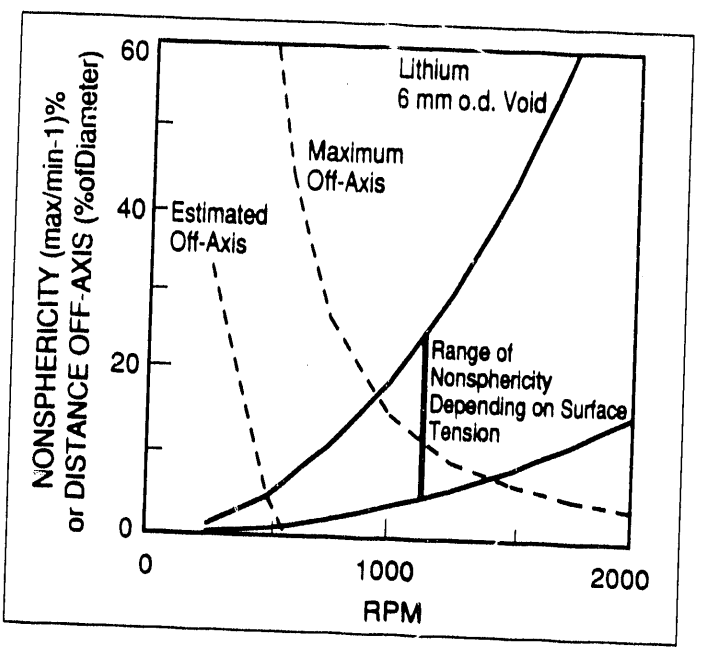

Fig. 1-36. Results from a simulated fabrication of a lithium void showing the competing effects of the angular velocity required to keep the void in the molten metal on-center, and centrifugal force, which tends to distort the void.

For additional information, please contact Thomas O'Holleran

1.4 Coating Technology

During this reporting period KMSF coating activities addressed three major areas of the national inertial confinement fusion (ICF) program:

1. The development and fabrication of films and filters in support of the Particle Beam Fusion Accelerator (PBFA) II program at Sandia National Laboratory (SNL).

2. The further development and deliveries of diagnostic targets for Los Alamos National Laboratory (LANL).

3. Experiments aimed at the optimization of both the glow discharge polymerization (GDP) process and the GDP coaters and support of target deliveries.

1.4.1 Films and Filters

Gold Foils/Diagnostic Lithium Ion Beam Targets. Ion beams rather than lasers will be used by PBFA II to implode targets and produce fusion. For ICF experiments that use ion beams, the uniformity of the intensity profile and the precise focusing of the beam on the fusion target is of great significance. The present status of the PBFA II facility is such that the optimization of the ion beam is the most important problem that has to be solved, with implosion-type target design considerations being secondary. To optimize the lithium ion beams, an image of the beam intensity distribution and its cross section is created through the use of diagnostic Rutherford scattering films. Additional information is obtained by x-ray analysis, which requires the fabrication of very thin metal foils used as x-ray filters. During the past six months, development work on these diagnostic films and filters has been very actively pursued.

The experimental arrangement used for the Rutherford scattering is shown in Fig. 1-37. The sketch shows the arrangement of a gold foil inside the lithium ion beam. The foil, with a thickness around 1 μm, is oriented such that its plane forms a 45° angle with the beam direction. On penetrating the foil, a very few of the lithium ions undergo Rutherford scattering by the gold atoms in the foil at an angle of 90° from the beam axis. The intensity of the beam of scattered atoms in the 90° direction is a function of (1) the primary beam intensity at the scattering center and (2) the number density of gold atoms present at the scattering site. If the number density of gold atoms is the same over

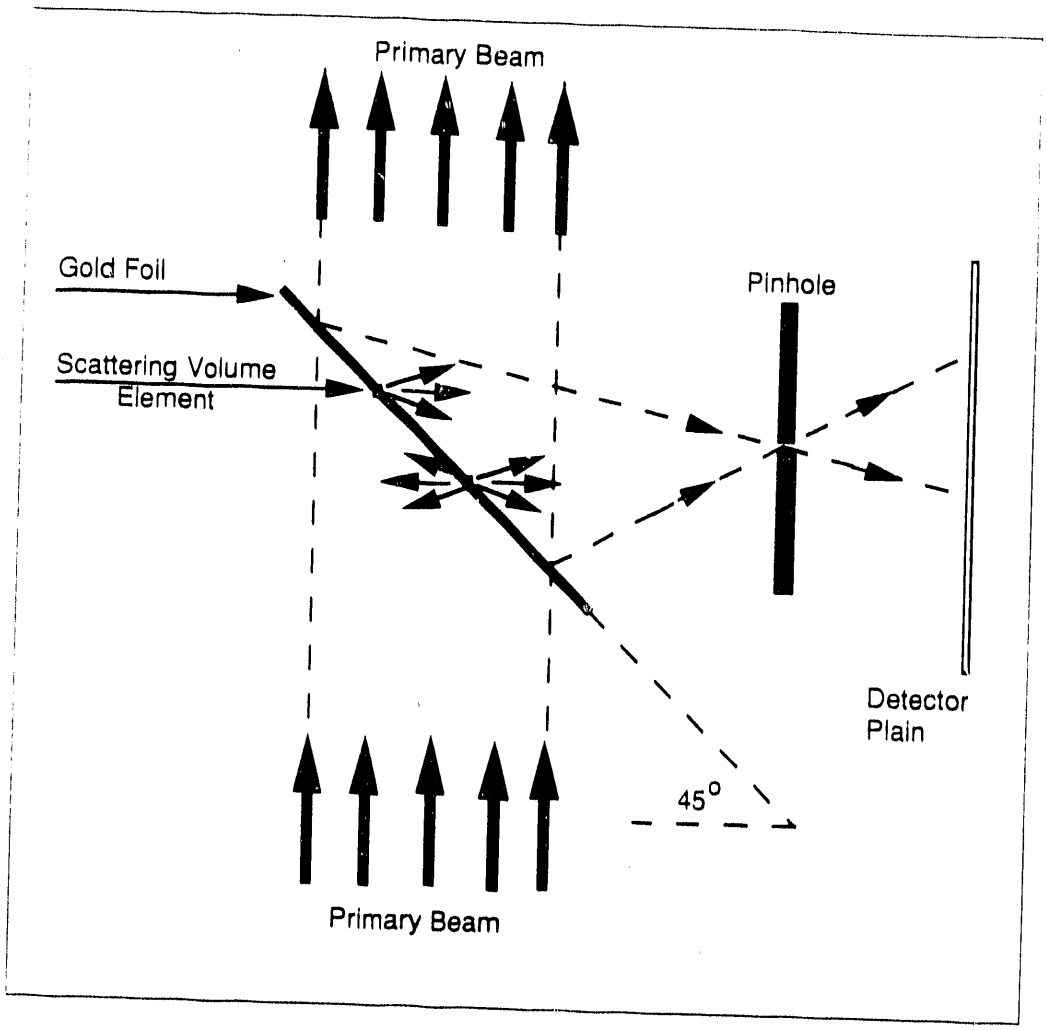

Fig. 1-37. The Rutherford scattering foil scatters a small percentage of lithium ions through a pinhole on an imaging system.

the area of the beam cross-section (i.e., the foil has very uniform thickness) then the intensity of scattered lithium ions carries the information about the primary beam uniformity. In principle, one could then image the beam cross section with (for instance) a pinhole camera.

The films used for this imaging process range in thickness from about 0.25 to 1 μm. Usually they are required to be "free-standing" so that there is no underlying substrate. At the same time, they must span elliptical or circular areas (as shown in Fig. 1-38) up to roughly 2.0 x 1.5 in. This can lead to very unfavorable high-stress conditions in these very large, very thin metal films. The films are attached to a metal frame in such a manner that they have an absolute minimum of wrinkles. An additional requirement in some cases is that these films must have fiducial marks which may consist of precise holes cut through the very thin gold films or markers of different materials deposited on the basic gold film, as shown in Fig. 1-39.

In spite of the fact that there are very few commercial operations that can perform this job (we only know of one) KMSF has performed this task successfully with some technology transfer from SNL. We also have developed the procedures to the point that we can deliver films of a quality that was previously unavailable.

While the diagnostic lithium-beam foils are made out of very pure gold, we also have started to make x-ray filter foils from a variety of different materials. We have made both organic foils and metal foils, using metals other than gold. For both organic and metal foils, we have dedicated and modified deposition equipment to handle large quantities of high quality films and filters with very short delivery times. In addition we have purchased equipment to perform precise characterizations of each film and deliver it with full characterization documentation.

Fabrication of Gold Rutherford Coatings on Low-Z Substrates. Some of the diagnostic films requested consist of a 1 μm gold coating on a 1 μm Mylar® substrate attached to a large brass frame. The resulting diagnostic foil has to satisfy two requirements: (1) it must be of well characterized, uniform thickness; and (2) it must be completely flat without wrinkles in the center region of the film. The deposition has to be made with the aid of a mask, which in turn determines the location and the dimension of the marker. It is a characteristic of the Mylar® films used as substrates that they develop stresses during the deposition of the gold film, which lead in turn to the formation of unwanted wrinkles (see Fig. 1-40). The wrinkles are removed by heating the film with a heatgun. This is a delicate operation, which has a direct bearing on the yields of the

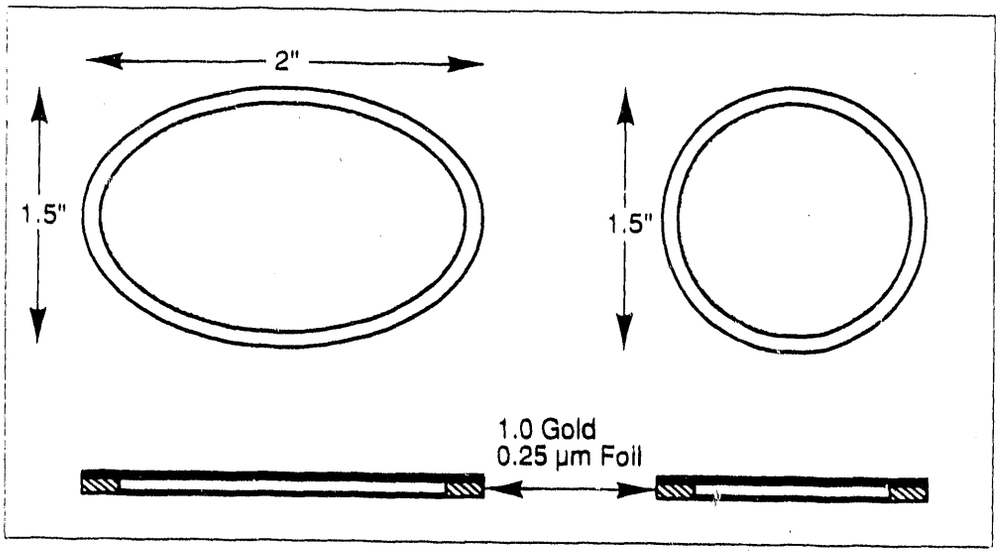

Fig. 1-38. Both substrate-supported and free-standing gold films are fabricated in two basic geometries, circular and elliptical.

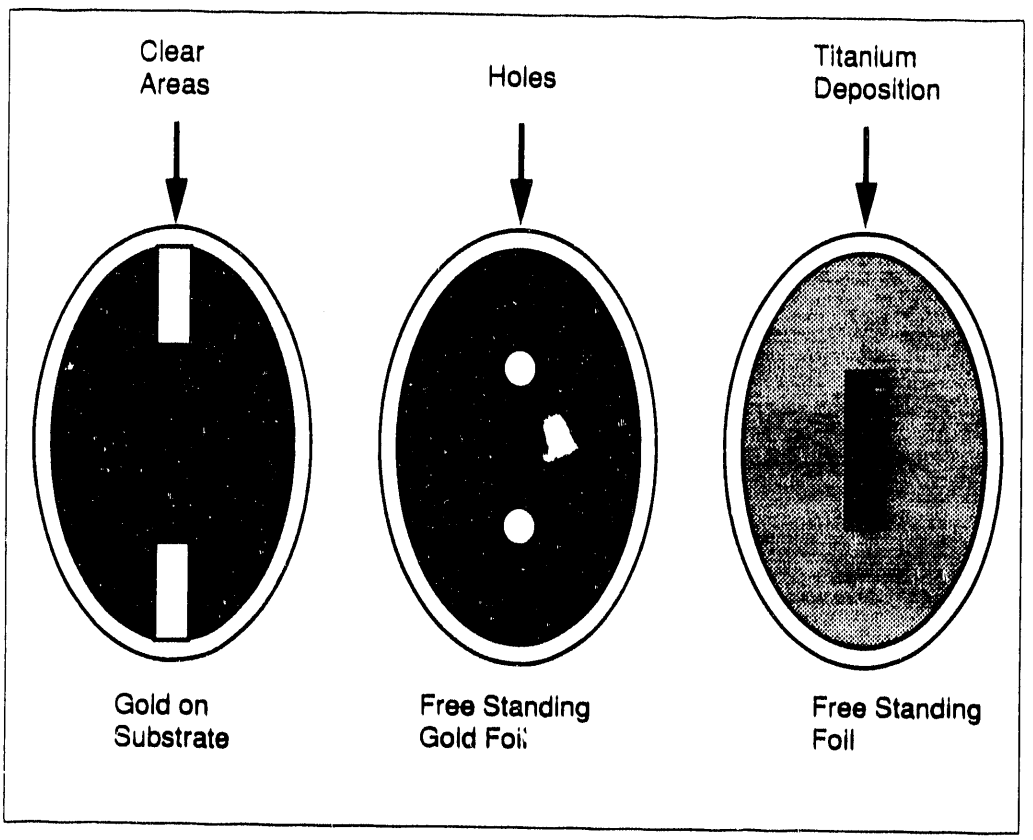

Fig. 1-39. Fiducials on Rutherford scatter targets are of three types: Clear areas; holes, additional deposition (titanium).

Fig. 1-40. Before heat-treatment, the foil is severely wrinkled.

process. In this operation it is very easy to destroy foils by applying too much heat, while insufficient heat simply will not remove the wrinkles (see Fig. 1-41). Once successfully fabricated, the gold-on-Mylar® foils are fairly robust and, when properly packed, can be shipped safely.

In some instances the foils must have physical holes for fiducials, as indicated in Fig. 1-42. Again, since these holes are used as markers to reference the location of the image of the beam cross-section with respect to the diode structure, they have to be very precise in both location and dimension. We had to develop a process that permitted the fabrication of the holes without causing damage to the remainder of the film. We chose to cut these holes with a pulsed Nd:YAG laser with the film on the frame mounted on a precision rotary plus X-Y-Z table. This arrangement is shown in Fig. 1-43. This process is now developed to the point that we can fabricate about 20 foils per week.

Other foils or films require the addition of a fiducial of a second metal (titanium). Even though these combinations of coatings most often lead to the formation of stresses, which lead in turn to warping and tearing of films, we were able to find operating conditions that enabled us to produce even some of these films meeting specifications in all respects. This was a novel and challenging problem that we were able to solve very quickly.

Fabrication of Free-Standing Gold Films. Some configurations for the free-standing gold films of interest are shown in Fig. 1-44. For the thicknesses required, between 1.0 and 0.25 μm, the specified nonuniformity of these films has to be less than 10%. The size of the films on the frames (that is, the free-standing area) is of the order of a few square inches.

The fabrication process for these films is shown in Fig. 1-45 and described below:

1. Glass slides are coated with a very uniform and smooth film of NaCl.

2. Gold is deposited onto these NaCl surfaces.

3. The frames (metal or plastic) are glued to the gold layer.

4. After the glue hardens, a cut through the gold film down to the NaCl is made around the frame.

5. The whole assembly of slide, film, and frame is supported on a fixture with standoffs and then immersed into distilled water.

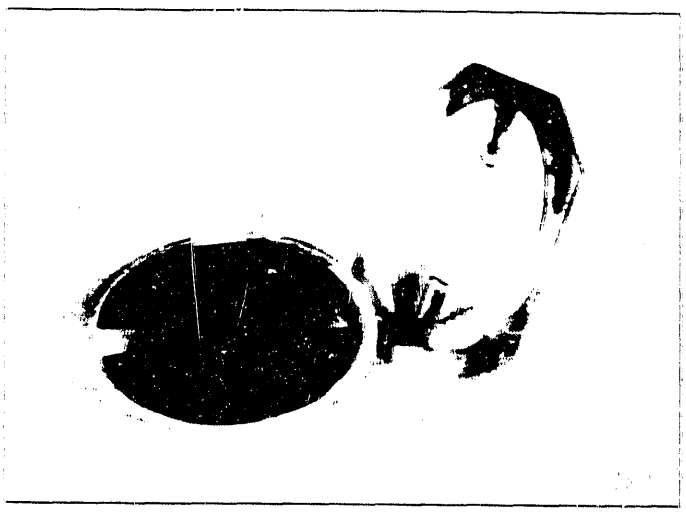

Fig. 1-41. After heat-treatment, a small amount of wrinkling remains around the sharp corners of the fiducials.

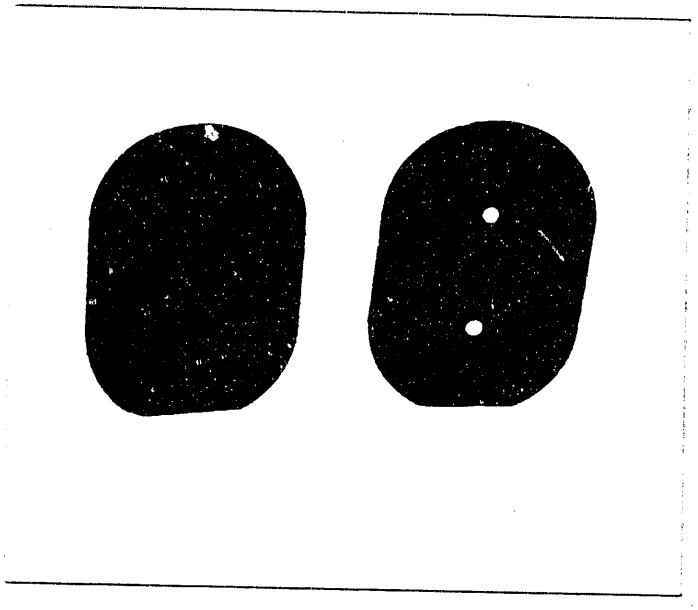

Fig. 1-42. Circular fiducials are "laser machined" into free-standing foils. Left: before machining. Right: after machining.

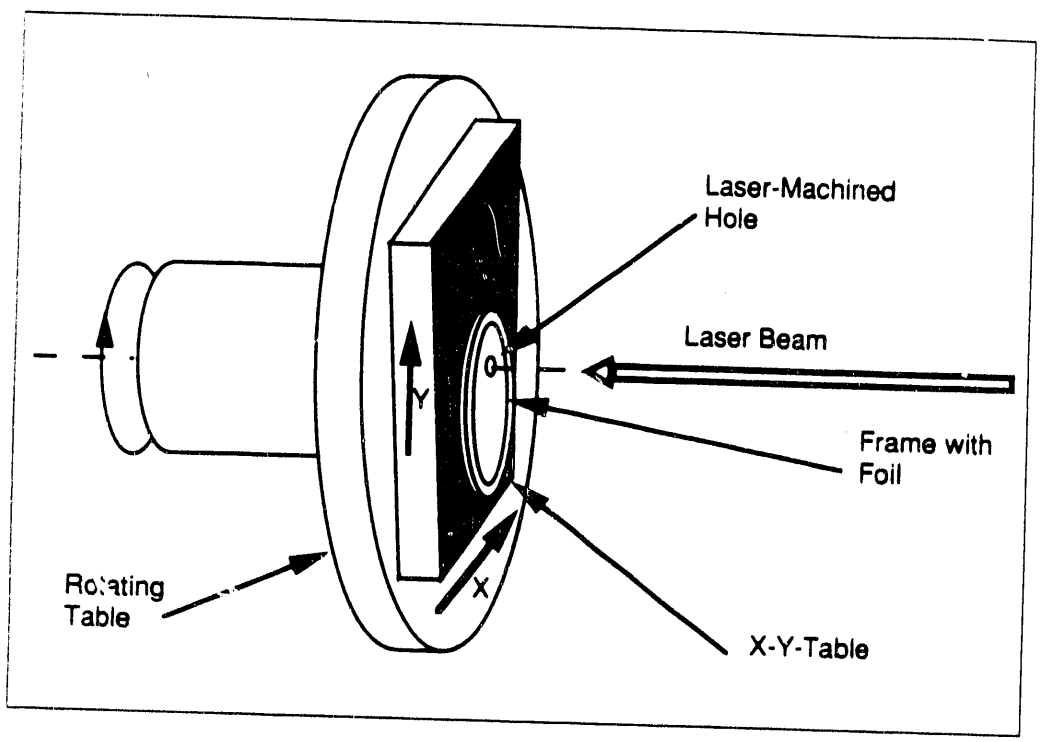

Fig. 1-43a. Schematic drawing of the "laser machining" fixture.

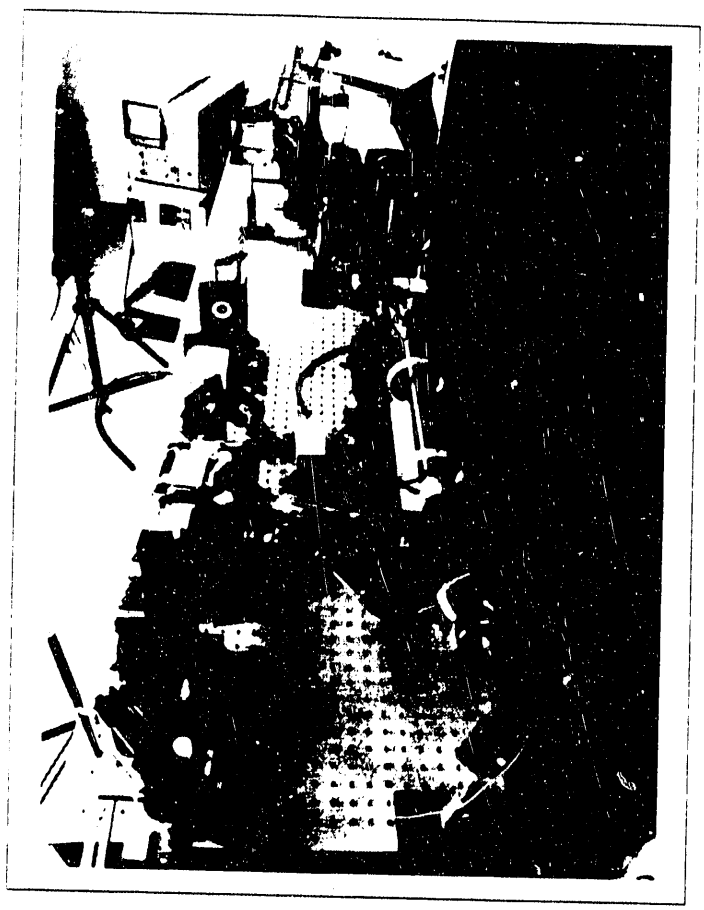

Fig. 1-43b. Laser machining requires an elaborate arrangement of equipment.

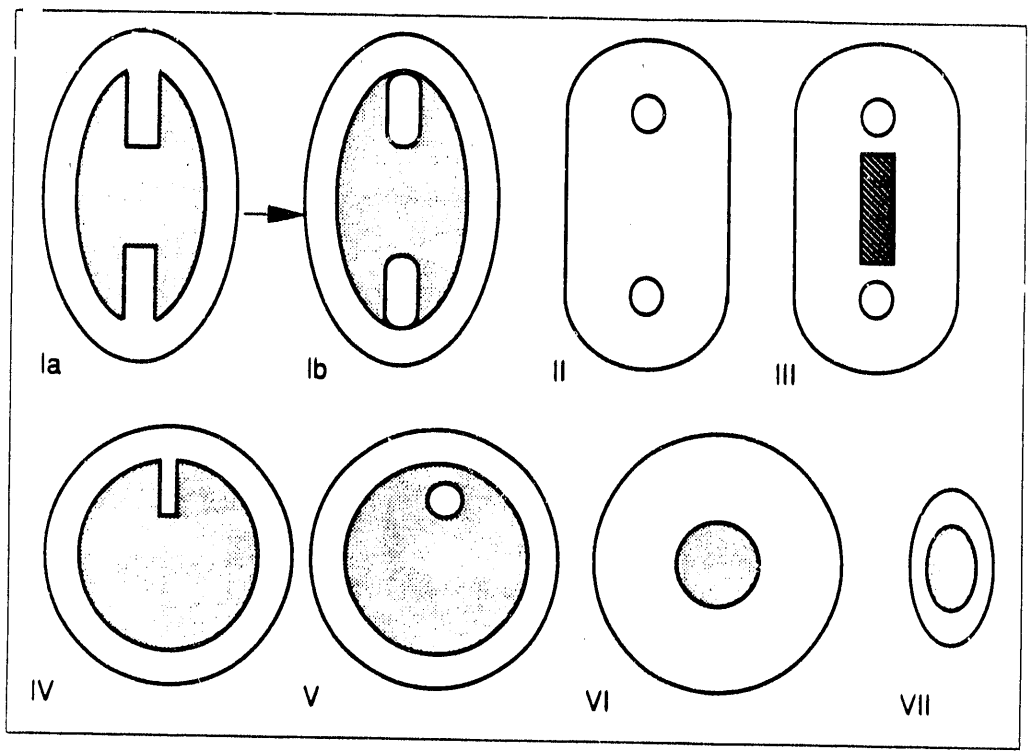

Fig. 1-44a. Films and filters come in many different configurations.

Fig. 1-44b. Size comparison of the smallest Rutherford scatter films and a penny.

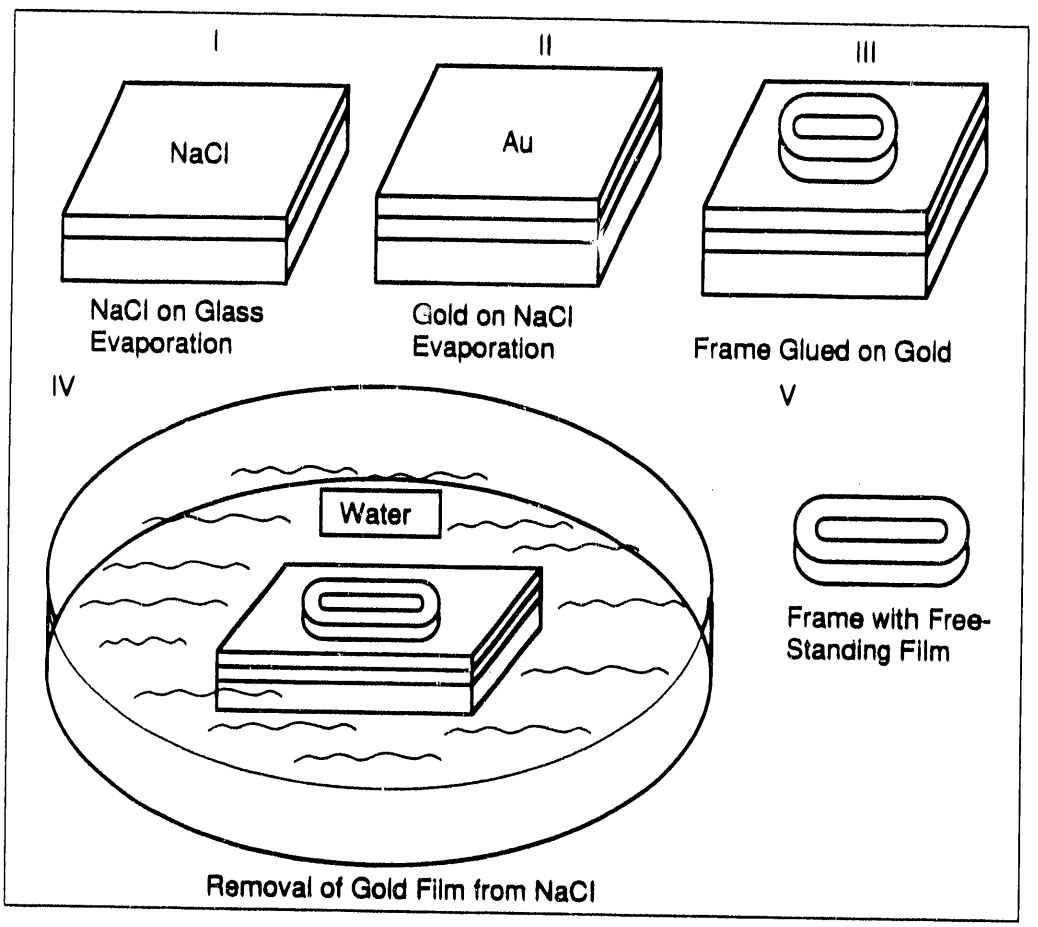

Fig. 1-45. Free-standing gold films require two deposition steps.

As the water dissolves the NaCl, the frame (still with the gold film attached) falls off and, after careful drying, is ready for laser machining as described previously. Special care has to be given to the very thin 0.25 μm films since they are very sensitive to mechanical shock or rough air movement. Success in this work depends on the correct preparation of the NaCl substrate, the removal procedure in water, and the subsequent handling and packing procedures.

X-ray Filters. The x-ray filters consist of very pure, thin films of metals or polymers. The films must be very uniform in thickness. These filters can be free-standing single foils or double foils. The arrangements of foils may be single metal, single polymer, metal-metal, metal-polymer and possibly polymer-polymer. The main problem areas in the fabrication of such foils are the prevention of wrinkles and stresses, the lack of mechanical strength, or the brittleness of some of the materials. An additional requirement for the free-standing foils is that they must be deposited on removable substrates. The removal process must be such that it will not alter or destroy the remaining foils.

In the case of the polymer films, the manufacturing methods for some of the requested materials are complex and can only be used by commercial producers. Purchasing these materials in the right thickness is not always possible since the manufacturers produce materials of standard thicknesses in large quantities, leaving the availability of the required thicknesses to chance. In the past KMSF has developed equipment to produce small quantities of films of some materials such as variants of parylene, Formvar®, and films produced with the GDP process which might prove useful in the future.

Free-Standing Thin Metal Films Made by Physical Vapor Deposition. Thin metal films of various materials are needed for x-ray filter applications. The materials presently requested are parylene-N, aluminum, titanium, vanadium, nickel, chromium, Saran, Teflon®, molybdenum, niobium, tin, and silver. Common to the fabrication of these films is that all free-standing films have to be deposited on a removable substrate. For the gold we used NaCl films deposited on glass slides as the substrate so that, after the gold deposition, the gold film could be removed by dissolving the NaCl film in water. This is possible because of the inertness of the gold film to the exposure to other chemicals.

If, however, the desired x-ray filter film consists of other materials, such as aluminum or copper, then the solution of NaCl in water could attack the film itself and destroy it. So depending on the material in question, we have to develop appropriate new processes. Even though the conditions are somewhat different for different filter materials, there are some universal conditions. One such condition is that the substrate must be able to withstand the deposition temperature and not lead to chemical reactions or alloying with the film material. Another condition is that the removal process (i.e., the solvent) not destroy or damage the film in any way.

Since the choice of materials in the ICF program does change frequently (based on our experience in the past), time-consuming development work is necessary in many cases. A typical approach for the fabrication of thin filter films involves the use of soluble polymers as substrates. KMS Fusion has made filter films with soluble polymer substrates in which the substrate material was attached to the filter frame and, after deposition, was dissolved away in the area of interest. Another area requiring possible development work is the removal or prevention of stresses in the films. Although some information about the formation of stresses in thin films and their prevention can be found in the literature, only a few papers address the procedures that permit the fabrication of totally stress-free films. Techniques for fabricating low-stress films are dependent upon the material in question and require different methods of deposition and control of the substrate's temperature. Again, this is an area of development that needs to be addressed in every individual case. KMSF is working on these problems.

For additional information, please contact Hubert Lintz

1.4.2. Diagnostic Components

Two types of diagnostics are fabricated to study the effects of mass inhomogeneities or mass perturbations in the walls of fuel containers on the symmetrical compression of the shells:

1. Gaussian bumps and Gaussian bands (aluminum and CH)

2. NaCl layers between CH layers.

Methods were developed for the fabrication of aluminum and CH bumps and CH bands. A method for the production of aluminum Gaussian bands is still in the developmental stage.

The fabrication of NaCl layers was accomplished very early but requirements for greater uniformity of the layer thickness and a smoother surface of the NaCl layer necessitates the continuation of development work.

Gaussian Bumps. The main effort in the fabrication of aluminum and CH Gaussian bumps in this reporting period addressed the reproducibility of the bump characteristics like height and full width at half maximum (FWHM). Although only a relatively small number of targets of this kind were to be delivered, a large number had to be fabricated to cover losses during the processing following bump deposition. Initial adhesion problems were overcome and presently the bump deposition has become a more-or-less routine operation with a yield of over 80%. A problem related to the bump is the formation of an unwanted perturbation on the surface of the CH coating which is applied after the bump deposition. We previously reported that the perturbation was successfully removed with an Excimer laser. Meanwhile, however, a new method became available which uses machining on a diamond lathe to remove the perturbation. This work was done at Los Alamos National Laboratory (LANL) since KMSF does not have a diamond lathe. Additional work on the precise removal of the unwanted perturbation is in progress at Rocky Flats, Colorado.

Gaussian Bands. There has also been considerable progress in the fabrication of Gaussian bands although deliveries have not yet been made. The original approach of depositing the aluminum band through a special aperture has led to considerable problems. The precision needed to manufacture the parts for this fixture cannot be achieved on conventional machinery. LANL's first attempt (made with a deposition

fixture of their own) did not work out because of the fragile nature of the shells to be coated. The shells are very easily crushed. A new approach is under investigation in which we will attempt to coat the shell with a heavy band of aluminum around the equator with a subsequent diamond machining step to achieve the precision of the band cross section.

It seems that the CH Gaussian band can be manufactured by slicing rings from a polystyrene (PS) shell and then melting these rings onto the shell in question. Fig. 1-46 shows a photograph of a shell with a melted-on PS ring.

NaCl Diagnostic Layers. Shells with NaCl diagnostic layers have been produced and delivered. The work on both the surface finish and the thickness uniformity of the NaCl layers continues. The improvement of the thickness uniformity is somewhat tied into further improvement of the analytical tools used to measure the uniformity. We have recently obtained very encouraging results concerning the surface smoothness of these layers and are presently awaiting tests of their reproducibility.

Polymer Coating Technology. It has become more and more obvious that the GDP process needs more investigation and optimization. Both the GDP coating teams at Lawrence Livermore National Laboratory (LLNL) and at KMSF have found that the performance of GDP systems seems to vary from run to run. At this time no one seems to know what the underlying causes are for the sporadically occurring problems. We have found in the past that the specific materials present in the reaction zone of the helical resonator have an effect on the performance. To study the importance of the various parameters we modified an existing GDP system. In our first set of experiments we have found that things like powder formation may be related to both geometrical design as well as the electrical properties used for the construction of the reaction chamber. This work will be very beneficial for the future improvement of GDP system design and will hopefully continue this year. Most of the activities in this task were concentrated on the construction of new equipment in support of target deliverables.

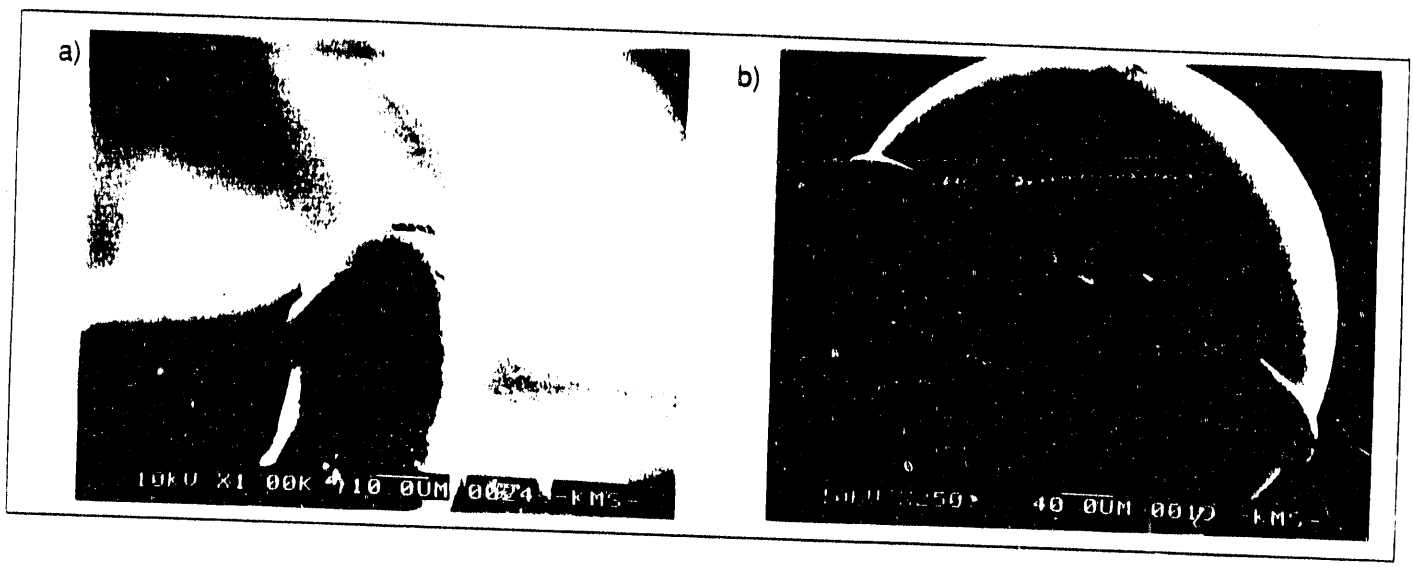

Fig. 1-46. CH Gaussian bands are made of rings of PS melted onto the target.

For additional information, please contact Hubert Lintz

1.5 Microfabrication and Assembly

Although this group was officially formed only as of January 1, 1990, many of the group members were engaged in target deliveries over the entire reporting period, October 1989 through March 1990. During this period, the group did prepare and characterize certain targets used for experiments at KMSF on the Chroma laser facility; since January 1, 1990, however, activities have been focused on fabrication, characterization, and shipping of targets to Lawrence Livermore National Laboratory (LLNL), Los Alamos National laboratory (LANL), and the University of Rochester, Laboratory for Laser Energetics (LLE).

Most of the targets delivered by this group do not require extensive research and development. Those more specialized targets (such as those delivered to Sandia National Laboratory [SNL]) are delivered to the national laboratories by other KMS groups such as Coatings Technologies and Capsule Fabrication. The target deliveries to LLNL, LANL, and UR/LLE will be detailed below.

1.5.1 Target Deliveries to LLNL

The task statement of work (SOW) is used as the guide for target deliverables to LLNL, but no deliveries are made until specifically requested. In this way, changing needs in the LLNL program are best served.

This process is illustrated by the following examples from 1989. Glass capsules with dimensions of 1200 μm x 3 μm filled to a pressure of 25 atm were indicated on the SOW. However, none were requested, so none were delivered. The same situation was encountered with glass capsules of dimension 440 μm x 10 μm at various D_2 or DT pressures (and CH coating when required). None were requested and none were delivered. By contrast, we had a request for 100 glass capsules of dimension 360 μm x 9 μm at various D_2 or DT pressures (and coated with CH when required). Of the 100 requested, we delivered 97. In fact, of the items requested, there was only one order that we were unable to fill, namely an order for 40 polymer composite shells. The technical problems that prevented us from completing that order have now been solved and we are shipping polymer composite shells to LLNL at present.

In addition to the items specified in the SOW, we also receive requests from LLNL that are not on the SOW. Specifically, LLNL requested 51 glass shells with larger Δw than target-quality with dimensions 370 μm x 9 μm. We delivered 73 of these. Also LLNL requested 12 polystyrene (PS) shells with approximate diameter of 1500 μm . We were able to deliver four of these. Targets delivered to LLNL in 1989 are shown in Table 1-7.

Table 1-7. LLNL Target Deliveries for 1989

Target Name	Shell Material	Number Requested	Number Sent	O.D. (μm)	Wall (μm)	Fill Gas	Pressure (atm)	Coating	Uniformity (μm)
KMSO53	Glass	8	8	350-390	8.0-10.0	DT	5		$\Delta w \leq 0.5$
KMSO54	Glass	8	7	350-390	8.0-10.0	DT	10		$\Delta w \leq 0.5$
KMSO55	Glass	8	8	350-390	8.0-10.0	DT	100		$\Delta w \leq 0.5$
KMSO56	Glass	6	6	350-390	8.0-10.0	DD	5	CH	$\Delta w \leq 0.5$
KMSO57	Glass	6	2	350-390	8.0-10.0	DD	10	CH	$\Delta w \leq 0.5$
KMSO58	Glass	6	4	350-390	8.0-10.0	DD	100	CH	$\Delta w \leq 0.5$
KMSO59	Glass	15	21	350-390	8.0-10.0	DT	51		$\Delta w \leq 3.0$
KMSO60	Glass	6	3	350-390	8.0-10.0	DT	5	CH	$\Delta w \leq 0.5$
KMSO60	Glass	3	6	350-390	8.0-10.0	DT	5	CH	$\Delta w \leq 0.5$
KMSO61	Glass	6	4	350-390	8.0-10.0	DT	10	CH	$\Delta w \leq 0.5$
KMSO62	Glass	6	6	350-390	8.0-10.0	DT	100	CH	$\Delta w \leq 0.5$
KMSO63	Glass	6	6	350-390	8.0-10.0	DT	5		$\Delta w \leq 0.5$
KMSO64	Glass	6	6	350-390	8.0-10.0	DT	10		$\Delta w \leq 0.5$
KMSO65	Glass	6	6	350-390	8.0-10.0	DT	100		$\Delta w \leq 0.5$
KMSO66	Glass	15	17	350-390	8.0-10.0	DT	25		$\Delta w \leq 0.5$
Rb Samples	Glass	12	24	350-390					
Rb Samples	Glass	24	28	350-390	8.0-10.0				$\Delta w \leq 3$
PS Samples	Polymer	12	4	~1500	12.0-25.0				
PVA Samples	Polymer		6	435-455	2.0-4.0				

Table 1-7. LLNL Target Deliveries for 1989

Target Name	Shell Material	Number Requested	Number Sent	O.D. (μm)	Wall (μm)	Fill Gas	Pressure (atm)	Coating	Uniformity (μm)
KMSO53	Glass	8	8	350-390	8.0-10.0	DT	5		Δw≤0.5
KMSO54	Glass	8	7	350-390	8.0-10.0	DT	10		Δw≤0.5
KMSO55	Glass	8	8	350-390	8.0-10.0	DT	100		Δw≤0.5
KMSO56	Glass	6	6	350-390	8.0-10.0	DD	5	CH	Δw≤0.5
KMSO57	Glass	6	2	350-390	8.0-10.0	DD	10	CH	Δw≤0.5
KMSO58	Glass	6	4	350-390	8.0-10.0	DD	100	CH	Δw≤0.5
KMSO59	Glass	15	21	350-390	8.0-10.0	DT	51		Δw≤3.0
KMSO60	Glass	6	3	350-390	8.0-10.0	DT	5	CH	Δw≤0.5
KMSO60	Glass	3	6	350-390	8.0-10.0	DT	5	CH	Δw≤0.5
KMSO61	Glass	6	4	350-390	8.0-10.0	DT	10	CH	Δw≤0.5
KMSO62	Glass	6	6	350-390	8.0-10.0	DT	100	CH	Δw≤0.5
KMSO63	Glass	6	6	350-390	8.0-10.0	DT	5		Δw≤0.5
KMSO64	Glass	6	6	350-390	8.0-10.0	DT	10		Δw≤0.5
KMSO65	Glass	6	6	350-390	8.0-10.0	DT	100		Δw≤0.5
KMSO66	Glass	15	17	350-390	8.0-10.0	DT	25		Δw≤0.5
Rb Samples	Glass	12	24	350-390					
Rb Samples	Glass	24	28	350-390	8.0-10.0				Δw≤3
PS Samples	Polymer	12	4	~1500	12.0-25.0				
PVA Samples	Polymer		6	435-455	2.0-4.0				

Request for LLNL 1990 deliveries are as follows:

1. The SOW calls for KMSF to supply 80 Type "A" glass shells by April 30, 1990. As of April 4, 1990, 77 had been delivered, with 12 more to be delivered by end of April.

2. The SOW calls for KMSF to supply 40 Type "B" glass shells, filled with gas, in groups of 10 per month by April 30, 1990. To date, 15 have been delivered and the rest are selected and ready to be filled, but LLNL has not specified the fill pressure. LLNL verbally asked us to hold them.

3. The SOW calls for KMSF to supply 40 Type "C" glass shells in groups of 10 per month after April 30, 1990. Twelve had already been delivered as of April 4, 1990.

4. LLNL has requested 75 low-Z capsules (classified dimensions), to be delivered at a rate of seven to eight per month . We have delivered 10 samples that LLNL states are of the same quality as they make (and hence would be acceptable). The specifications for specific targets were not received until April 2, 1990, so that no targets have actually been delivered. Manufacture is underway and these will be delivered by May 1, 1990.

5. We have a request for three maximum-size glass shells filled to ≈ 200 atm. We have delivered four of these.

6. In addition to the items specified in the SOW, we had a request for ≥12 glass shells with dimensions 1000 μm x 3 μm @ 25 atm. To date, we have delivered 22.

7. We have requests for two batches of >1200 μm glass shells. Ten are to be filled to 25 atm while 5 are to be filled to 50 atm (on a best-effort basis). There are no due dates on these requests, but they will be completed without delay. The actual delivered targets (for both LLNL and LANL) for 1990 are shown in Table 1-8.

Table 1-8. LLNL and LANL Target Deliveries for 1990

Laboratory	Target Name	Shell Material	Number Requested	Number Sent	O.D. (μm)	Wall (μm)	Fill Gas	Pressure (atm)	Coating	Uniformity (μm)
LANL	LANL1:90	Glass	10	10	340-360	1.8-2.2			25-32 μm CH	Δw≤0.2
LANL	LANL2:90	Polymer	20	23	350-370	3.0-3.4			0.8 μm CH	
LANL	LANL3:90	Glass	5	6	340-360	1.8-2.2			Al Bump 25-32 μm CH	Δw≤0.2
LLNL	KMSB01	Glass	15	15	350-390	8.0-10.0	DT	50		Δw≤3.0
LLNL	KMSC01	Glass	6	6	440-480	9.0-11.0	DT	100		Δw≤0.7
LLNL	KMSC02	Glass	6	6	440-480	9.0-11.0	DT	50		Δw≤0.7
LLNL	KMSO57	Glass	4	3	350-390	8.0-10.0	DD	10	CH	Δw≤0.5
LLNL	KMSO61	Glass	2	5	350-390	8.0-10.0	DT	10	CH	Δw≤0.5
LLNL	KMSO66	Glass	15	17	350-390	8.0-10.0	DT	25		Δw≤0.5
LLNL	KMSO67	Glass	15	16	350-390	8.0-10.0	DT	50		Δw≤0.5
LLNL	KMSO68	Glass	10	10	350-390	8.0-10.0	DT	100		Δw≤0.5
LLNL	KMSO69	Glass	10	10	350-390	8.0-10.0	DT	10		Δw≤0.5
LLNL	KMSO70	Glass	10	10	350-390	8.0-10.0	DT	100		Δw≤0.5
LLNL	KMSO71	Glass	7	8	350-390	8.0-10.0	DT	50		Δw≤0.5
LLNL	KMSO72	Glass	6	6	350-390	8.0-10.0	DT	25		Δw≤0.5
LLNL	LLNL(H)	Glass	3	4	600-700	≈ 9	DT	200		
LLNL	LLNL(I)	Glass	≥12	22	950-1050	≈ 3	DT	25		
LLNL	Samples	Composite	10	10	435-455	~2-3			~2-3 μm PVA CH	

1.5.2 Target Deliveries to LANL

The target deliveries to Los Alamos National Laboratory are structured to follow the Statement of Work (SOW). The actual deliveries for 1989 are shown in Table 1-9. In addition, some of the requested targets have additional features not specified in the SOW. Some of these features are as follows:

Item 2: Better CH bump removal; Better bump characterization and better surface characterization where bump was removed

Items 4,5,11: Better NaCl layer uniformity.

Most targets were delivered nearly on time or even earlier than the SOW date.

Item 13 was not in the original SOW, but it was requested and delivered.

For 1990, the SOW called for three deliveries to LANL by March 1, 1990, with the next set of deliveries due on May 1, 1990. The status of these requests at the time of this writing was as follows:

Item 1: 350 x 2 μm glass plus 27 μm CH: 10 requested, 10 sent.

Item 2: 360 x 4 μm polymer: 20 requested, 23 sent.

Item 3: 350 x 2 μm glass plus aluminum bump plus 27 μm CH: 5 requested, 6 sent. The CH bump not removed per LANL instruction. They will machine the bump away.

Refer to Table 1-8 for the actual delivered targets to LANL in 1990 to date.

Table 1-9. LANL Target Deliveries for 1989

Target Name	Shell Material	Number Requested	Number Sent	O.D. (μm)	Wall (μm)	Fill Gas	Pressure (atm)	Coating	Uniformity (μm)
LANL1:89	Glass	20	26	340-360	1.8-2.2			25-32 μm CH	Δw≤0.2
LANL2:89	Glass	5	5	340-360	1.8-2.2			Al Bump 25-3 μm CH	Δw≤0.2
LANL3:89	Glass	7	8	340-360	1.8-2.2	DT	15	25-32 μm CH	Δw≤0.2
LANL4:89	Polymer	15	15	350-370	3.6-4.4			0.5 μm NaCl 25-32 μm CH	
LANL5:89	Polymer	10	10	350-370	3.6-4.4			0.5 μm NaCl 25-32 μm CH PS Bump	
LANL6:89	Polymer	10	8	350-370	3.6-4.4			0.5 μm NaCl 25-32 μm CH 2 PS Bumps	
LANL11:89	Polymer	10	14	500-520	4.0-4.5			1.8 μm CH 0.5 μm NaCl 17-20 μm CH	
LANL13:89	Glass	12	12	950-1150	2.0-7.0	DT	56		

For additional information, please contact Wayne Miller

1.5.3 Target Deliveries to UR/LLE

The task description for KMSF target deliveries to UR/LLE consists of two parts: (1) fabricating and delivering glass and polymer shells and (2) filling returned shells in eggcrates with D_2 or DT to required fill pressure.

During this reporting period, KMSF performed one DT fill for LLE. It was a 200 atm fill in which 45 of the 52 glass shells in the eggcrate survived. The fill was a deemed a success because the ratio of diameter to wall thickness for many of the shells was nearly 100:1. LLE target personnel measured sample shells and confirmed that the fill pressure achieved came to within 2% of the requested value.

Two glass shell batches in the diameter range of 240 to 260 μm were delivered during this reporting period. Targets having wall thicknesses of 3, 4, 5, or 6 μm were available for culling from these two batches.

Six polymer shell batches of four varieties were also delivered. It must be noted that the majority of the shells in these batches were not considered "target quality" because of LLE's stringent target requirements. For instance, the "state of the art" of plastic shell fabrication does not yet meet LLE's requirement for < 5% nonconcentricity of all layers of composite CH shells. In order to develop the technologies which can meet these requirements and at the same time to keep LLE supplied with "near target quality" shells, KMSF delivered an assortment of shell batches for evaluation and possible use as targets. Table 1-10 lists the types of polymer shell batches delivered during this reporting period:

Table 1-10. Polymer Shell Deliveries to LLE - Oct. 1989 through Mar. 1990

Type of CH Shell	Specifications	Number of Batches
Microencapsulated PS	220-245 x 2-30 μm	3
Microencapsulated PS overcoated with PVA	220-245 x 2-30 μm 1-3 μm PVA	1
Drying Column PS overcoated with PVA	220-245 x 2-4 μm PS 1-3 μm PVA	1
Filled Drying Column PS overcoated with PVA	220-245 x 3-7 μm PS+PVA 0.5 atm argon fill	1
Total number of batches:		6

For additional information, please contact David Steinman

1.6 References:

1. *1989 Annual Technical Report*, KMS Fusion, Inc., Ann Arbor, MI. KMSF-U2339. Section 1.5.8, Automated Interferometry for Rapid and Accurate Characterization of Transparent Shells .

2. Ibid.

3. Ibid., Section 1.5.9, "Paraxial Model of Shell Interferometry."

4. *1989 Annual Technical Report*, KMS Fusion, Inc., Ann Arbor, MI. KMSF-U2339.

5. 1989 Semi-Annual Technical Report, KMS Fusion, Inc., Ann Arbor, MI. KMSF-U2205, Section 1.5.2.

6. R. L. Downs, M. A. Ebner, B. D. Homyk, and R. L. Nolen, *J. Vac. Sci. Technol.* **18**(3), 1272-1275 (1981).

7. R. F. Probstein and R. E. Hicks, *Synthetic Fuels* (McGraw-Hill, Inc., 1982).

8. H. H. Storch, N. Golumbic, and R. B. Anderson, *The Fischer-Tropsch and Related Syntheses* (John Wiley & Sons, Inc., New York, 1952).

9. W. H. Beattie, "The Radiolysis of Mixtures of Carbon Dioxide and Hydrogen," LA-4657, UC-4 Chemistry, TID-4500, Los Alamos Scientific Laboratory, Los Alamos, NM, June 1971.

10. W. H. Beattie, "The Radiolysis of Mixtures of Carbon Monoxide and Hydrogen," LA-4658, UC-4 Chemistry, Los Alamos Scientific Laboratory, Los Alamos, NM, June, 1971.

11. R. G. Schneggenburger and M. A. Ebner, *KMS Fusion 1989 Annual Technical Report*, KMS Fusion, Inc., Ann Arbor, MI, KMSF-U2339.

12. M. A. Ebner, W. J. Miller, and L. T. Thompson, "The Reactivity of Residual Blowing Gases in Glass Shells," Proceedings of the Sixth Target Fabrication Specialists Meeting, LA-UR-89-200, Los Alamos National Laboratory, Los Alamos, NM, June 20-24, 1988, pp. 144-148.

13. Landau and Lifshitz, *Fluid Mechanics*, 2nd edition, Vol. 6 (Pergamon Press, 1987), Sections 15, 49, 55.

14. Gary A. Glatzmaier, "Numerical Simulations of Stellar Convective Dynamos," *J. Comp. Phys.* **55** (1984), pp. 461-484.

15. Paul N. Swartzbauber, "On the Spectral Approximation of Discrete Scalar and Vector Functions on the Sphere," *SIAM J. Numer. Anal.* **16**(6) (Dec.1979), p. 934-949.

16. *KMS Fusion 1989 Annual Technical Report on Inertial Fusion Research* (KMS Fusion, Inc., Ann Arbor, MI). KMSF-U2339.

17. LLE Review **40** (University of Rochester, Rochester, NY, 1989), p. 205.

18. *KMS Fusion 1988 Annual Technical Report on Inertial Fusion Research* (KMS Fusion, Inc., Ann Arbor, MI), p. 19. KMSF-U2116.

19. T. R. Pattinson, D. L. Musinski, and W. J. Felmlee, "The Role of Sandwich Holography in Inertial Confinement Fusion," *J. Vac. Sci. Technol. A* **7** (1989), pp. 993-995.

20. C.M. Vest, *Holographic Interferometry* (John Wiley & Sons, 1979), p. 275.

21. J. S. Ankney, D. L. Musinski, W. J. Felmlee, and T. R. Pattinson, "Holographic Interferometry Evidence that ß-Decay Energy Can Symmetrize Solid Deuterium-Tritium Samples," *J. Vac. Sci. Technol.* A (to be published).

22. J. S. Ankney, D. L. Musinski, and W. J. Felmlee, "Shell Surfaces Affect Cryogenic Fuel Layers," Proceedings of the 3rd Target Fabrication Specialists' Meeting CONF-8404169 Vol. IV, p. 133-148, September, 1984. KMSF-U1422.

23. R. P. Reedy, "Selection and Measurement of Microsphere Laser Targets Based on Refraction," *J. Appl. Phys.* **47** (1976), pp. 2502-2508.

24. R.L. Downs, M.A. Ebner, B.D. Homyk and R.L. Nolen, "Analysis of Glass Shell Blowing Gases from Metal-Organic Gels," *J. Vac. Sci. Technol.* **18** (1981), p. 1272-1275.

25. M. T. Mruzek, J. S. Ankney and D. N. Decker, "Apparatus for Verification of Beta Heating Driven Layer Uniformity in Solid DT," *J. Vac. Sci. Technol. A* **6**(3) (May/Jun 1988), p. 1889-90.

26. M. T. Mruzek and W. J. Felmlee, "Study of X-ray Emissions from Cold Deuterium-Tritium Fuel Inside Glass Targets for ICF," *J. Vac. Sci. Technol. A* (to be published).

27. Hyo-Gun Kim, Memo of March 30, 1989.

28. Steve Noyes, January 29-30, 1990.

29. *1986 Annual Technical Report on Inertial Fusion Research,* KMS Fusion Inc., Ann Arbor, MI. KMSF-U1871.

30. J. O. Hirschfelder, C. F. Curtiss, and R. B. Bird, *Molecular Theory of Gases and Liquids* (Wiley, New York,1954).

31. R. B. Bird, W. E. Stewart, and E. N. Lightfoot, *Transport Phenomena* (Wiley, New York, 1960).

32. R. J. Clift, R. Grace, and M. E. Weber, *Bubbles, Drops, and Particles*. (Academic Press, New York, 1978).

33. K. Masters, *Spray Drying Handbook*, 4th edition (Wiley & Sons, New York, 1985).

34. H. C. Van Ness and M. M. Abbott, *Classical Thermodynamics of Nonelectrolyte Solutions* (McGraw-Hill, New York,1982).

35 F. A. Bovey and F. H. Winslow, *Macromolecules* (Academic Press, New York, 1979).

36 H. Schlichting, *Boundary-Layer Theory* (McGraw-Hill, New York, 1979).

37. *1987 Annual Technical Report on Inertial Fusion Research*, KMS Fusion Inc., Ann Arbor, MI. KMSF-U1962.

38. K. R. Amundson, D. W. Bousfield, and D. S. Soong, "Rheology of Microsphere Formation and Refinement," *J. Appl. Phys.* **59**(7), 2306-2313 (1986).

39. R. B. Bird, R. C. Armstrong, and O. Hassager, *Dynamics of Polymeric Liquids-Vol. 1 Fluid Mechanics*, 2nd edition (Wiley, New York, 1987).

40. DMS-5595-WJF.

41. DMS-5566-DGS.

42. N. P. Bansal and R .H. Doremus, *Handbook of Glass Properties* (Academic Press, Orlando, FL, 1986) p. 7.

43. S. C. P. Wang and D. E. Day, *A Technique for Producing Glass Macro Shells For ICF Targets*, (Univ. of Missouri-Rolla, 1988).

SECTION TWO. LASER PLASMA INTERACTIONS

Douglas J. Drake, Scientific Editor

Introduction

The Department of Laser Plasma Interactions (LPI) at KMS Fusion (KMSF) contributed to the goal of achieving high gain, inertially confined fusion during the reporting period by developing diagnostics for the fusion program, conducting experimental campaigns on the Chroma laser, and performing theoretical and computational analysis in support of local and off site inertial confinement fusion (ICF) experiments.

A high energy x-ray continuum spectrograph under development at KMSF will contribute to the ensemble of ICF diagnostics for Nova. KMSF will supply the diffracting crystal and mechanical assembly for the device, and Lawrence Livermore National Laboratory (LLNL) will supply the detector. The Laue transmission geometry chosen for the instrument should improve detection of weak signals, allow use of shorter crystals and reduce background. Various proposed designs are discussed in this report.

KMS Fusion is also developing a diagnostic for the Aurora laser at Los Alamos National Laboratory. In this case, the instrument will be an 266 nm optical probe, which will initially be used to obtain Schlieren images. Future use of the probe in a holography system is foreseen.

Ionization balance and interpenetrating plasma experiments were conducted during the period.

The ionization balance experiments were a refinement of an earlier set of experiments conducted in 1987 at KMSF to gain information on the kinetics of ion level populations. K-shell and L-shell emitters were subjected to a varying laser irradiance. Improved diagnostics were used to record the time-resolved spectral data, allowing us to observe, among other things, the evolution of electron population inversions in levels of interest for potential x-ray laser schemes. The most recent set of experiments, concentrating on L-shell spectroscopy, provided a wealth of data, which is still being analyzed. It should provide important information on the temperature and density conditions at early times after short pulse laser irradiation for a number of materials of interest.

Correct treatment of interpenetrating plasmas may prove critical to the accurate modeling of laser fusion experiments. However, the physical complexity of the process makes simulation of such plasmas a difficult task. It is difficult to adapt lagrangian hydrocodes to such problems in any case. Experiments are essential to ensure that hydrocodes can model the process adequately.

An experimental program investigating interpenetrating plasmas was conducted during the reporting period. A description is given of the useful insights gained through the experiments along with preliminary theoretical interpretation of results.

Finally, computational and theoretical work performed during the reporting period on interpretations of the thin, high density jets of relatively cold plasma seen in several experiments at KMSF is discussed. These jets make their appearance when high-Z materials are irradiated with pulsed laser beams. The radiation cooling instability is proposed as a likely mechanism for cold jet formation, and the implications of the instability for laser pulse shaping schemes are discussed.

2.1 X-ray Spectrogram Design and Development

2.1.1 High Energy X-ray Continuum Spectrograph for Aurora

An x-ray spectrograph has been designed to take high energy x-ray continuum measurements from Aurora for inertial confinement fusion (ICF) diagnostics. The complete instrument package consists of a crystal spectrograph for recording the hard x-ray continuum over the energy range of 5 to 35 keV and two high energy channels for recording a time-resolved, integrated continuum in the 40 to 60 keV and 60 to 90 keV energy bands. The continuum spectrograph is to provide continuous spectral coverage over the entire energy interval of 5 to 35 keV. The high energy channels consist of filtered CsF scintillators for wideband, high time resolution measurements at discrete high energy points.

The 5 to 35 keV continuum spectrograph is shown in Fig. 2-1. The spectrograph uses a de Broglie curved crystal geometry with LIF 200 ($2d = 4.03$ Å) and PET 002 ($2d = 8.75$ Å) as the diffracting crystals. Both crystals have the same radius of curvature and diffract the same Bragg angles. There is a large amount of overlap in the spectral coverage of each crystal. A single two-dimensional (2-d) detector records both spectra simultaneously. Time integrated spectra are to be obtained with an energy resolution $E/\Delta E$ of the order of 20. The detector for the spectrograph is a 40:1 microchannel plate (MCP) proximity focused to a phosphor-coated fiber optic that is lens coupled to a charged coupled device (CCD) camera. On receipt of an event trigger synchronized to the laser shot, spectral data are recorded by the camera and transferred to a computer for storage and display.

A de Broglie geometry was chosen for the continuum spectrograph after considering a number of alternatives. The choice of the de Broglie geometry is very specific to the requirements of this particular instrument. These requirements are that continuous spectral coverage be provided over the large energy interval of 5 to 35 keV with low energy resolution, that data be recorded electronically, and that the entire package fit in the space available on a 6-in. port on the Aurora target chamber. Additional space within the experimental port is also required to accommodate the two separate high energy channels. A Laue geometry was initially considered for this instrument because of certain advantages inherent to the transmission geometry at high energies, but was discarded because of the difficulty of matching a suitable detector to the spectrograph in the available space.

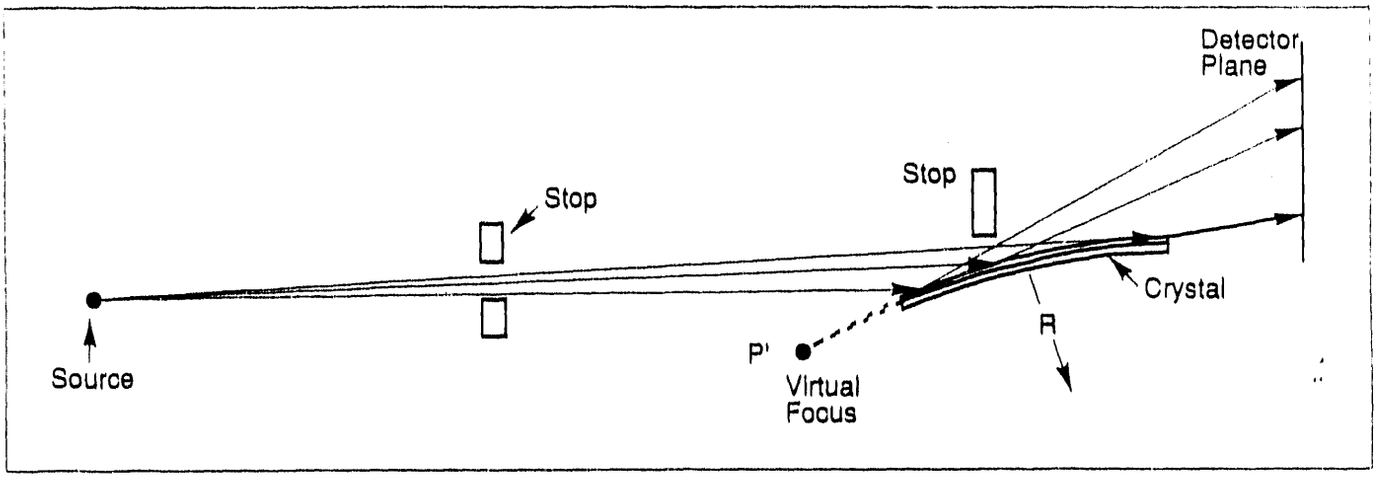

Fig. 2-1. Mechanical layout showing the major components of the continuum spectrograph for Aurora.

The de Broglie geometry adapted for high energy x-rays is shown in Fig. 2-2. Because of the high energies involved, the Bragg angles are small and approach grazing incidence for the upper energy limits even for crystals having small 2d values. The convex curved crystal increases the Bragg angles available in the given solid angle from a point source. For small Bragg angles, a relatively large energy range is diffracted in the forward direction and is sufficiently compressed that it can be recorded with low energy resolution with a compact position sensitive detector. By close coupling the detector to the crystals it is possible to obtain the low dispersion required for high sensitivity. Since small Bragg angles are involved, both incident and diffracted rays are close to the line of sight to the source, and a compact design is possible that will fit in the space available. An additional feature of this geometry is that due to the convex curvature of the crystal, the source is demagnified. For a slitless spectrograph with resolution limited by source size, this has the effect of lessening the dependence of energy resolution on source parameters. The main disadvantage of the de Broglie geometry at high energies is that, because Bragg angles are close to grazing incidence, accurate placement of stops is critical to avoid shine through and prevent background.

A MCP was chosen for the detector for the continuum spectrograph. Phosphor intensified photodiode arrays were also considered, but the MCP was found to provide greater sensitivity in this energy region. Microchannel plates have the additional advantage of providing (two-dimensional) 2-d readout. They possess high gain, so that signal processing electronics can be simple, and are inherently low noise. Two-dimensional readout is a great advantage for determining sources of stray background and for introducing real time calibration marks, such as K-edge filters, for energy calibration.

The MCP is proximity focused to a phosphor-coated fiber optic. The phosphor used is P-20 which provides efficient coupling to a CCD. Spatial resolution is 50 to 100 μm and is more than adequate for the energy resolution required. The 2-d data are transferred by the fiber optic to the focal plane of the camera lens and read out using a commercial CCD camera.

A Cohu 6500 was chosen for the CCD camera because it uses the TC-243 CCD chip. This CCD has a frame transfer architecture and incorporates on chip correlated double sampling to provide an order of magnitude reduction in readout noise over comparable CCD cameras. This greatly improves the camera sensitivity. The camera has adequate sensitivity in this application without the need for cooling.

The camera lens and electronics are mounted in a remote camera head that is compact and fits easily onto the spectrograph. The electronics allow for a remote trigger as well as for time integration. Integration periods as long as 4 s are possible before dark current becomes

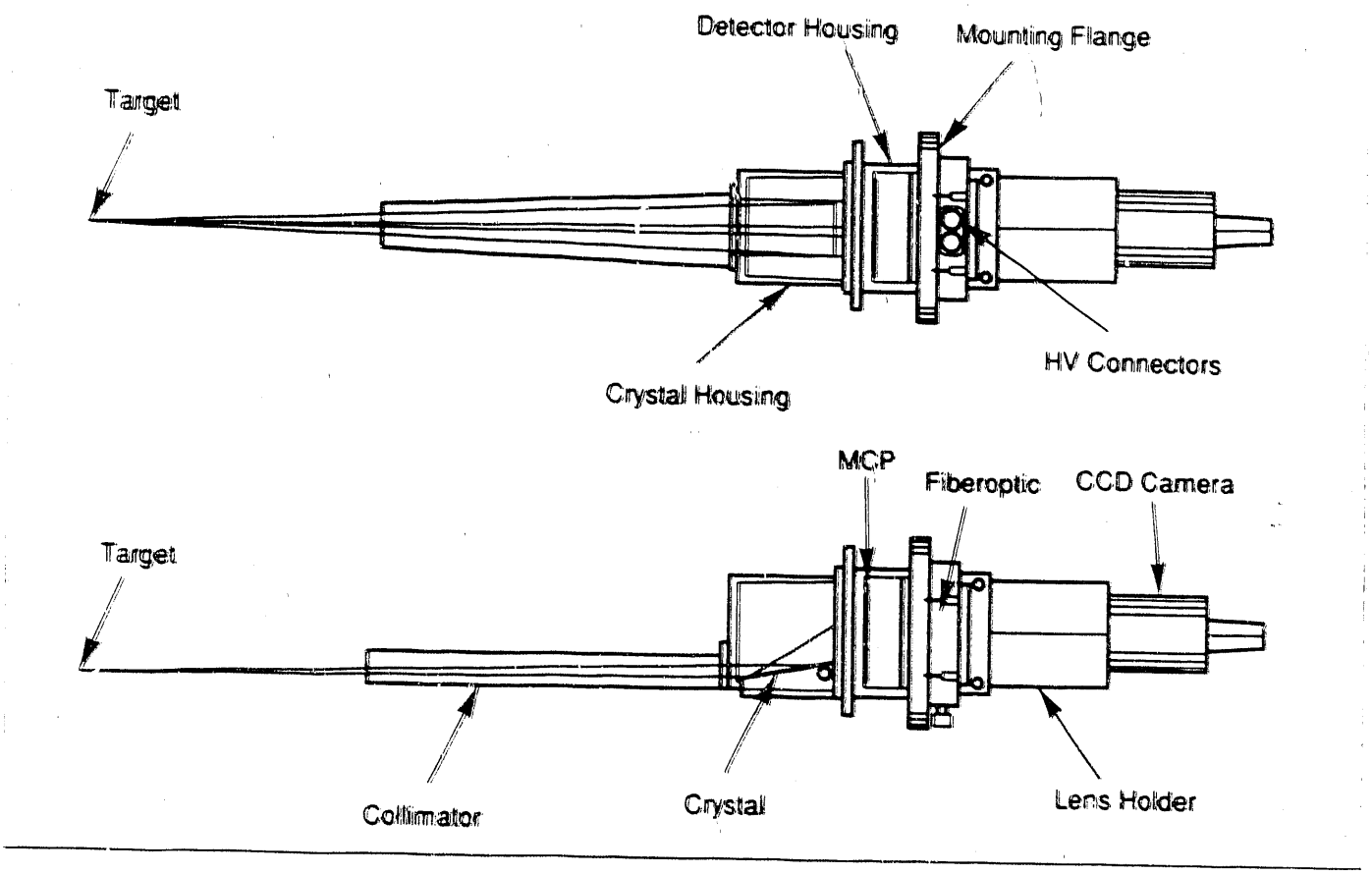

Fig. 2-2. The continuum spectrograph for Aurora uses the de Broglie geometry. A convex curved crystal increases the available Bragg angles from a point source. For high energies, the energy range of interest diffracted in the forward direction is sufficiently compressed that it can be recorded with a single detector. Accurate placement of stops is critical in this geometry when used at small Bragg angles.

objectionable. This feature is useful for laboratory evaluation with dc x-ray sources. The camera is compatible with AT based framegrabbers.

The mechanical layout identifying the major components of the continuum spectrograph is given in Fig. 2-1. A set of stops in the collimator assembly defines the optical axis to which the crystals are aligned. The crystal holder provides for adjustment of the crystals in both height and angle. The detector housing has a 10 mil Be window that provides both a 4 keV low energy cutoff and vacuum isolation for the MCP. The MCP housing is isolated from the target chamber vacuum and is pumped separately by its own vacion pump. Internal components that are viewed directly by the MCP are made of aluminum to reduce background due to fluorescence. Aluminum fluorescence that is generated internally is effectively blocked by filtering it through the 10 mils of Be in the MCP housing. Heavier shielding is used for external filtration.

The mechanical layout of a high energy channel is shown in Fig. 2-3. The two high energy channels consist of collimated filtered scintillators for recording integrated continuum in the 40 to 60 keV and 60 to 90 keV energy bands. A collimator defines a small field of view around the source. The energy band of interest is defined by a K-edge filter of the appropriate thickness. The filter is mounted on the front end of the collimator to reduce the amount of fluorescence that can produce background at the scintillator. Background is further reduced by a set of baffles placed in the collimator tube. The high energy cutoff in the energy response of the detector is defined by the scintillator material and its thickness. Cesium fluoride was chosen for the scintillator material because it has good x-ray absorption efficiency for this energy region, can provide a reasonably sharp high energy cutoff and has the shortest decay time of the inorganic scintillators. The scintillation efficiency is 6% of NaI and the decay time is about 5 ns. The scintillator is coupled to a 19 mm Hamamatsu R1450 photomultiplier tube (PMT). This PMT has excellent timing characteristics.

The data acquisition system for the Aurora instrument package is illustrated in Fig. 2-5. In response to a trigger, 2-d video data from the CCD camera are captured by a framegrabber and transferred to a computer for data storage and display. Data from the high energy channels are sent to transient digitizers for time resolved information, and to CAMAC compatible charge integrators for intensity information.

The entire instrument package is shown in Fig. 2-4. A reentrant design was chosen with all instruments mounted on a common housing. The camera, PMTs, and associated electronics are located in air and are electrically isolated from the target chamber ground. The package fits inside a 6-in. tube and is mounted by a standard 8-in. conflat flange to a 6-in. target chamber

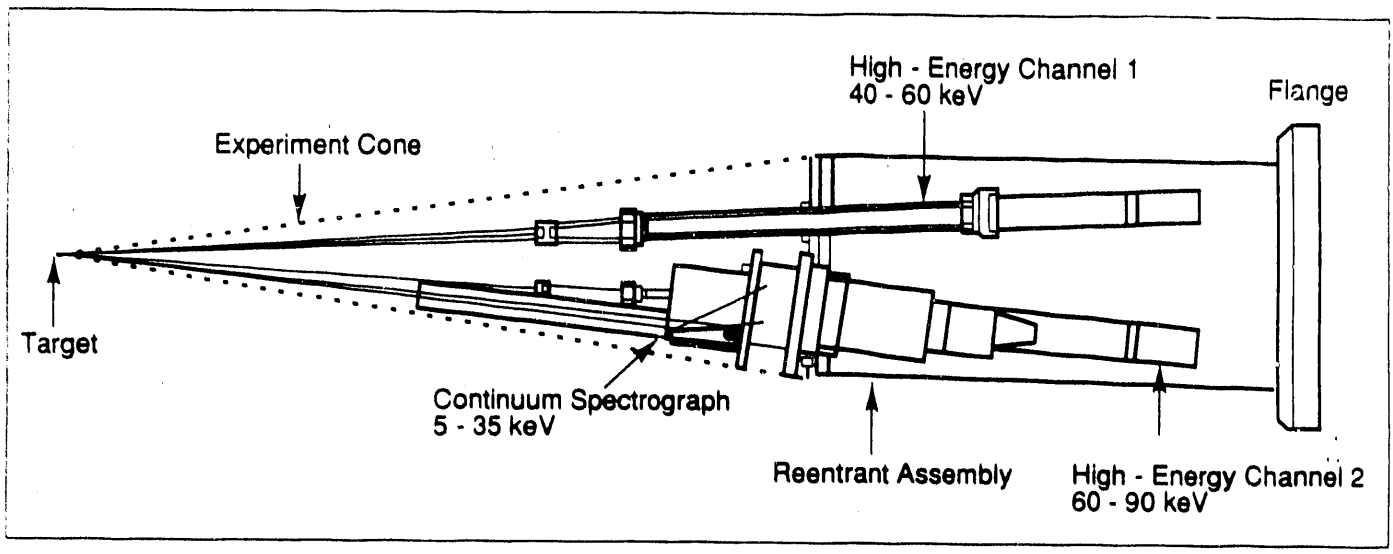

Fig. 2-3. The two high energy channels consist of filtered CsF scintillators. CsF is used for high time resolution.

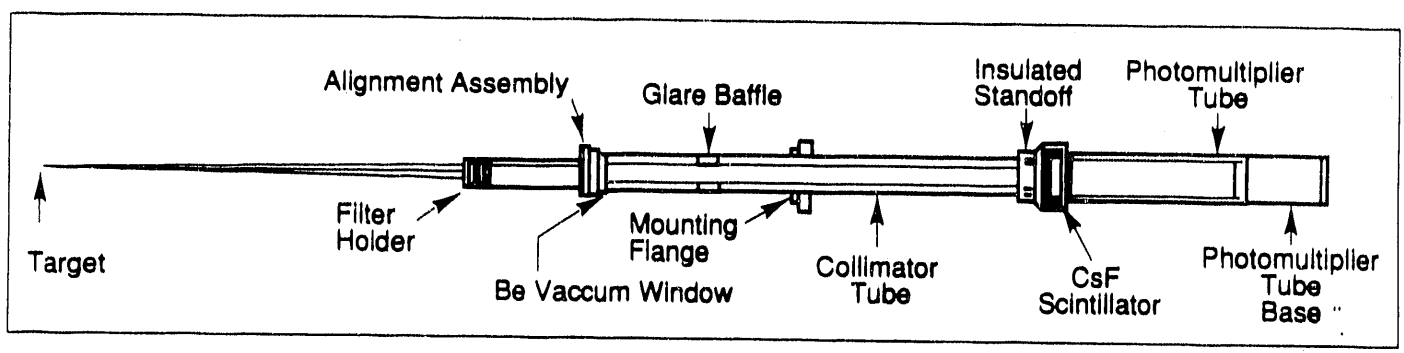

Fig. 2-4. The instrument package for Aurora is mounted in a reentrant assembly. The three instruments are to be coaligned and co-calibrated. An 8-in. flange holds the 6-in. i.d. reentrant tube for mounting to a 6-in. target chamber port.

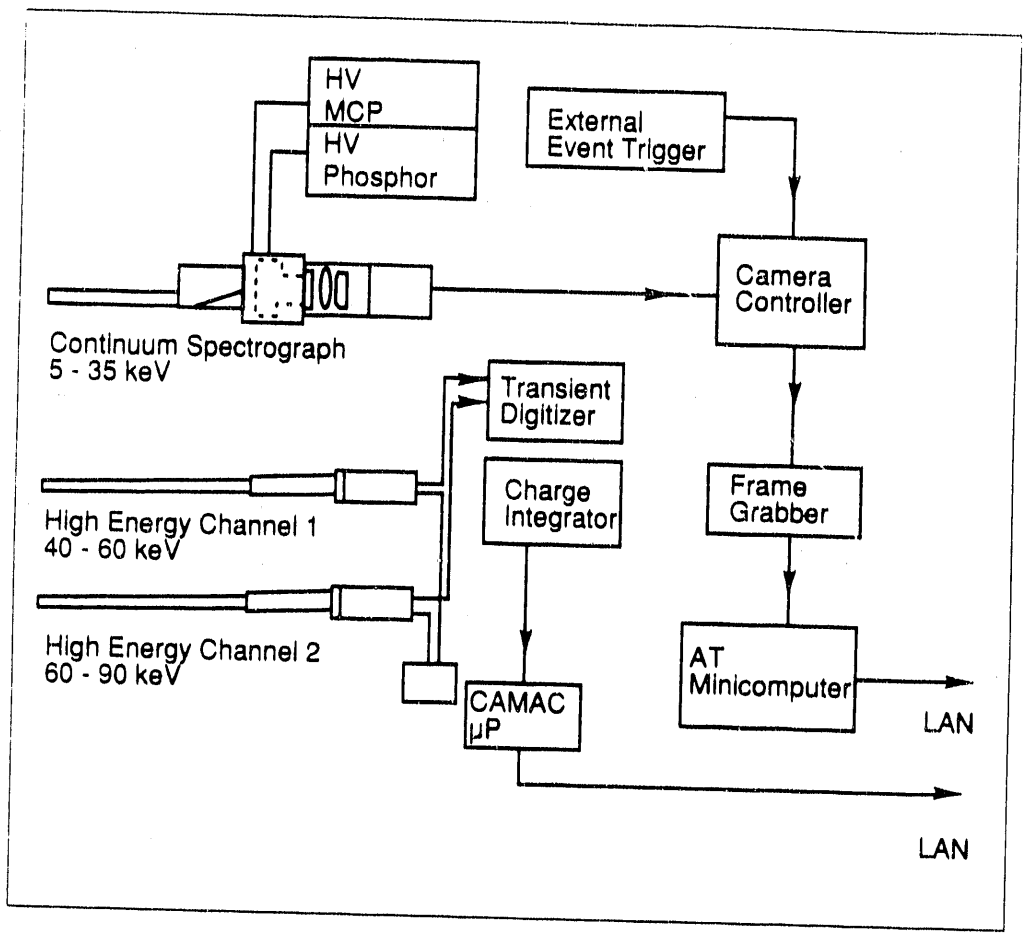

Fig. 2-5. Outline of the data acquisition system for the Aurora instrument package.

port. Provision is made for adapting to an 8-in. port if necessary, and the entire package can be electrically isolated if required through use of a Lucite™ isolation flange. All instruments are to be coaligned and co-calibrated prior to shipment to Los Alamos National Laboratory (LANL) using the calibration facilities at KMS Fusion.

The high energy test stand designed for calibration of the Aurora instrument package is shown in Fig. 2-6. The x-ray source is a standard four port, water-cooled, 2.5 kW, 60 kV, sealed x-ray tube with tungsten anode. A spot or line focus is available depending on the orientation of the tube. Spot size is nominally 0.4 mm^2 while the line focus has dimensions of 0.04 x 8 mm. The x-ray tube can be mounted on the test chamber so that the line focus is either horizontal or vertical. The x-ray tube is interchangeable with standard sealed tubes having anode materials other than tungsten. Tungsten was chosen for this application because of the need for a continuum source and because tungsten is an efficient fluorescence excitation source. Because of the beryllium window on the x-ray tube and test chamber entrance port, the lowest energies available in direct excitation are about 5 keV. This low energy limit can be extended to lower energies by using fluorescent excitation because the fluorescent target shares the test chamber vacuum. Fluorescence excitation has the great advantage that it provides pure monochromatic lines free of continuum background.

Although the energies involved for the Aurora calibration permit operation of the test chamber in air, provision was made for vacuum operation to allow for the calibration of vacuum sensitive devices such as MCPs and to accommodate low energy fluorescent sources. Provision is also made for using a calibrated Si(Li) detector for determining the energy and intensity characteristics of the x-ray source. Accurate source characterization is essential for overall instrument calibration.

The test chamber is designed to accept the entire Aurora instrument package. When mounted on the test chamber flange, the instruments are at the design distance to the source. This allows end to end calibration of each instrument as well as co-calibration and coalignment of the entire package to a common, well characterized continuum x-ray source. Calibration and testing of individual components at high x-ray energies for prototyping is also possible as is calibration in discrete spectral lines using fluorescence excitation.

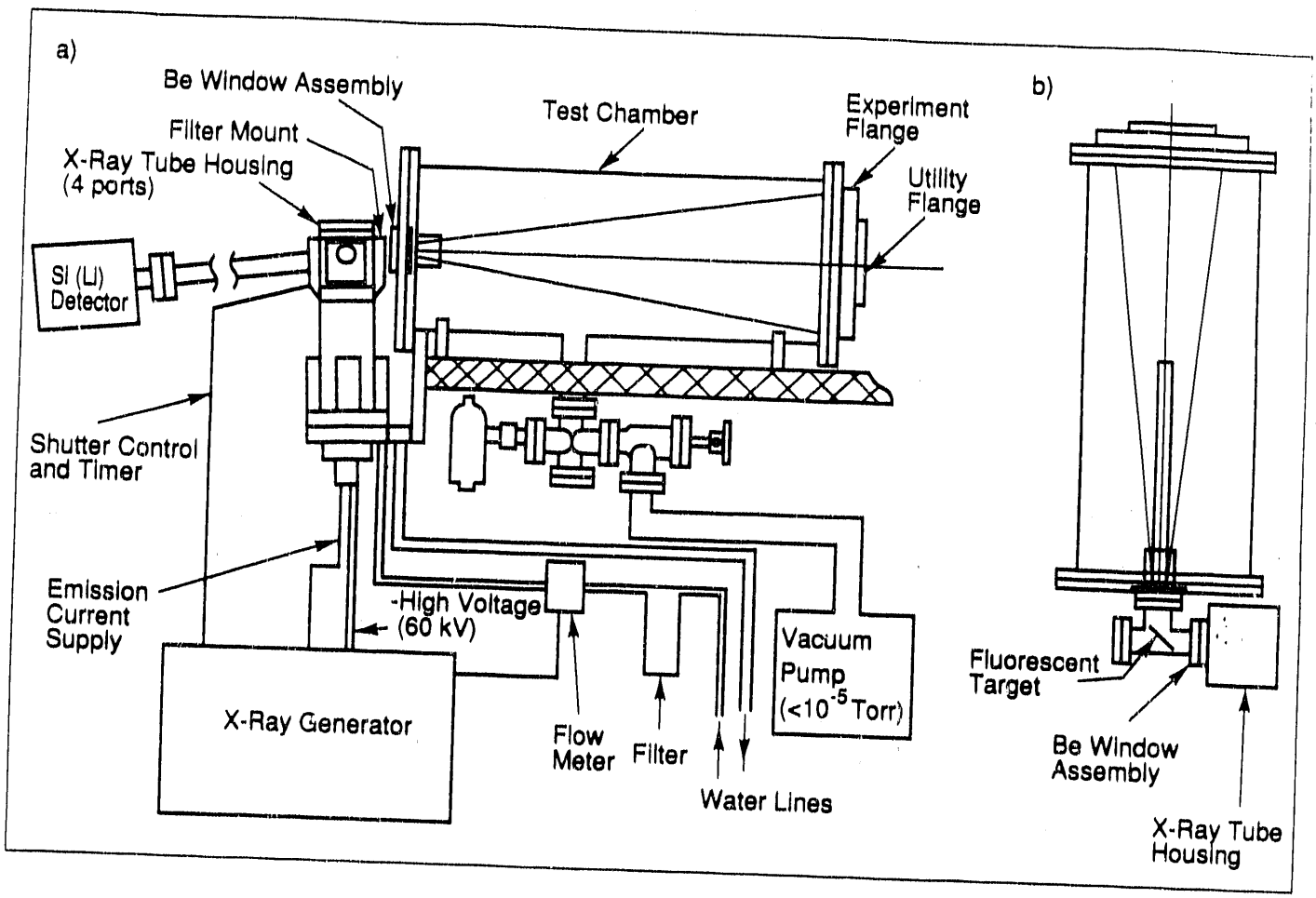

Fig. 2-6. **Details of the high energy test stand designed for calibration and alignment of the Aurora instrument package. With fluorescence excitation x-ray energies of 0.5 to 60 keV are available for calibration purposes. The Aurora reentrant assembly mounts on the 6-in. test chamber port: (a) direct excitation; (b) fluorescence excitation.**

For more information, please contact Anthony Burek

2.1.2 High Energy X-ray Continuum Spectrograph for Nova

A high energy x-ray continuum spectrograph is being designed for inertial confinement fusion diagnostics for Nova. This spectrograph has similar requirements to those for the Aurora spectrograph but with several differences. The energy range for the Nova spectrograph is smaller than the energy range for the Aurora spectrograph, film can be used as a detector, separate high energy channels are not required, and the mechanical constraints imposed by the space requirements are less severe.

The energy range required for the Nova spectrograph is 5 to 25 keV. However, a smaller energy range of 7 to 20 keV would be acceptable if this energy range is covered with a single crystal. The energy resolution $E/\Delta E$ should be no smaller than 10. Although film registration is planned initially, eventual use of a streak camera is planned. Lawrence Livermore National Laboratory (LLNL) wants to reserve the option of detector choice and will supply the detector. KMS Fusion is to supply the diffracting crystal and mechanical assembly.

The mechanical constraints are that the package fit within a 6-in. i.d. tube and mate to a general purpose experiment flange that is guided along alignment rails (the spectrograph interface mechanism [SIM] cart). Confinement within the experiment cone defined by the source and port flange is not as critical as accommodation of the instrument package to the SIM cart within the 6-in. i.d. tube. The continuum spectrograph is the only instrument planned for this port. Space requirements are therefore more tolerant than for the Aurora package, which must also include room for two high energy channels. The total volume available to both experiment packages is about the same.

Lawrence Livermore National Laboratory found several features that are unique to the Laue transmission geometry, particularly attractive in this application, and encouraged us to pursue a Laue design. The main features that make the Laue geometry attractive for a high energy continuum spectrograph are:

- It is a focusing design. The point of zero dispersion is real as opposed to virtual as in the de Broglie geometry, making it possible to obtain arbitrarily small values of dispersion on either side of the focal point. This is particularly important when the signal is weak; only low energy resolution is required and high flux per unit area at the detector is critical.
- Grazing angles of incidence at high energies are avoided because small angles of incidence to the crystal planes are close to normal incidence to the crystal surface. This permits the use of shorter crystals to cover the Bragg angles needed for a given energy range. Placement of stops to avoid shine through at small Bragg angles is not critical.

- **Because it is a focusing design, a scatter slit placed at the focus is very effective in reducing background.**

A number of designs using available crystals have been considered and are being reviewed by LLNL to determine their compatibility with Nova's mechanical constraints. Two such designs using flat crystal and curved crystal geometries that are compatible with the SIM cart mechanism are shown in Fig. 2-7 and in isometric projection in Fig. 2-8. These designs are based on a dispersion such that 300 μm on the detector at the lowest resolution point corresponds to an energy resolution $E/\Delta E$ of 10.

The major components of a Laue transmission spectrograph using a flat crystal design are shown in Fig. 2-9, along with the relevant details of the SIM mechanism and experiment mounting flange to show overall compatibility with the Nova alignment system. It is interesting to note that a similar design using a single crystal to cover the larger energy range of 5 to 35 keV does not fit inside the Aurora experiment cone, even if the high energy channels are removed. The primary reason is that compatibility with the experiment cone is less important for Nova than the requirement that the instrument fit within the 6-in. experiment tube.

A flat crystal geometry provides the most desirable configuration since it simplifies considerably the mechanical design, alignment, and calibration. It is necessary to consider curved crystal geometries only because the 2d spacings of those crystals that are efficient in Laue transmission in this energy region are too short to allow full energy coverage using a single flat crystal.

PET is useful in this energy range because it has a large structure factor, has low-Z components so that fluorescence is not a problem, and has very low absorption so that efficiency in transmission is high at energies less than 10 keV for reasonable crystal thicknesses. Large PET crystals are readily available, and crystals of the required size and thickness can be easily prepared. PET 020 has been used successfully in transmission for film registration of laser produced x-rays for energies as low as 5 keV. The 020 planes have the second largest structure factor in PET and have a fairly large 2d spacing. The planes in PET with the largest 2d spacing and the largest structure factor, the 002 planes ($2d = 8.75$ Å), are not readily available for thin Laue transmission plates because of the cleavage properties of PET.

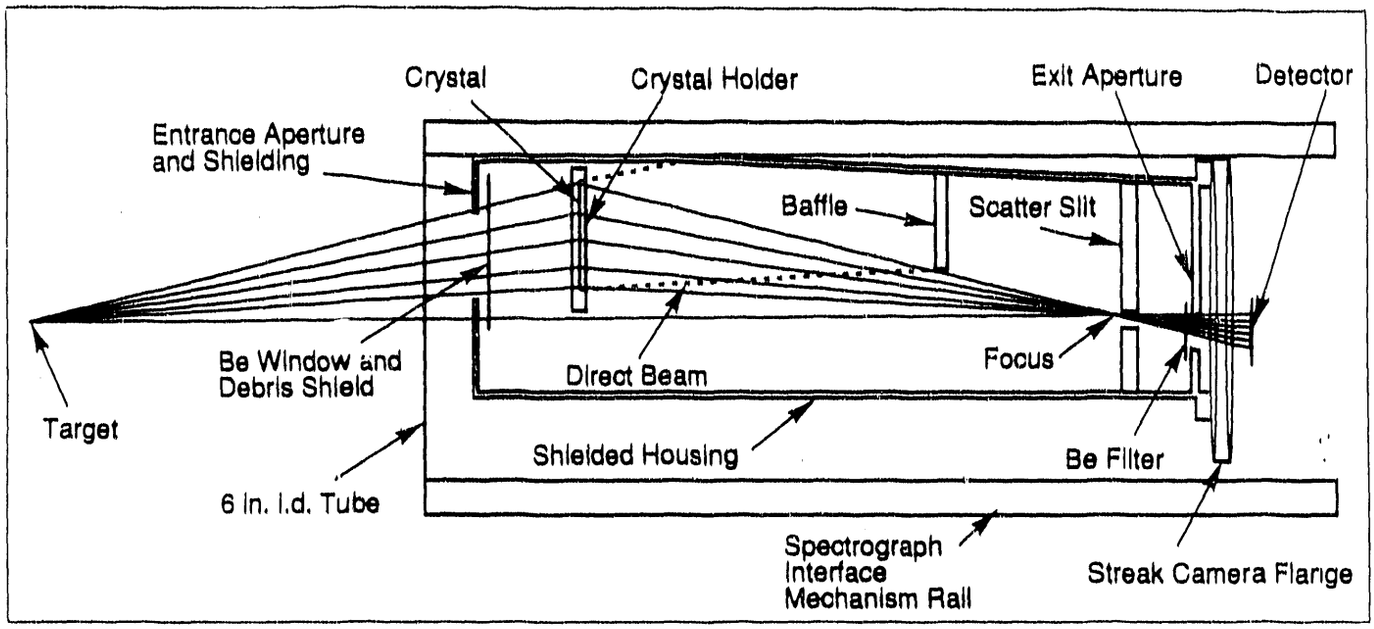

Fig. 2-7. Curved and flat crystal Laue geometries shown relative to the LLNL SIM cart. Curving the crystal shortens the instrument length, increases the spectral coverage, but decreases the spectrograph efficiency.

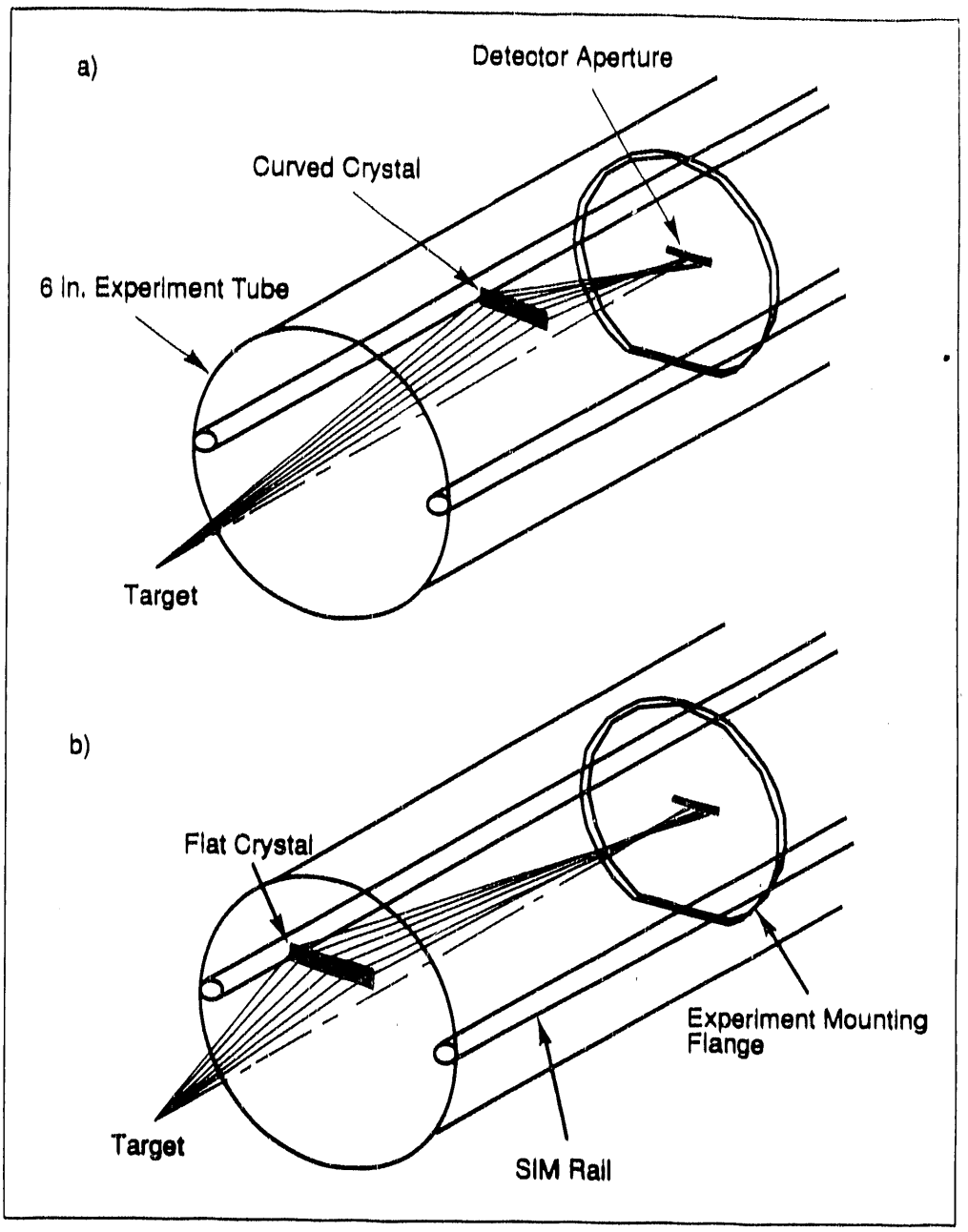

Fig. 2-8. Isometric view showing the placement of the crystal and major rays for the SIM mechanism for the flat and curved crystal Laue geometries: (a) PET (020) curved crystal; (b) PET (020) or EddT (020) flat crystal.

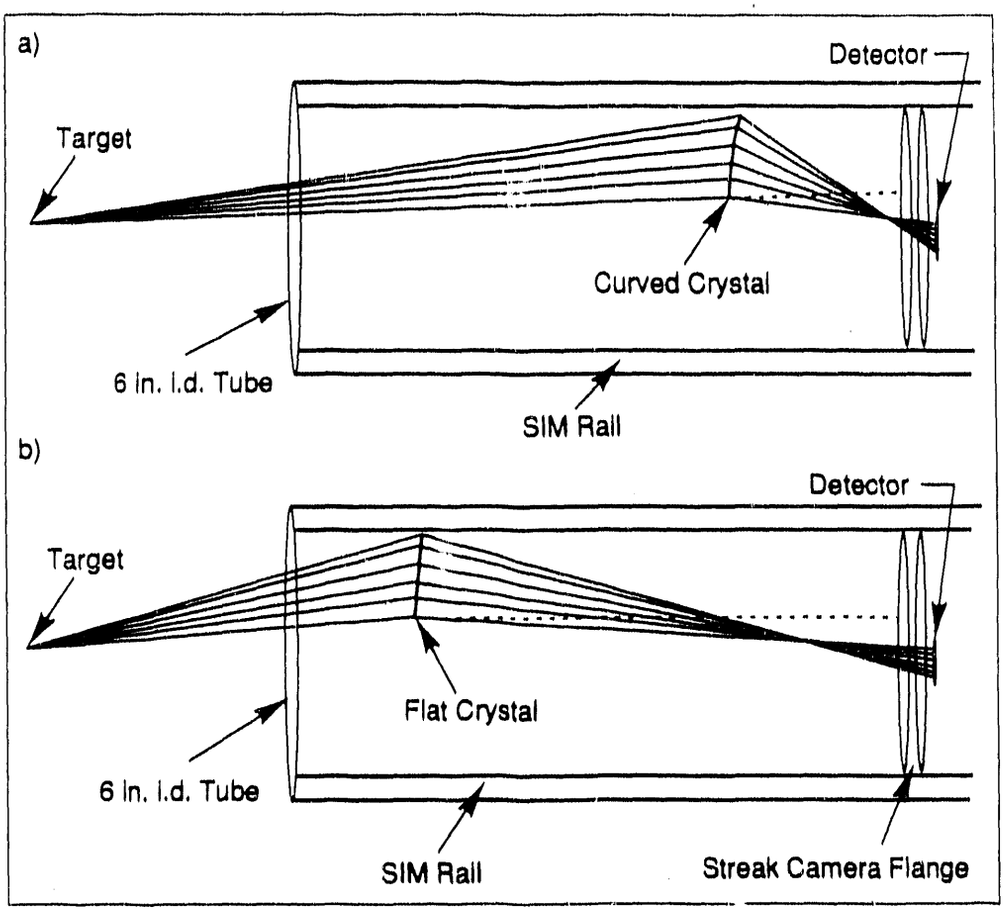

Fig. 2-9. Schematic drawing showing the major components of a flat crystal Laue transmission spectrograph in relation to the LLNL SIM cart and target: (a) PET (020) curved crystal; (b) PET (020) or Eddt (020) flat crystal.

Because of the limited solid angle available in the target chamber for this experiment, it is difficult to cover the entire energy range required with a single flat PET 020 crystal. This is because PET 020 has a relatively short 2d of 6.08 Å. The energy range can be increased by using a convex curved crystal in transmission. Although this makes the instrument more compact, it also decreases the overall sensitivity.

A candidate for larger grating spacing having those attributes that make PET 020 useful in this energy range is EddT 020. This has a 2d spacing of 8.808 Å and will cover the 5 to 25 keV range with the given space constraints in a flat crystal configuration. Like PET, EddT is composed of low-Z elements, has equally low absorption, and has a large structure factor.
The 020 planes are normally used in surface Bragg reflection and very large crystals are easily grown. The crystal does not cleave and it should be possible to grind a plate to the required thickness having the 020 planes oriented for Laue reflection.

Calculations for the mosaic integrated reflectivity for PET 020 and EddT 020 for different thicknesses as a function of energy are shown in Fig. 2-10. These calculations suggest that an EddT 020 plate having a thickness of 0.5 to 0.75 mm would have an integrated reflectivity 3 to 10 times the value of 5×10^{-5} used as a lower limit for useful sensitivity in the 5 to 25 keV energy range for the continuum intensities expected at Nova. The reflectivity of EddT 020 in transmission is expected to be two to four times that of PET 020 simply on the basis of relative structure factor and absorption. Although the theoretical curves indicate increasing reflectivity with crystal thickness at higher energies, one would not like to make the crystal thicker than about 0.75 mm because increasing the thickness degrades energy resolution. With thicker crystals there is also greater difficulty producing the required dislocation density in bulk necessary to approach the mosaic limits to integrated reflectivity.

In referring to these calculations it must be remembered that they give only upper limits because no crystal is ideally mosaic. The actual integrated reflectivity of a mosaic crystal depends on how it is prepared. It might be safe to assume that a real mosaic crystal will have an integrated reflectivity 20 to 50% of the theoretical mosaic value.

We have ordered an EddT crystal cut for Laue transmission from the 020 planes for testing and prototyping. Although EddT is commonly used for Bragg reflection, its use in Laue transmission in this energy region would be novel.

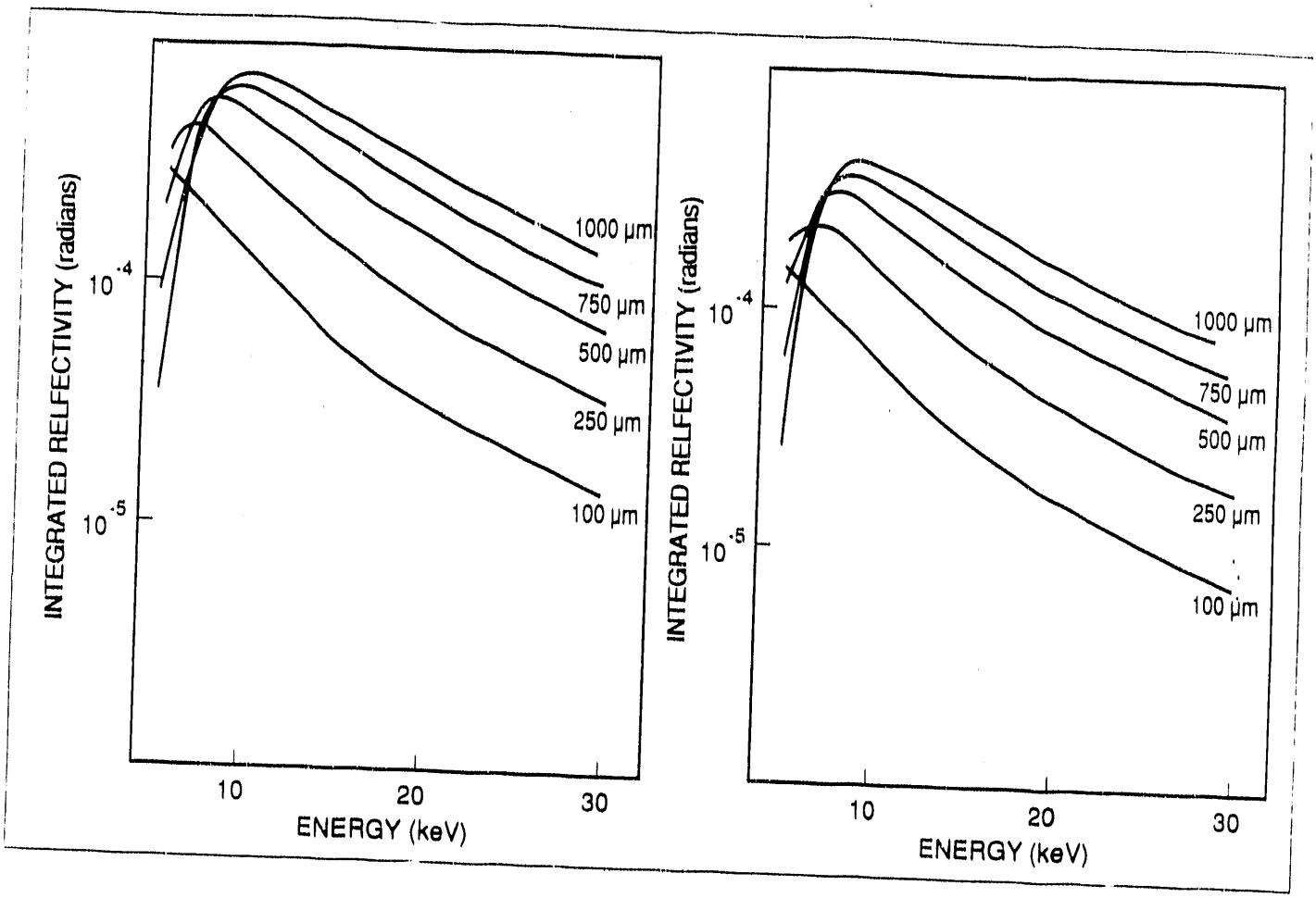

Fig. 2-10. Mosaic integrated reflectivity calculations for (a) EddT (020) and (b) PET (020) as a function of crystal thickness and x-ray energy. The individual curves are labeled with crystal thickness in microns. Since no crystal is ideally mosaic, these calculations are only a guide to the relative efficiency. An integrated reflectivity of 5×10^{-5} for the required energy range is considered a useful lower limit for the continuum intensities expected at Nova.

For more information, please contact Anthony Burek

2.2 Los Alamos National Laboratory Probe Beam Design

The development of an optical probe for the Aurora laser at Los Alamos National Laboratory (LANL) has begun with engineering design work for an f/10 Schlieren system with probe wavelength of 266 nm. The task is divided into three areas:

1) Probe Laser Set-up. A JK Nd:YAG laser has been transported from Alameda, CA, to KMS Fusion (KMSF), Ann Arbor, MI, and assembled. Maintenance and field service has been performed by a Lumonics representative; additional repairs are required to achieve single pulse operation. When the JK laser performance is adequate, timing modifications will be implemented and a frequency-quadrupling crystal installed. The laser will be available for use in the development and test of the Schlieren optical system at KMS Fusion. Subsequently, the JK laser will be transferred and installed at LANL.

2) Probe Timing. Synchronization of the JK laser with Aurora requires a major effort. The JK laser requires ~ 1 μs to produce a mode-locked single pulse, which is longer than would be possible if the JK laser was triggered from the Aurora laser pulse. Consequently, it is necessary for the Aurora computer to initiate the JK laser electronics and oscillator, which subsequently sends a synchronized signal to trigger Aurora.

Figure 2-11 shows a schematic of the proposed system. Interface electronics designed and fabricated at KMS Fusion are triggered by the Aurora computer. The interface electronics control the JK laser timing, trigger Aurora, and also give timing signals that can be used for other applications. A bypass of the JK laser electronics is also included to allow operation of Aurora when the optical probe is *not* in operation, and vice versa.

3) Schlieren Optics. The planned Schlieren optical system is shown in Fig. 2-12. The system has a 3 mm field of view with 10x magnification. The initial phase of development is the design and construction of the multibounce filter to separate plasma-generated light from the collected probe signal. Once this is completed, test of the filter will be performed. The Schlieren optics will be tested at KMSF using the JK laser. Subsequently, the JK laser and Schlieren optical system will be transferred to Aurora and installed. At this point, a test and optimization of the system will be performed to obtain Schlieren images of target shots at LANL.

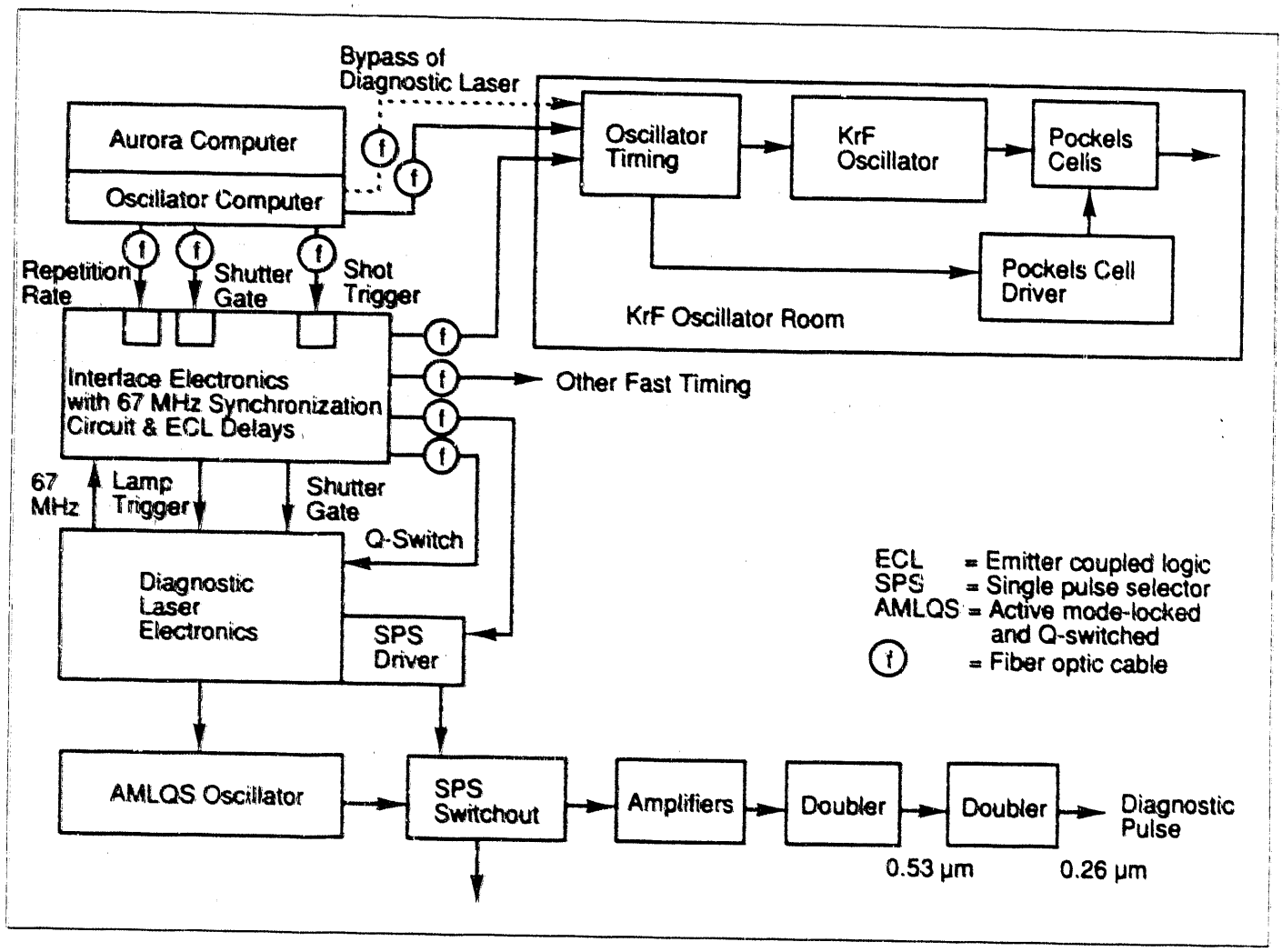

Fig. 2-11. Timing interface design for JK laser at Aurora.

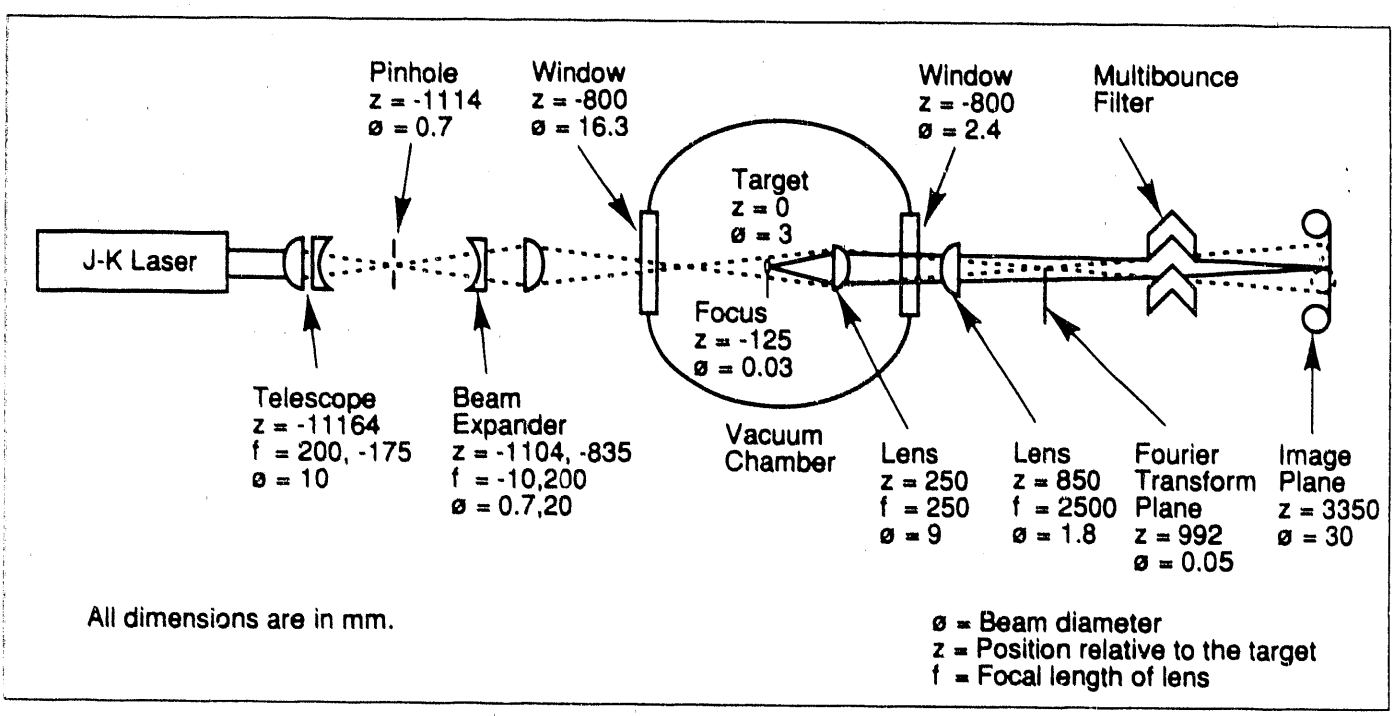

Fig. 2-12. Optical design for Aurora Schlieren photography system.

For more information, please contact Robert Bosch

2.3 Interpenetrating Plasma Experiment

Recent theoretical work[1] has shown that plasmas that collide at high velocity in relatively low density plasma interpenetrate because collisional mean free paths for slowing down due to electron-ion and ion-ion mean free paths are comparable to or larger than the density and velocity scale lengths. Specifically, the systems of interest have electron temperatures, T_e, in the range between 500 eV and 5 keV, ion streaming velocities, U, between 2×10^7 cm/s and 2×10^8 cm/s, electron densities, n_e, between 10^{19} and 10^{22} cm^{-3} and charge states, Z, between 3 and 50. The treatment of this phenomenon, although possibly quite important to the accurate modeling and design of experiments, is not trivial for hydrodynamic simulations even in one dimension. Thus, it is of vital interest to provide experimental tests of interpenetration with relevant plasma parameters.

The standard set of underdense plasma diagnostics do not measure the ion density or ion current density but measure electron density and possibly electron temperature. Measurements of line radiation, if time and space resolved, can provide information about the ion density by charge state and species. The primary difficulties here are signal size and interpretation. For high-Z plasmas, the relationship of the line radiation to plasma parameters is a difficult active area of research and is not understood well enough to yield a reliable measurement. On the other hand, low-Z plasmas will have little line radiation if the electron temperature is too high and the atoms are completely ionized. Thus one is led to consider the collision of two low-Z plasmas at moderate electron temperature, viz, Al and Mg plasmas irradiated with a laser intensity low enough that the electron temperature is between 600 eV and 1 keV. At these temperatures, the ions are most likely bare, hydrogen-like (H-like) or helium-like (He-like), that is, ions with none, one, or two electrons with most of the electrons in the ground state. The strongest emission will be in the Lyman alpha (Ly^{α}) and helium alpha (He^{α}) lines (transitions from the first excited state to the ground state from H-like and He-like ions, respectively) which for Al are at energies of 1.73 and 1.60 keV, respectively.

Description of Experiment.

The target, shown schematically in Fig. 2-13, consists of a Mg slab and an Al dot on a parylene substrate facing each other and separated nominally by 400 μm. Magnesium and Al components were nominally 300 μm square. The targets are mounted on Al wires which, on some shots, were coated with parylene to reduce unwanted line emission from the stalks. The Al dots were typically 125 mm in diameter and both Mg and Al plasmas were created with laser

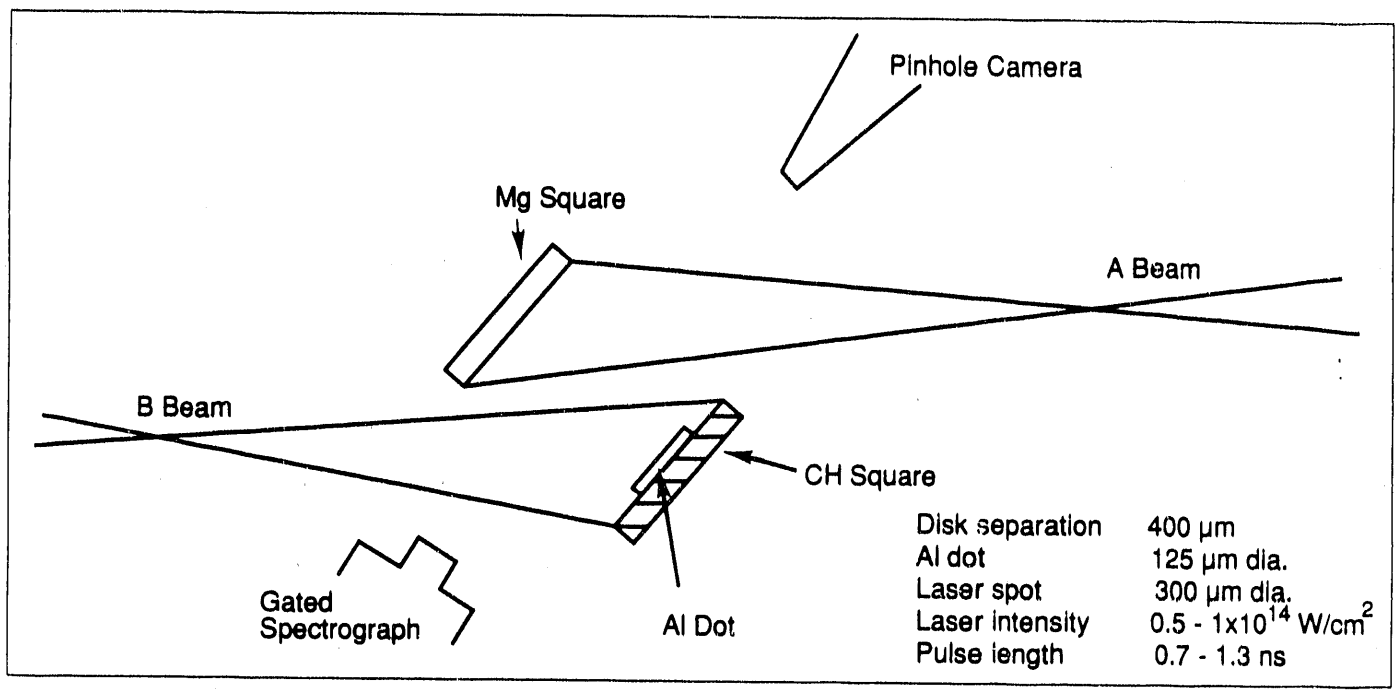

Fig. 2-13. **Schematic diagram of the experiment shows a target consisting of two opposed disks made of Mg and Al on a CH substrate. Also shown are two laser beams (A beam and B beam) striking each target; an x-radiation pinhole camera and a gated spectrometer with an imaging slit. Not shown are another pinhole camera and the holographic probe that are in the plane othogonal to this diagram.**

beams of pulse lengths between 700 ps and 1300 ps and total energy per beam between 50 J and 100 J. The laser spot at the target surface was approximately circular with spot size of 300 μm and an angle of incidence to the target surface normal of 50°.

The experimental setup, also shown schematically in Fig. 2-13, shows two laser beams (A and B beams) striking the inside surfaces of the opposing disks. The x-radiation emitted parallel to the target surfaces is monitored by time integrating pinhole cameras and time, wavelength, and space resolving framing cameras. In addition, holography was used to obtain interferograms that allowed separate measurements of the electron density and target alignment. The framing camera has four images with 100 ps integration time separated by 200 ps. The first frame was adjusted to start typically within 200 ps of the arrival of A and B beams or 600 ps later. This variation allowed measurement of emission for weakly collisional or strongly collisional plasmas. The wavelength resolution was provided by using a highly dispersive ADP crystal with a reflectivity at 1.49 keV of 5.5 x 10^{-5} rad. The holographic probe beam was independently timed and provided up to four images per shot. The probe duration was 20 ps and the separation in time between images was 200 ps. Provision was also made for a backlighter target and beam to measure absorption lines, but no shots were made with this diagnostic in operation.

Description of Experimental Results. Two-dimensional, spatially-resolved time integrated images of x-radiation filtered with Be were taken on all shots. Examples of an image for a target illuminated on both sides and on only the Al side are shown in Fig. 2-14a and 2-14b, respectively. In the one-sided illumination shot, the size of the Al emission region increases with distance from the Al target surface. There is measurable emission in Fig. 2-14b from a spot of diameter 150 μm near the Al target and from a spot of diameter 400 μm near the Al target and from a spot of diameter 400 μm near the Mg target. However, the full width at half maximum (FWHM) of the emission is about 140 mm and varies very little between 50 μm and 200 μm, as is shown in Fig. 2-14c by the dotted lines. For the two-sided illumination shown in Fig. 2-14a, the FWHM of the emission increases in the target midplane region to about 200 μm from the 125 μm size near the target surface. This variation is shown in Fig. 2-14c by the solid line. These images unfortunately are most likely dominated by emission late in time, perhaps even long (1 to 2 ns) after the laser pulse is ended because line emission from recombination is observed to persist. However, these images do provide useful limits to the source size for our interpretation by Ly^{α} line widths.

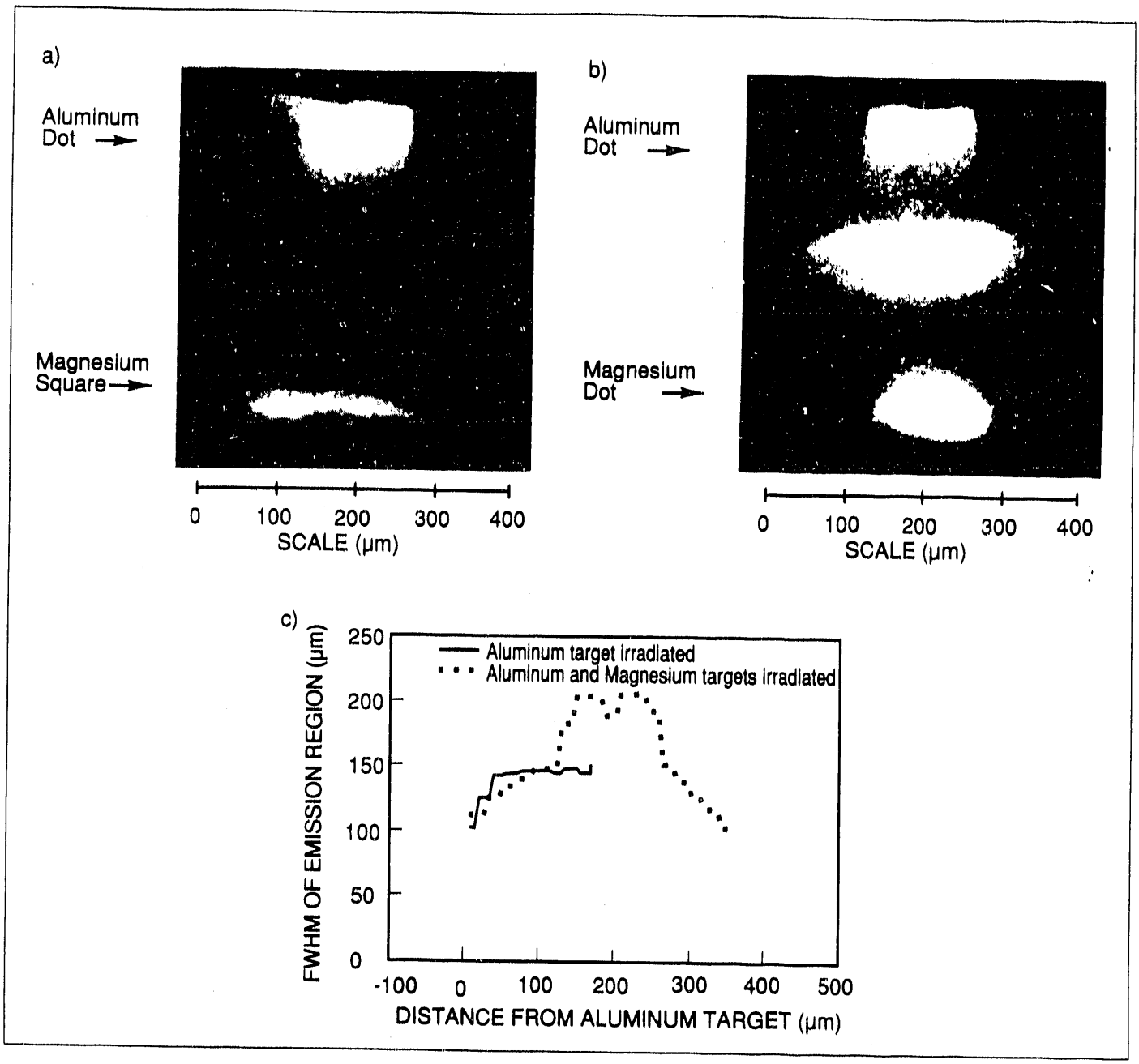

Fig. 2-14. Pinhole images (time integrated) of the x-radiation from an Al dot on a CH substrate and a Mg slab a) illuminated on both sides, b) illuminated on the Al side only, and c) the FWHM of the Al emission in (a) and (b) as a function of distance from the Al target surface.

Space and wavelength resolved images were obtained on a large number of shots with the framing camera. Near the target surface both α and/or β lines of Al (or Mg) are clearly visible in the energy range between 1.5 keV and 1.8 keV because the density temperature product is largest, the number of H-, He-, and Li-like ions is high; and the collisional excitation of the upper levels is highest. Examples of space and energy resolved images are shown in Fig. 2-15. The position of the target inside surface is identified by the continuum emission that forms a line in energy at a fixed spatial position. The x-ray energy increases from 1.5 to 1.8 keV and the Al target is on the top. In all frames shown in Fig. 2-15, the amount of He_α and Ly_α emission can be used to deduce an electron temperature from the ratio of the intensity and reasonable assumptions about the electron density. Farther from the target surface but particularly beyond the target midplane, the Hea emission is particularly weak and this ratio can have large uncertainty.

The Ly_α emission also drops in intensity with distance from the Al surface as one expects for the typical exponential decrease of the ion density for a given species. For our detector, there is a minimum signal that can be observed that depends on the number of H-like Al ions. For our initial spot size of 125 μm, this minimum signal is observed to correspond roughly to $10^{19}/cm^3$ (by comparison to electron density deduced from holography). The total energy radiated (in arbitrary units) in the time interval the framing camera samples can be obtained by integrating the line intensity over the line width. For colliding plasmas, this line energy for Al Ly_α decreases at a less than exponential rate from the Al surface and disappears at some distance near or beyond the midplane. This variation for four different times is shown in Fig. 2-16 for both a one-sided illumination (Fig. 2-16a) and a two-sided illumination (Fig. 2-16b) shot. The increase in Ly_α in Fig. 2-16b over what is measured in Fig. 2-16a is consistent with an increase in electron temperature near the midplane. Such an increase would also increase the ratio of H-like to He-like ions as is typically observed. Moreover, the one-sided shot showed a faster than exponential drop of Ly_α emission with distance, which possibly indicates a decrease of electron temperature with distance.

The apparent spectral width of the Ly_α line of Al can also be measured as a function of distance from the target surface. This width is influenced by the size of the emitting region, the Doppler width caused by the random motion of the different ion emitters, the probably small natural line width, and the line opacity. The size of the Al dot was chosen to keep the plasma parameters within the source region constant (in the unresolved spatial direction) and to minimize source size effects. At these densities, line opacity is estimated not to be important.

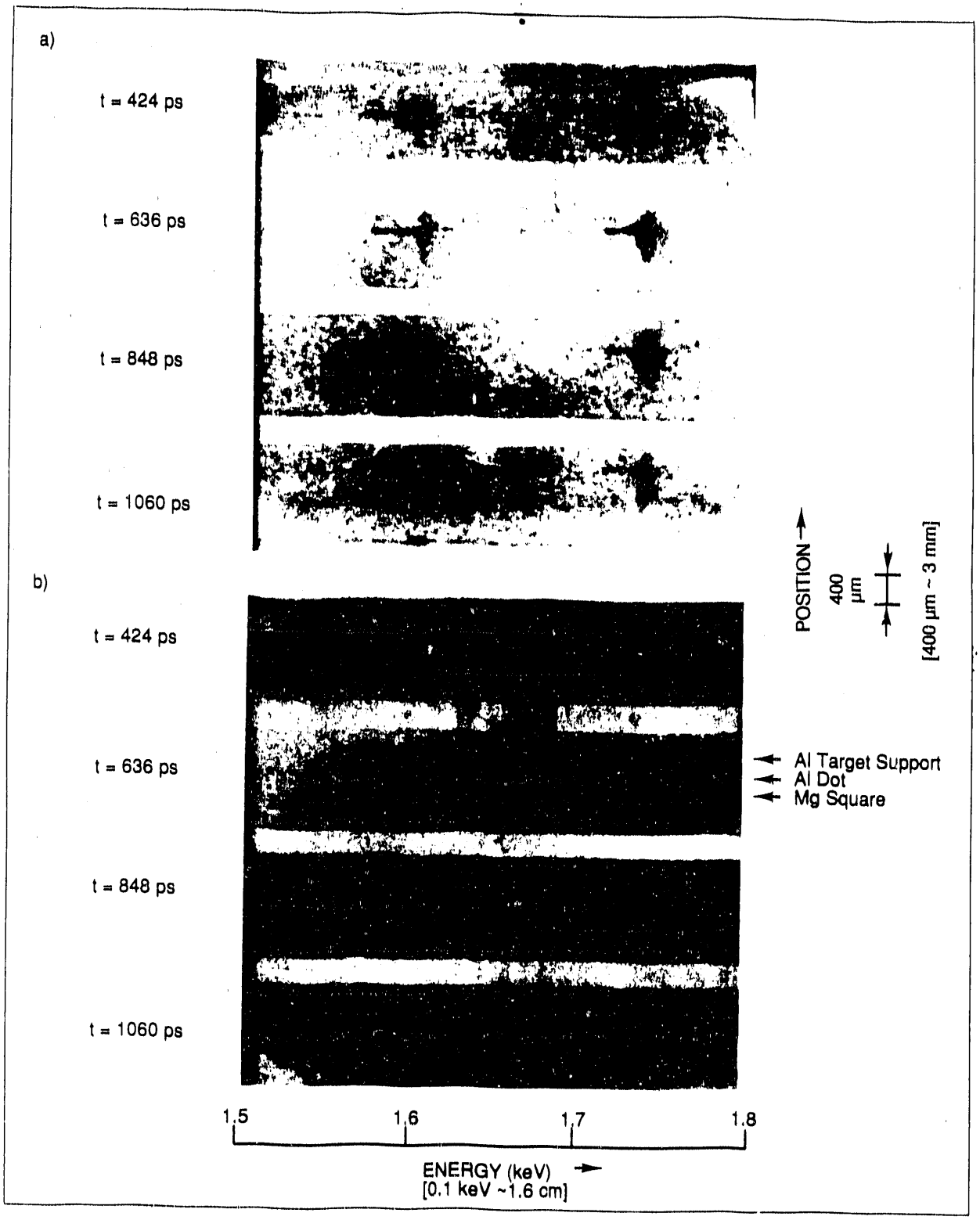

Fig. 2-15. Space and energy resolved images of the x-ray emission. Energy increases from 1.5 to 1.8 keV. The Al target is at the top in each image. The top set of four images is from a shot with only the Al side illuminated. The bottom set was illuminated on both sides. Times at which the images were taken are indicated on the left.

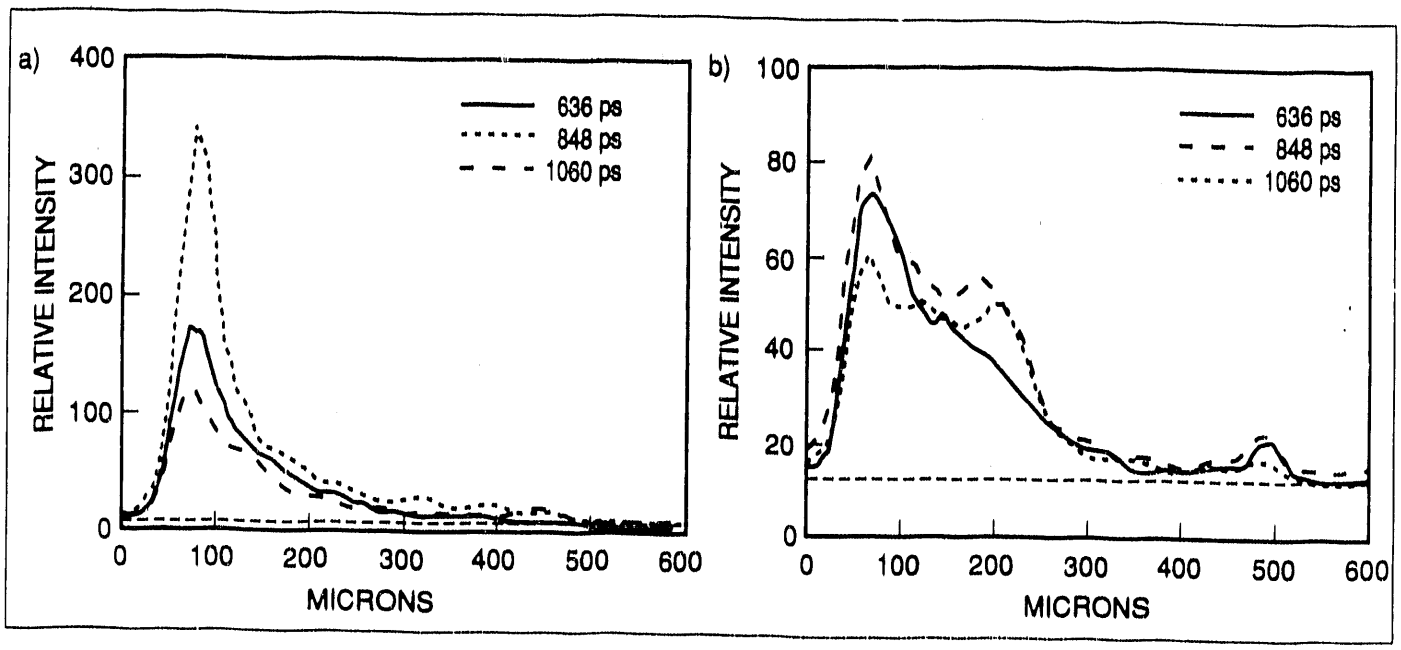

Fig. 2-16. The total energy in Ly_α emission as a function of distance from the Al target at three different times as labeled for a) a shot where only the Al side was illuminated and b) a shot with both sides illuminated. The background (fog) level is indicated by the dashed lines.

In Fig. 2-15b, the Ly$_\alpha$ line looks wider and more intense in the last visible emission before the line disappears in frames at t = 848 ps and 1060 ps. This width increase may be either Doppler broadening or source broadening. As mentioned above, the source broadening can be estimated from the pinhole images shown in Fig. 2-14. In the next section, we give estimates of each effect and our interpretation.

The holographic images were often of poor quality, especially late in the pulse, which we expect is related to the increase in the radial extent of the plasma with time and possibly turbulence associated with the plasma instabilities driven by the counterstreaming flows. Nonetheless, the images were valuable in two respects: 1) the position of the laser spot on each disk could be seen, and a rough measure of energy balance could be obtained from the number of fringes on each side; 2) on those shots with clear fringe patterns, the electron density at important positions could be obtained. The time-integrated, x-radiation pinhole images were also valuable in selecting shots where the laser spots were in diametrically opposed positions on the two disks. On some shots, these two diagnostics showed the Al plasma missed the center of the expansion of the Mg plasma. In the wavelength resolved framing camera pictures, such misaligned shots sometimes recorded spectra with Doppler shifts associated with plasma flow toward or away from the camera.

The electron density for a particular shot and its interferogram are shown in Fig. 2-17. The electron density as a function of radial distance along the target surface (Z is the axis between the disks and r is centered at the middle of the disk) at three different times is shown in Fig. 2-17b. The decrease with radial distance is roughly gaussian away from the peak value on axis of nearly 7 x 10^{20} cm^{-3} at 1 ns. Very little resolution of the density on axis is obtained.

Interpretation and Conclusions. At this time, the data analysis is incomplete. Thus, our conclusions, tentative and somewhat speculative, are as follows. The plasmas reach a coronal electron temperature of ~800 eV close to the target surface (within 100 μm) within 400 ps of the start of the laser pulse. Because of the collisional heating of the electrons as the ions slow down due to ion-ion and electron-ion collisions, the electron temperature near the midplane increases causing a further ionization of He- and H-like ions. In general, this process causes an increase in Ly$_\alpha$ emission compared to what one expects from expansion into a vacuum where the electron temperatures would decrease somewhat with distance. The Ly$_\alpha$ emission early in the pulse (less than 300 ps) is consistent with complete interpenetration, but quantitative verification suffers from the lack of signal sensitivity of the framing camera if the ion density falls below 10^{19} cm^{-3}. Later in the plasma evolution (greater than 800 ps) the

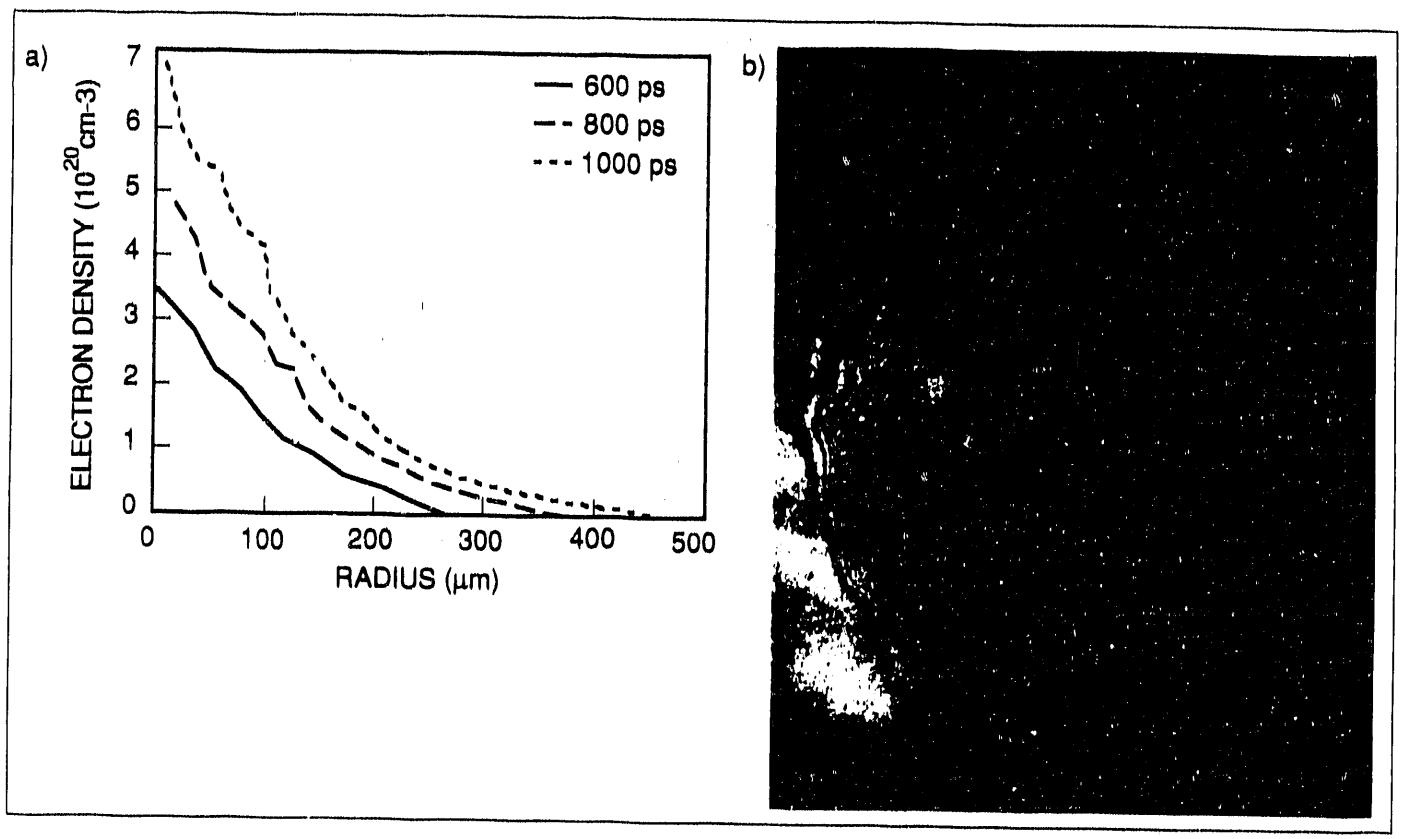

Fig. 2-17. Shown are the electron density a) versus radius at the target midplane at three times as labeled, and b) one frame of three holographic images from which the density was deduced.

interpenetration stops well before the Al plasma reaches the solid density Mg plasma. Evidence for this statement is the strong emission of Ly$_\alpha$ radiation near or just past the midplane that ends abruptly at greater distance. Some evidence also exists for Doppler broadening of the line which is consistent with ion temperatures locally of tens of kilo-electron volts. Such ion temperatures represent only a fraction of the estimated energy available in the ion kinetic energy that must be converted to heat (or radiated) as the plasma stops. Some or all of this increased line width may be source broadening because of radial expansion of the plasma. At the present time, no definite conclusions have been reached.

In this experiment, emitted radiation in the region of interest was about at the detector threshold. The experiment design would be improved if the detector sensitivity could be increased at least an order of magnitude. No reduction in space or time resolution is desirable however. The use of absorption spectroscopy was not attempted due to lack of time but is clearly the next step for any subsequent experiment on this subject. Because collisional heating appears to deplete the He-like ions, Ly$_\alpha$ absorption appears to be the best choice for Al plasmas. The use of this diagnostic with an Al target plasma is limited to sub-keV electron temperatures for which stagnation occurs when electron densities reach 2 to 5 x 10^{20} cm^{-3}. At higher temperatures, the mean free path for stopping will be larger for Al, but higher Z plasmas will be required to have a few bound electrons for diagnostic purposes. Thus the target size and laser parameters need not change more than a factor of two in size and four in energy.

For more information, please contact Richard Berger

2.4 Ionization Balance Experiments

Detailed atomic level populations in high temperature and dense plasmas have become increasingly important in laser generated plasmas. Certain spectral lines are density-dependent while others are temperature-dependent. Both can be used to extract information concerning population kinetics and ion level populations. In order to be useful, these dependencies must be characterized by independent means. In laser produced plasmas, this can be done via holographic interferometry for electron density determination[2] and via the slope of the H-like free-bound continuum of K-shell lines for electron temperature determinations.[3] The characterization of density- and temperature-dependent L-shell lines can be accomplished in ionization balance experiments in which laser irradiance is varied on targets which contain both K-shell and L-shell emitters. The K-shell free-bound continua provide the local

temperature determination while holographic interferometry yields density profile information from which the temperature and density dependent L-shell lines can be characterized.

Ionization balance experiments were performed during the latter half of this reporting period on K-shell and L-shell elements. They constitute refinement of a previous series of ionization balance experiments that were performed in 1987 at KMS Fusion (KMSF).[4] The difference between the two sets of experiments is in the degree of sophistication used in the recording of the time-resolved spectral data. In the earlier 1987 series, two time-resolving instruments were employed: (1) A streak camera fitted with a low spectrally resolving KAP crystal spectrograph was used to record the time-varying x-ray emission at selected regions of the target plasma plume. (2) A stripline/microchannel plate (MCP) framing camera spectrometer, also with a KAP crystal, was used to provide spatially resolved spectra at three different times.

In the present series, three stripline/MCP framing intensified x-ray spectrometers (FIXS) provided by Lawrence Livermore National Laboratory (LLNL) were used to yield simultaneous high, medium, and low resolution spectra of the plasma plume, using ADP, Beryl, and KAP crystals, respectively. Electron density was measured using a 4-frame holographic interferometer. Additional target/plasma diagnostics included two pinhole cameras, one with three filtered stripline/MCPs, yielding 18 timed target images, a spatial- and time-integrating KAP spectrometer, plus the usual energy-on-target and absorbed energy calorimeters, and visible streak cameras for pulse length and shape measurements. Figure 2-18 is an axial view of the placement of the spectrometers in the KMSF target chamber.

Twenty-six target types, listed in Table 2-1, were employed to accommodate the different target element emissions and spectrometer sensitivities. Aluminum, Mg, and Cl, as K-shell emitters, provided information on the electron density and temperature of irradiated targets also containing L-shell emitting spectra of Mo, Br, and Cu. These composite targets were fabricated using powder mix techniques. Previously prepared powders of the specified elements were mixed, melted in a furnace, remelted, etc., until the composite was considered well mixed. The powder mixtures were then tamped into pre-drilled depressions in polystyrene and shaved at the surface to produce spots with diameters of 50 and 100 μm, as shown in Fig. 2-19. Also shown in Fig. 2-19 is a "bull's eye" target made by placing a washer of Mg around the spot to provide added Mg emission for shots in which electron temperature could be more easily determined via the free-bound continuum of H-like Mg.[5]

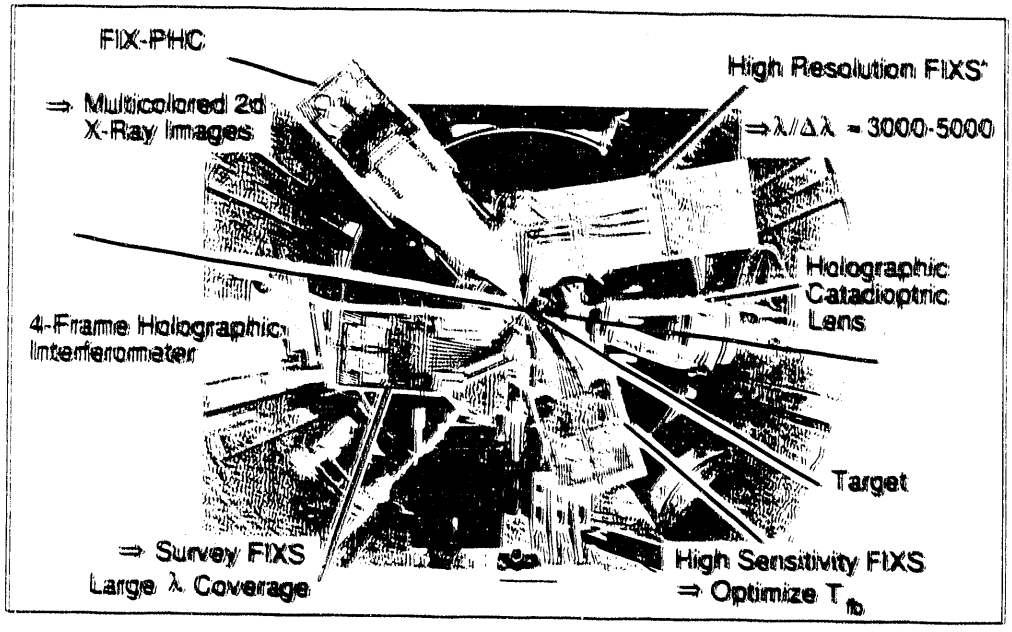

Fig. 2-18. Axial view schematic of target chamber showing the placement of the spectrometers and other plasma diagnostics.

Table 2-1. Twenty-six Composite Target Types were Used to Accommodate Target Element Emissions and Spectrometer Sensitivities.

Target Type	Composition
1. Al slab	1 mm thick
2. Al dot/Lexan™	50 x 50 μm/150 nm Lexan™
3. Al dot/Lexan™	100 x 100 μm/150 nm Lexan™
4. Al dot/Formvar®	5000 Å x 530 μD Al/1000 Å Formvar®
5. Al/Al 2-sided	43 μm x 43 μm Al/5 mil Mylar®/53 μD Al
6. 50μm Al sq.dot	100 nm Al/50 nm Mg/50 nm Si/2 μm Al
7. 50μD Al/Ag	Al on thick Ag
8. Al/Ge	23 nm Al/34 nm Ge
9. Al/NaCl split	70 x 30 μm NaCl top/50 μm Al bottom
10. Layered: Al/NaCl	50 layers: 15 nm Al/5 nm NaCl
11. Fe/Al 2-sided	35 x 25 μm Fe/5 mil Mylar®/50 μD Al
12. Er/Al 2-sided	50 x 25 μm Er/5 mil Mylar®/50 μD Al
13. Mg slab	4.5 x 6 μm x 15 μm Mg
14. Mg dots	70 x 70 μm Mg/5 mil Mylar®
15. Mo/Mg	50 μD x 90 nm Mo/50 μD x 140 nm Mg
16. 10%Mo/30%Mg	MoO_3+MgO in 50 μD
17. 10%Mo/30%Mg "bull's eye"	MoO_3 + MgO in 50 μD + 150 μD Mg
18. 11%Mo/11%Mg	MoO_3 + $MgCO_3$ in 50 μD
19. 2%Mo/10%Mg	MoO_3 + $MgCO_3$ + $NaHCO_3$ in 50 μD
20. 2%Mo/10%Mg "bull's eye"	MoO_3 + $MgCO_3$ + $NaHCO_3$ in 50 μD + 150 μD Mg
21. 8:1 Mg/Mo dot	50 μD 8:1 Mg/Mo on 160 μD Mg
22. 7%Mo/7%P	$Na_4P_2O_7$ + Na_2MoO_4 in 50 μD
23. MgF_2/NaBr	50 μD x 110 nm NaBr/50 μD x 100 μD MgF_2
24. 10%Br/40%Mg	C_6Br_6 + MgO in 50 μD
25. 10%Br/10%Mg	C_6Br_6 + MgO + C in 50 μD
26. Mg/Cu	76 x 78 μm Mg/1 mil Mylar®/53 μD Cu

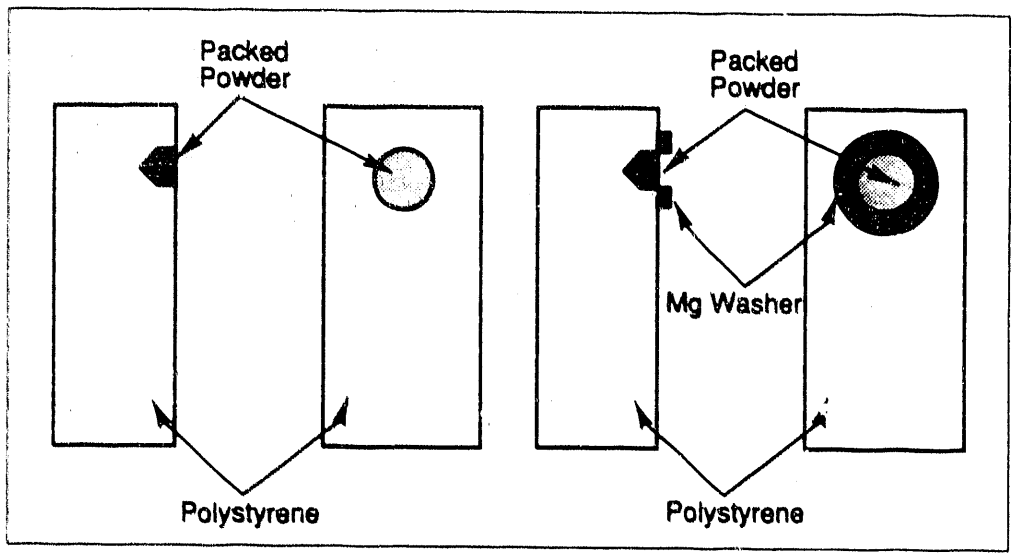

Fig. 2-19. Schematic drawings of powder spot targets and "bull's eye" targets.

A typical L-shell spectrum of Mo is shown in Fig. 2-20, in which F-, Ne-, and Na-like lines of Mo are indicated by F, Ne, and Na labels, respectively. As an example of the use of L-shell lines as a measure of density, the E2 transition indicated by the line labeled X is density sensitive.[6] When compared to the Ne-like line 3A, it can be used as a measure of the plasma electron density, especially under conditions in which interferometric measurements of electron density are not practical.

The ionization balance task was in three parts. Two parts, a series on 20 ps experiments and a series on absorption spectroscopy, were provided in earlier KMSF Annual and Semi-Annual Technical Reports. The third, on L-shell spectroscopy, has resulted in large number of laser/target shots which are presently being analyzed. A summary of shot statistics for all three parts of the ion balance task is shown in Table 2-2.

Table 2-2. Ion Balance Statistics Summary including the Three Parts of this Task

Number	20 ps Experiments	Absorption Spectroscopy	L-Shell Spectroscopy
Target Fabricated	217	75	233
Target Shots	152	64	173
Interferograms	300	- - -	420
Analyzable Spectra (Estimate)	220	40	480

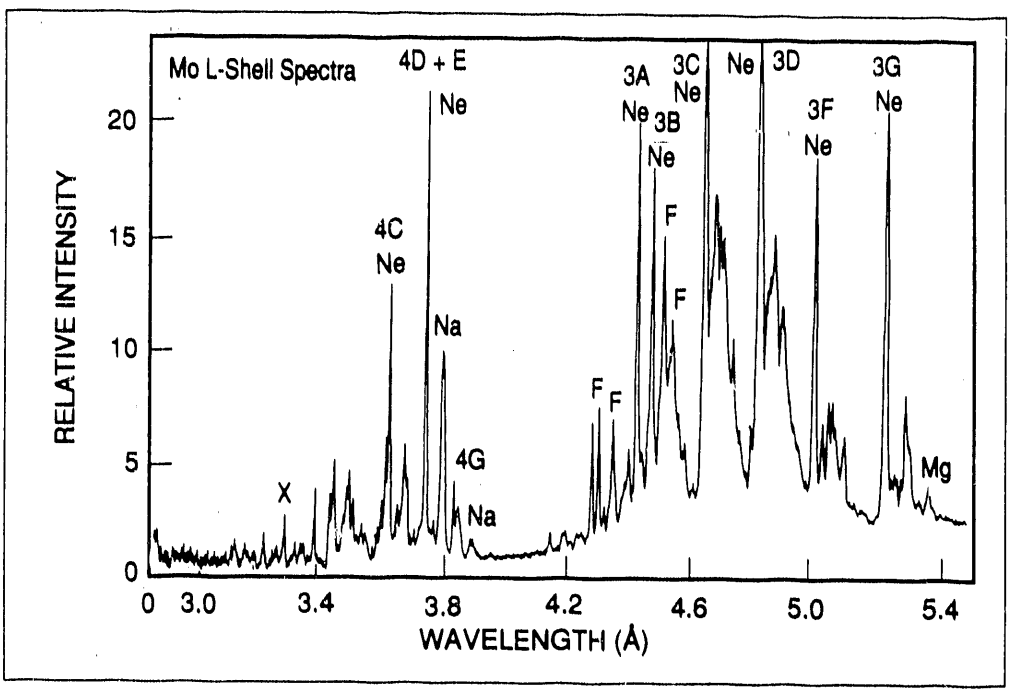

Fig. 2-20. Preliminary lineout of a Mo L-shell spectrum showing the appearance of F-, Ne-, and Na-like lines. An E2 line labeled X can also be used a as a ratio with the Ne-like 3A as a density diagnostic.

For more information, please contact George Charatis

2.5 Radiation Cooling Instability

KMS Fusion (KMSF) experiments during this reporting period have exhibited the curious presence of thin, high density fingers or jets of relatively cold plasma. These "cold jets" appear in experiments with high-Z materials such as gold disks, but only when the laser irradiation is pulsed, typically with lengthy gaps between the laser pulses. The physical mechanism behind the cold jets has long been elusive, but recent theoretical advances strongly suggest that the jets arise from a hydrothermal instability driven by radiative cooling, a process first discussed theoretically within the context of inertial confinement fusion (ICF) by Evans in 1981.[7,8] It now appears that this mechanism may be responsible for some of the jets or "horns" observed elsewhere over the years in laser-target interactions.[9-11] For the ICF program, the effects of the instability have important implications for the temporal shaping of laser pulses used to generate implosions via secondary radiation. Specifically, long gaps in "picket fence" schemes can lead to detrimental asymmetries in wall ablation and radiative uniformity.

The recent KMSF experimental paper "Plasma Jets from Laser-Irradiated Planar Targets" by Gabl et al[12] documents the characteristics of the cold plasma jets observed in KMSF gold disk experiments at laser wavelengths λ_L = 0.53 μm and λ_L = 0.35 μm. In that paper, it was stated that two-dimensional (2-d) hydrodynamic simulations with the KMSF 2-d hydrocode HYRAD were unsuccessful in reproducing the jetting, and that the jets were apparently not purely hydrodynamic in origin. Here we report recent successful hydrocode simulations of the jetting, and the assumptions and conditions required for their appearance. We also describe the implications of the jetting for future ICF work.

The experimental evidence for the cold jets is described in Ref. 12 and 13. Temporally and spatially resolved images of continuous x-ray emission from high-Z irradiated disks (Au, Ti) show jets that are cold, dense, and supersonic. Views along the laser axis clearly show reduced hard x-ray emission (> 1.5 keV), while transverse views show apparent hard x-ray absorption, indicating high density, i.e., the jets are as much as 10 times more dense than the surrounding corona. Curiously, the jets appear to move at the extremely rapid speed of two to four times the local sound speed cs ($cs \sim 4 \times 10^6$ cm sec^{-1} at the estimated jet temperature of < 600 eV), a speed more characteristic of the lower density parts of the outer corona. The most astonishing discovery is the clear correlation of the jet location with the cooler parts of the laser beam (which typically contained numerous small [~20 μm] hot spots). This is very different from normal ablation scaling, in which higher ablation pressures and greater blowoff occur in the areas of higher intensity.

Two additional facts about the cold jets appear to be fundamental to understanding their underlying physics. First, they appear only in multiple pulse laser illumination, typically a "picket fence" arrangement in which a relatively short 100 ps pulse is followed by a lengthy off period (usually 300 to 500 ps). A representative pulse of this type is shown Fig. 2-21a. The emission features previously mentioned are to some extent time averaged features, but the jet appears to form in the period between the first and second picket (Fig. 2-21b). Subsequent illumination with a second picket and a main pulse appears to smooth out the density perturbations (Fig. 2-21c,d). The second important fact is that the jetting only occurs in high-Z materials (e.g., Au and Tl). Similar jets are rarely or never seen in low-Z materials such as plastics or aluminum.

The scaling with Z is consistent with the interpretation that thermal conduction [1/(1+Z)] is the smoothing mechanism which either smooths out existing jets when the laser is on or fails to damp out density perturbations between pickets. The reduced efficiency of heat conduction in high-Z materials is the reason jets or plumes form much more readily at high-Z. After the picket pulse turns off, there is not enough time for conduction to laterally smooth out temperature perturbations. Instead, the thermal energy is either radiated away or quickly converted into kinetic energy of expansion normal to the target surface, thus preserving the imprint of the density perturbations causing the jet phenomenon.

The simplest possible hydrodynamic effect that could cause jet formation would be a pressure gradient created by hot spots. Consider the geometry shown in Fig. 2-22. In converging focus, a hot (higher laser intensity) ring surrounds a cooler central part of the laser beam. This sets up angular pressure gradients in the ablation region upward of critical density, which have the effect of squeezing cooler material out along the central axis, much as one squeezes toothpaste out of a tube. Unfortunately, 2-d HYRAD and LASNEX[14] simulations were unable to produce any such effect with any reasonable high/low intensity ratio (< 10 to 1). The densities typical of the jets (< 0.2 n_c, where $n_c = 4 \times 10^{21}$ electrons cm^{-3} for $\lambda_L = 0.53$ μm) may be too low to be affected by such an ablation pressure effect. In any case, the jets were seen with both converging and diverging focus laser illumination.

The inefficiency of pure hydrodynamics leaves one with an array of pure hydrodynamic, hydromagnetic, and hydrothermal instabilities to consider. A magneto-thermal heat flow instability15 and radiative cooling instability (RCI)[7,8] have also been invoked to explain similar phenomena.12 In the purely hydrodynamic category are the Rayleigh-Taylor (RT) instability and the Richtmeyer-Meshkov (RM) instability in which material boundaries and/or ambient density gradients are set up in such a way that (for RT) a light fluid accelerates a heavier fluid, or (for RM) a shock wave amplifies density ripples between light/heavy fluids. The direction and monotonic nature of the pressure gradient in the coronal plasmas in this report and the lack of material interfaces both indicate that RT and RM are not responsible for the cold jets we are currently trying to explain.

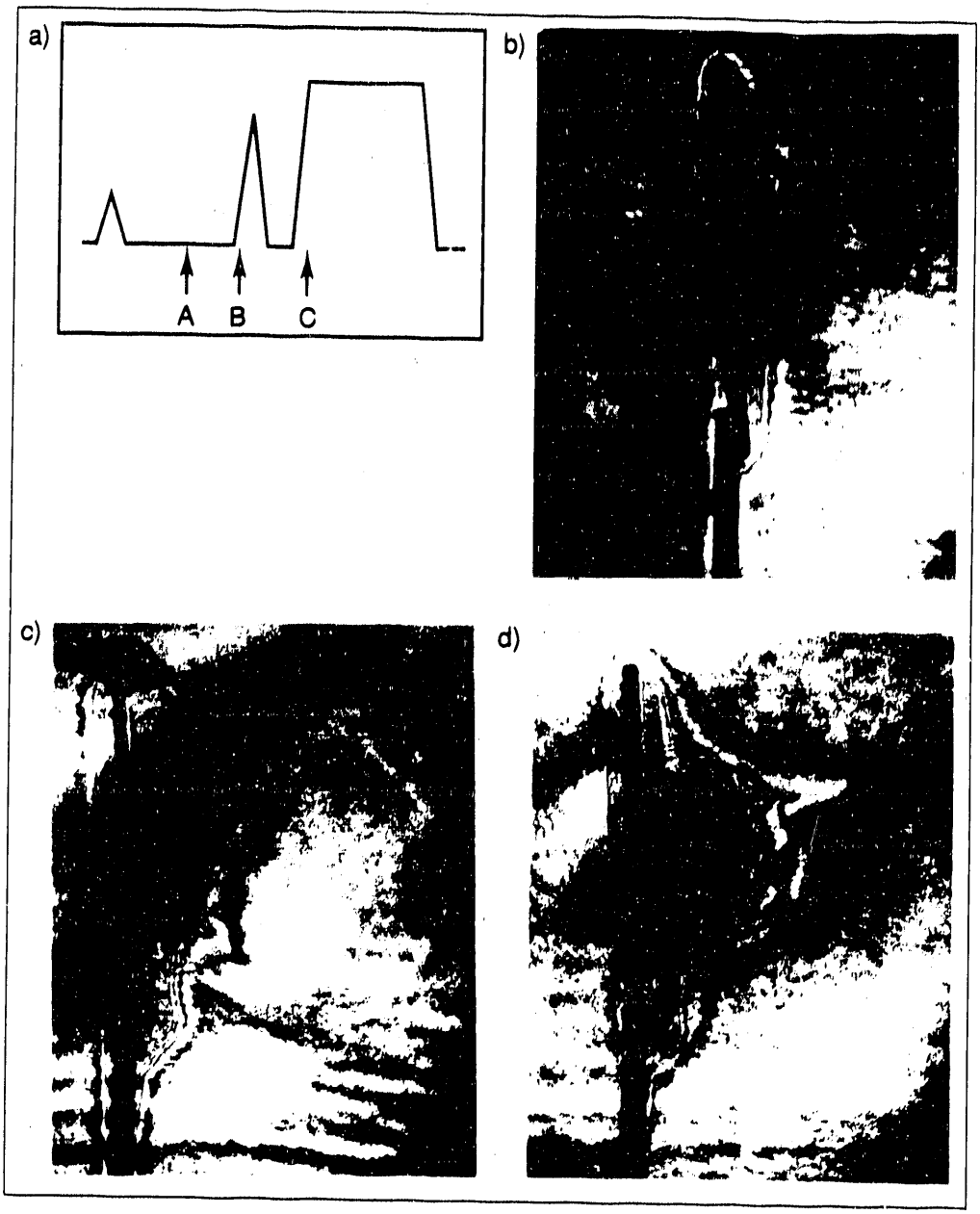

Fig. 2-21. For times indicated by A, B, and C during a picket fence pulse, holographic interferometry shows jets forming, growing, and dissipating.

Magnetic instabilities are driven by temperature and pressure gradients. In more collisionless plasmas (e.g., with CO_2 illumination) huge B fields and currents can be driven. In more collisional plasmas, the Weibel instability, for example, can create jetlike asymmetries.[16] However, the ambient B fields at the intensities (1 to 5 x 10^{14} W/cm^2) of the KMSF experiments discussed here are just too low. A similar objection applies to the magneto-thermal heat flow instability.

This leaves us with just two likely instability candidates for the KMSF cold jets. These are (thermal) filamentation and RCI. Filamentation[17,18] is driven by laser self-focusing, while RCI causes density clumps by rapid, optically thin radiation loss followed by pressure relaxation. Both have sizable growth rates in the intensity region of interest. Although in thermal filamentation the hot (self-focused) parts of the laser beam occupy regions of lower density, there is no reason to expect to see a finger or plume moving outward from regions of higher density. More importantly, there is no way for filamentation jets to grow when the laser is off. It was this line of reasoning that first led us to consider RCI, which we now believe to be responsible for the KMSF cold jets.

Radiative cooling instability is one of a class of thermal instabilities which has found wide application in astrophysical plasmas.[19-21] Basically, one has a plasma in which there are four important timescales: heating, cooling, thermal conduction, and acoustic (hydro). At the densities and temperatures encountered in the KMSF high-Z experiments, strong laser or thermal conduction heating and radiative cooling result in heating/cooling being the shortest timescale, followed by hydro, with thermal conduction as a smoothing agent not being important. The latter requirement fails for short wavelength RCI modes ($\lambda_{RCI} < 10$ μm according to Evans[7]), which will be damped out by conduction.

The instability operates as follows: random density fluctuations result in a slight density increase. If the radiation is a sensitive enough function of density, and if the local plasma is optically thin to the radiation produced, this results in increased radiation loss. This causes two effects. First, if the hydro time is not too long, pressure readjustment of the cooling plasma will cause further condensation, i.e., density increase, which will increase the radiation rate, etc. However, just as importantly, if the plasma cooling rate depends inversely on the temperature to some power in a certain temperature range, then the cooling rate increases even more rapidly, accelerating the formation of a cold jet. Our 2-d HYRAD simulations of the cold jetting indicate that this cooling law is the key to the formation of the picket jets. The cold jets accelerate faster than the hotter part of the corona as if the radiation is a trap door, causing the bottom to drop out of the pressure, and thus creating large accelerating pressure gradients slightly upstream.

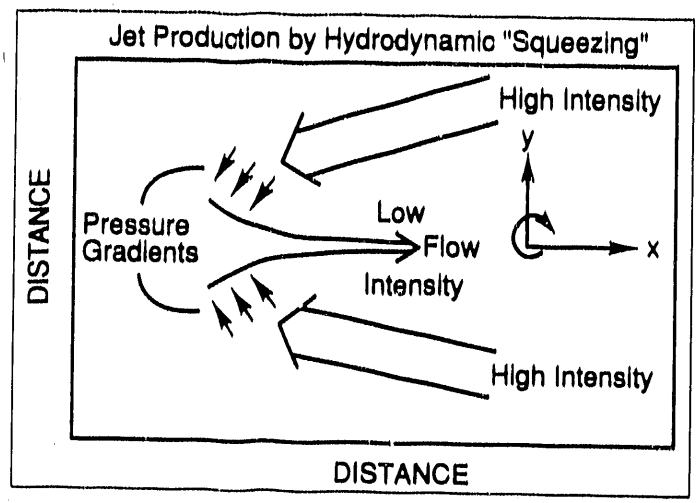

Fig. 2-22. Jet production by pure hydrodynamic "squeezing" under nonuniform laser illumination conditions.

Evans has obtained detailed RCI growth rates under the conditions that the laser is on and the heating and cooling rates balance each other. If the heating rates per unit mass go as $H = \rho^{\alpha}T^{\delta}$ and the cooling rate as $C = \rho^{\gamma}T^{\delta}$, then the RCI growth rates depend on the relative values of α,β,γ and δ. He finds that $(\delta-\beta)-(\gamma-\alpha) < 0$ is typically required, so for inverse bremsstrahlung laser absorption ($\alpha = 1$, $\beta = -1.5$) and free-free or bound-free emission ($\gamma = 1$), one requires $\delta < -1.5$. This is the telltale temperature dependence mentioned in the previous paragraph. It can occur in high-Z materials as a shell filling effect. That is, at slightly too high a temperature, an outer shell may be stripped, so no line emission can occur from that level down; as the temperature drops and recombination occurs, line radiation can increase. Of course, for bound-bound emission $\gamma = 0$, so this is not easy while the laser is on in the corona. If one switches to thermal conduction heating, such as would occur above n_c during the pulse or anywhere after the laser shuts off, growth becomes a little easier. The latter is key for the KMSF jets. Evans also shows that the dispersion relation for the plasma with no heating source has growing modes, which we believe correspond to the cold jets.

Evans simulated RCI numerically in a laser plasma by artificially putting in optically thin radiation losses with the right values of δ. His rates were based on rates calculated for generally less dense ($n_e < 10^{16}$ cm^{-3}) astrophysical plasmas.

What we have done is put in optically thin radiation losses for Au over a temperature range from 200 to 1600 eV and electron densities 10^{20} to 10^{22} cm^{-3}. We wanted to put in a rate which would have reasonable density and temperature dependence for a primary radiation loss mechanism of bound-bound (line) emission from Au. The average-atom equation of state usually used in the HYRAD code was clearly inadequate for this simulation, and indeed contributed heavily to the failure of previous HYRAD and LASNEX simulations from showing the jetting effect. Therefore, we ran a separate non-LTE EOS simulation for Au in this temperature range using the LLNL atomic-physics/radiation package Detailed Configuration Accounting (DCA).[22] Detailed Configuration Accounting calculates the actual multi-ion stage equilibrium, in this case in the hydrogenic approximation. We found that over a significant range the temperature dependence of the (assumed optically thin) emission corresponded to an effective value of $\gamma = -1.85$.

Therefore, we ran a HYRAD simulation similar to that of Evans, using an artificially imposed optically thin radiation loss term with $\delta = -1.85$ on a picket fence pulse with a 100 ps initial pulse, followed by 400 ps of coasting (laser off). For this simulation, the laser pulse was assumed to have a spatial variation corresponding roughly to a high intensity ("hot") outer ring ($I_L = 3 \times 10^{14}$ W/cm^{-2}) surrounding a cooler central axis ($I_L = 1 \times 10^{14}$ W/cm^{-2}). This is indicated schematically in Fig. 2-23, which also shows the actual 2-d mesh during the 100 ps pulse. The intensity falls to $I_L = 1 \times 10^{14}$ W/cm^{-2} again outside the hot ring. There is no hint yet of RCI. However, although we will be seeding and starting the instability during the laser pulse, the really dramatic effects are expected to begin after the laser turns off and the plasma expands and cools.

What we expect to see is a cool jet forming on axis as the pulse ends, accelerating outward as the plasma cools to below 100 eV. During the coast phase, the dense jet will protrude beyond the rest of the corona. When the second laser pulse hits, the hotter parts of the beam again will hit not the jets but the surrounding corona, from which the jets will absorb the emission.

Figure 2-24 is an isodensity contour plot of the HYRAD 2-d Au simulation run at 100 ps, the end of the first laser pulse. The beginnings of jet formation are apparent, because the density contours in the hot part of the beam are bent in (concave), while in the low intensity part of the beam near the axis, a density spike is protruding outward.

We have yet to finish the simulation with another 100 ps pulse followed by a 1 ns main pulse. We expect to see the jet at first doing a lot of absorption, then thermal conduction smoothing it out.

The implications of this result for ICF are clear. For confined secondary acceleration schemes, in which laser radiation is converted to secondary radiation, radiation symmetry will be severely degraded if one uses just a picket fence (discontinuous leading edge) laser pulse and a high-Z ablator because of RCI. KMS Fusion viewfactor calculations with the viewfactor code RAYNA II have been applied to investigate this problem.

We conclude that the RCI plays a role in the observed jetting from high-Z KMSF disk experiments. This instability can produce jets which would disrupt uniform energy deposition and occurs at coronal densities or slightly above critical density. The instability occurs primarily in high-Z materials with growth times as short as 100 ps. A very nonuniform laser beam might be required to seed this instability. The effects of RCI are potentially important for the national ICF program. Specifically, long gaps in picket fence shaped pulses can lead to detrimental asymmetries in wall ablation and radiative uniformity. Other simulations of RCI should be undertaken, especially ones with more detailed atomic physics and full radiation transport effects included.

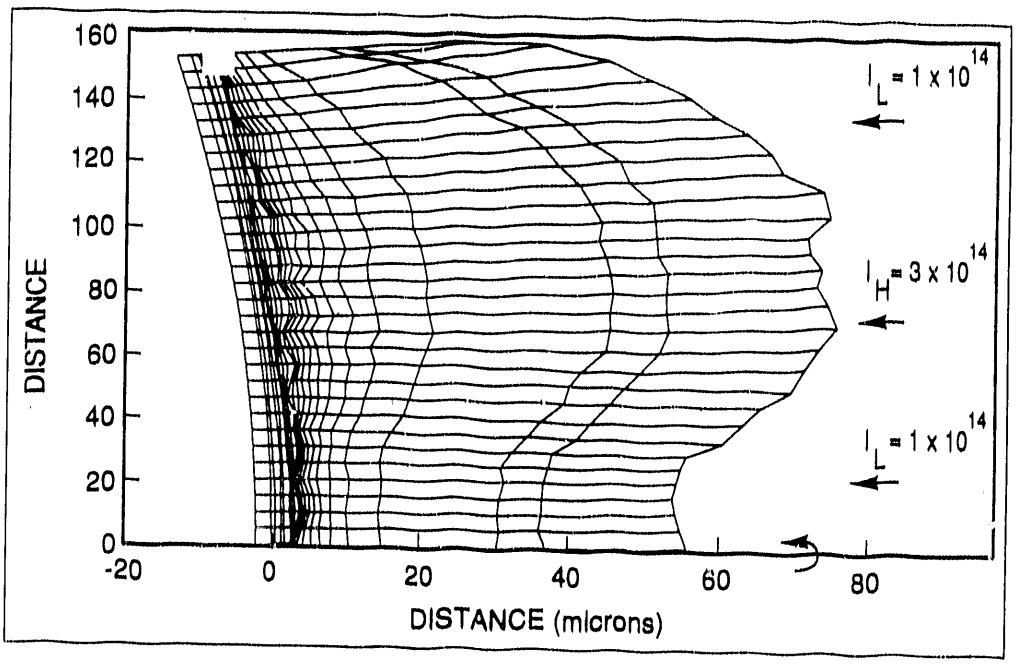

Fig. 2-23. Two-dimensional HYRAD mesh at end of 100 ps laser pulse.

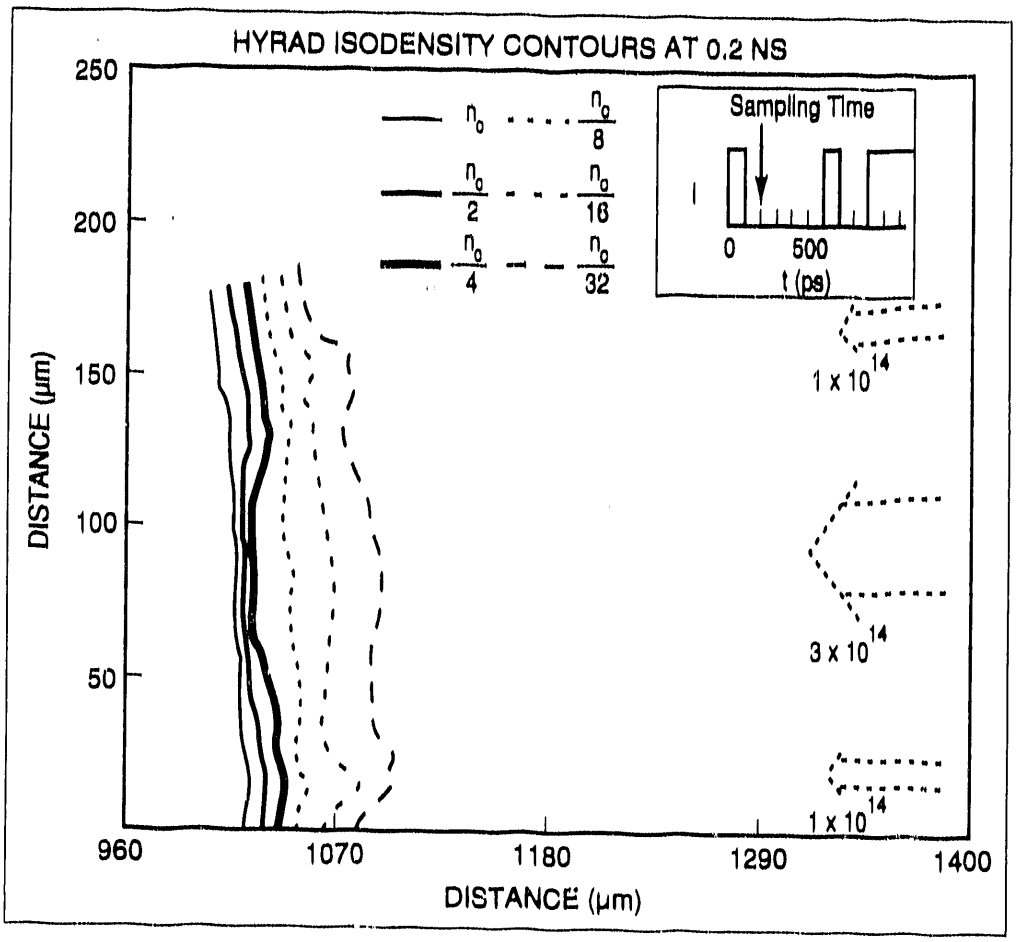

Fig. 2-24. HYRAD isodensity contours at 200 ps produced after 100 ps nonuniform laser illumination. Note beginnings of jet formation on axis.

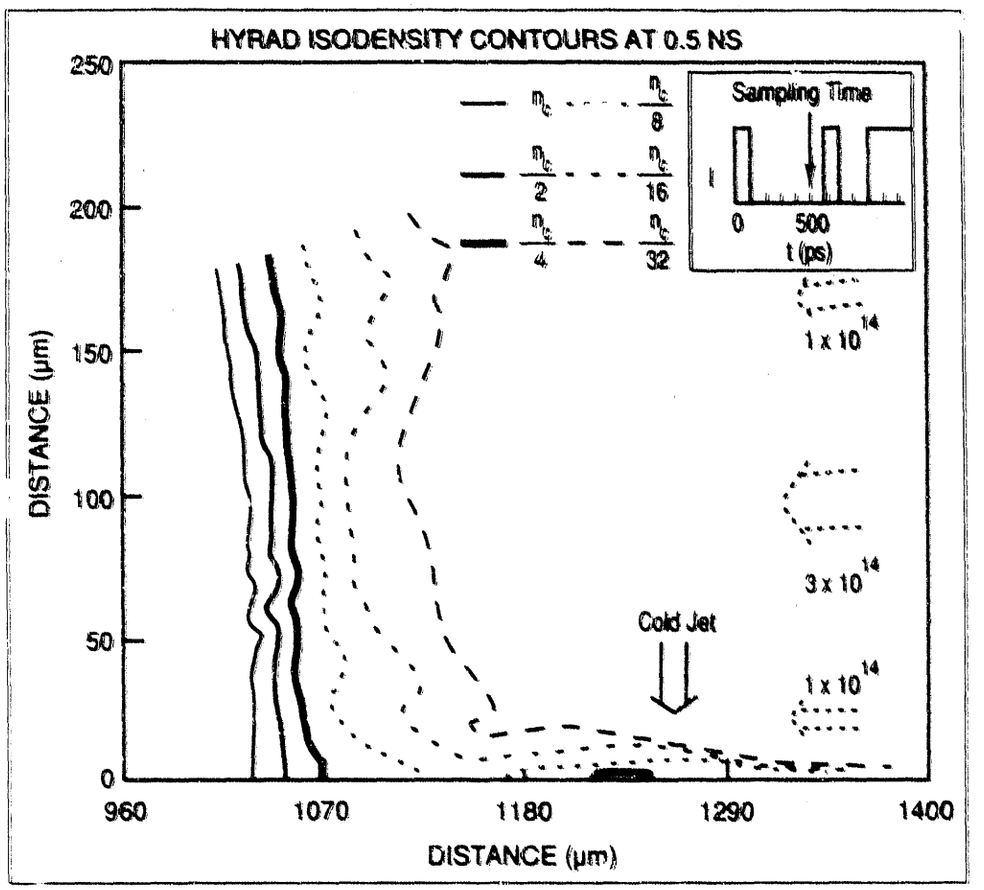

Fig. 2-25. HYRAD isodensity contours at 500 ps show prominent jet features appearing on axis.

For more information, please contact
Norman D. Delamater and Walter B. Fechner

2.6 References

1. R. L. Berger, J. R. Albritton, and C. J. Randall, "Stopping and Thermalization of Interpenetrating Plasma Streams," 1986 Laser Program Annual Report, UCRL-50021-86 (Lawrence Livermore National Laboratory, Livermore, CA, 1987) pp. 2-41.

2. Gar. E. Busch, C. L. Shepard, L. D. Siebert, and J. A. Tarvin, *Rev. Sci. Instrum.* 56 (1985) p. 879.

3. C. DeMichelis and M. Mattioli, *Nucl. Fusion* 21 (1981), p. 677 .

4. G. Charatis, B. K. F. Young, Gar. E. Busch, C. J. Cerjan, W. H. Goldstein, A. H. Osterheld, T. Phillips, M. D. Rosen, R. E. Stewart, and R. S. Walling, *Proc. SPIE* (1988), Vol 913.

5. B. K. F. Young, PhD Thesis, "Space and Time Resolved spectroscopy of Laser-Produced Plasmas: A Study of Density-Sensitive X-ray Transitions in Helium-Like and Neon-Like Ions, LLNL, UCRL 53887 (1988), pp. 291-296.

6. Ibid, pp. 300-309.

7. R. G. Evans, *J. Phys. D.* 14 (1981) L173.

8. R. G. Evans, *Proc. of Second Intl. Conf. on Radiative Properties of Hot Dense Matter*, edited by J. Davis, et al, (1985), p. 173.

9. G. Thiell, and B. Meyer, *Laser and Particle Beams* 3 (1985), p. 51.

10. M. J. Herbst, J. A. Stamper, R. R. Whitlock, R. H. Lehmberg, and B. H. Ripin, *Phys. Rev. Lett.* 46 (1981) p. 328.

11. O. Willi, P. T. Rumsby, C. Hooker, A. Raven, and Z. Q. Lin, *Opt. Comm.* 41 (1982), p. 110.

12. E. F. Gabl, B. H. Failor, C. J. Armentrout, N. D. Delamater, W. B. Fechner, R. A. Bosch, Gar. E. Busch, Z. M. Keonig, D. Ress, L. Suter and R. J. Schroeder, *Phys. Rev. Lett.* 63 (1989), p. 2737.

13. W. B. Fechner, and N. D. Delamater, "Effects of Jetting Instabilities on Ablation of High-Z Disks: The Role of Radiation Cooling Instability," presented to the the *Thirty-first Annual Meeting of The APS Division of Plasma Physics*, Anaheim, CA, Nov. 14, 1989.

14. D. Ress, personal communication.

15. M. G. Haines, *Phys. Rev. Lett.* 47 (1981), p. 917.

16. A. Hirao, and M. Ogasawara, *Phys. Soc. Japan* 50 (1981), p. 668.

17. W. L. Kruer, "Ponderomotive and Thermal Filamentation of Laser Light", *Comments Plasma Phys. Controlled Fusion*, 9 (1985), p. 63.

18. R. Bingham, R. Short, E. Williams, Villeneuve and M. C Richardson, *Plasma Physics and Controlled Fusion* 26 (1984), p. 1077.

19. B. Meerson, *Ap. J.* 347 (1989), p. 1012.

20. R. B. Dahlburg, C. R. DeVore, J. M. Picone, J. T. Mariska, and J. T. Karpen, *Ap. J.* 315 (1987), p. 315.

21. I. S. Shklovskii, "Physics of the Solar Corona" (Oxford: Pergamon Press, 1956).

22. Y. T. Lee, *J. Quant. Spectrosc. Radiat. Transf.* 38 (1987), p. 131.

SECTION THREE. PRESENTATIONS AND PUBLICATIONS

3.1. Presentations

J. S. Ankney, D. L. Musinski, T. R. Pattinson, and W. J. Felmlee, "Evidence of β-decay Driven Uniformity of Thin Solid Deuterium/Tritium Layers Obtained Via Holographic Interferometry," *36th National Symposium of the American Vacuum Society*, Boston, MA, October 23-27, 1989. KMSF-U2216ab.

C. J. Armentrout, "Overview of Plasma Research and Instrumentation at KMS," *31st Annual Meeting of the Division of Plasma Physics of the American Physical Society*, Anaheim, CA, November 13-17, 1989. KMSF-U2260ab.

R. L. Berger, "Suppression of Parametric Instabilities by Induced Spatial Incoherence: A Theoretical Model," *31st Annual Meeting of the Division of Plasma Physics of the American Physical Society*, Anaheim, CA, November 13-17, 1989. KMSF-U2259ab.

R. A. Bosch, E. F. Gabl, and J. D. Simpson, P. M. Bell (LLNL), D. R. Kania (LLNL), and S. H. Langer (LLNL), "Effects of Laser Nonuniformity and Induced Spatial Incoherence on X-ray Conversion," *31st Annual Meeting of the Division of Plasma Physics of the American Physical Society*, Anaheim, CA, November 13-17, 1989. KMSF-U2244ab.

C. C. Bowman, "Tritium Handling Facility at KMS Fusion, Inc.," *36th National Symposium of the American Vacuum Society*, Boston, MA, October 23-27, 1989. KMSF-U2217ab.

A. J. Burek, "High Energy X-ray Spectrometer for Aurora ICF Diagnostics," *31st Annual Meeting of the Division of Plasma Physics of the American Physical Society*, Anaheim, CA, November 13-17, 1989. KMSF-U2243ab.

W. B. Fechner and N. D. Delamater, "Effects of Jetting Instabilities on Ablation of High-Z Disks: The Role of Radiation Cooling Instability," *31st Annual Meeting of the Division of Plasma Physics of the American Physical Society*, Anaheim, CA, November 13-17, 1989. KMSF-U2250ab.

E. F. Gabl, J. P. Sheerin, and J. F. Ostiguy, "Numerical Studies of Nonlinear Ion-Acoustic Waves Using a Full Two-Fluid Description, *31st Annual Meeting of the Division of Plasma Physics of the American Physical Society*, Anaheim, CA, November 13-17, 1989. KMSF-U2242ab.

R. L. Hays, "Using PostScript® in a VAX/VMS Word Processing Environment," *Digital Equipment Computer Users Society Conference*, Anaheim, CA, November 6-10, 1989. KMSF-U2173ab.

R. L. Hays, "Making Newsletters on a VAX," *Digital Equipment Computer Users Society Conference*, Anaheim, CA, November 6-10, 1989. KMSF-U2174ab.

R. L. Hays, "Beginning PostScript® Programming," *Digital Equipment Computer Users Society Conference*, Anaheim, CA, November 6-10, 1989. KMSF-U2209ab.

P. D. Morley, W. B. Fechner, and J. F. McGrath, "Laser Driven Compression of Thermonuclear Fuel in a Dense Conical Container," *31st Annual Meeting of the Division of Plasma Physics of the American Physical Society*, Anaheim, CA, November 13-17, 1989. KMSF-U2253ab.

M. T. Mruzek and W. J. Flemlee, "Study of X-ray Emissions from Cold Deuterium/Tritium Fuel Inside Glass Targets for ICF," *36th National Symposium of the American Vacuum Society*, Boston, MA, October 23-27, 1989. KSMF-U2215ab.

J. F. Ostiguy and J. P. Sheerin, "Ultra-Strong Langmuir Turbulence in Two Dimensions, *31st Annual Meeting of the Division of Plasma Physics of the American Physical Society*, Anaheim, CA, November 13-17, 1989. KMSF-U2255ab.

L. V. Powers, "Stimulated Raman Scattering from Density Extrema," *31st Annual Meeting of the Division of Plasma Physics of the American Physical Society*, Anaheim, CA, November 13-17, 1989. KMSF-U2257ab.

L. A. Scott, D. L. Musinski, T. P. O'Holleran, D. G. Schroen, J. L. Steffy, J. A. Ruppe, and D. A. Steinman, Macroshell™ Target Development: Methods and Materials," *36th National Symposium of the American Vacuum Society*, Boston, MA, October 23-27, 1989. KMSF-U2218ab.

J. P. Sheerin and J. F. Ostiguy, "Studies of Collapse in Two-Fluid Plasmas," *31st Annual Meeting of the Division of Plasma Physics of the American Physical Society*, Anaheim, CA, November 13-17, 1989. KMSF-U2254ab.

3.2. Publications

E. F. Gabl, B. H. Failor, C. J. Armentrout, R. A. Bosch, Gar. E. Busch, Z. M. Koenig, A. Suter (LLNL), D. Ress (LLNL), and R. J. Schroeder (Schlumberger-Doll), "Plasma Jets from Laser-Irradiated Planar Targets," *Phys. Rev. Lett.* **63** (December 1989), pp. 2737-2740. KMSF-U2194.

R. R. Johnson, L. V. Powers, B. H. Failor, E. F. Gabl, Gar. E. Busch, J. T. Larsen, P. D. Rockett, D. Sullivan, R. J. Schroeder (Schlumberger-Doll), C. L. Shepard (Batelle Laboratory), and P. A. Hammerling (La Jolla), "Low-Preheat Cryogenic Implosion Experiments with a Shaped 0.53 μm Laser Pulse," *Phys. Rev. A* **41** (January 1990), pp. 1058-1070 (KMSF-U2207.

END

DATE FILMED

12/03/90